Magnetostriction measurements in magnetically ordered crystals using double crystal x ray diffractometry

Jones, Francis, J.

Jones, Francis, J. (1977) *Magnetostriction measurements in magnetically ordered crystals using double crystal x ray diffractometry*, Durham theses, Durham University. Available at Durham E-Theses Online: http://etheses.dur.ac.uk/9154/

"Magnetostriction measurements in magnetically ordered crystals using double crystal X ray diffractometry"

by

Francis J. Jones B.Sc. (Dunelm)

This thesis, presented in candidature for the degree of Doctor of Philosophy, gives an account of work carried out during the period October 1974 to September 1977 in the Department of Physics, Durham University.

November 1977

ABSTRACT

Magnetostriction measurements have been made on a thin film uniaxial garnet $Tb_2Lu_1Fe_5O_{12}$ with a double crystal diffractometer. A value of the magnetostriction constant λ_{111} was determined from an analysis of the measurements which employed a least squares technique. The value obtained, $\lambda_{111} = (8.12 \pm 1.00) \times 10^{-6}$, was in agreement with an expected value obtained by a linear weighting of the pure Rare Earth Iron garnet measurements of another author. Small ($<10^{-5}$) magnetostriction measurements in materials possessing only 180° magnetic domain walls, where an applied magnetic field is needed, have not previously been reported. The measurement given here made use of the fine resolving power of the double crystal diffractometer, and of a specially constructed electromagnet. A description of these two instruments has also been given. A review of magnetostriction measurements using single crystal X ray diffraction techniques points out the main limitation here of a comparatively low resolving power. Also, without an applied magnetic field, magnetostriction measurements by the X ray diffraction technique can only be made in crystals which have magnetic domain walls other than of the 180° type. Measurements made on different parts of the sample, and even at different parts of the rocking curve, showed considerable variation. This was attributed to local strains in the crystals used. A topographic study of the samples, using the double crystal diffractometer, revealed some of the strains which can be responsible for the local variation in magnetic anisotropy. Such an "in situ" study displays the power of this particular measurement technique over the commonly used electrical resistance strain gauge method. In the latter, various defects in the crystal structure may not be revealed during the course of measurement. Variations in individual magnetostriction measurements may be related almost simultaneously to the defects in the crystal structure when the X ray double diffraction technique is used.

Acknowledgements

It is a pleasure for me to make the following acknowledgements. I would like to thank Professor A.W.Wolfendale for allowing me to use the facilities of the Physics Department to carry out the work which has been reported. My thanks go also to the Science Research Council for my research studentship, and to the Royal Society Paul Instrument Fund which provided the finance for the project.

I am grateful to Dr. W.D.Corner, head of the Solid State Physics group at Durham, who has given me much guidance and encouragement. It is a special pleasure to offer my thanks to Dr. B.K.Tanner, without whose constant guidance, encouragement and enthusiasm I would have found it difficult to complete the work.

I would like to thank Mr.W.Lesley, head of the Physics Department Workshop, Mr. W.Mansey, Mr. A.Lannigan and Mr.K.Moulson for their important technical assistance, Dr K.Bowen of Warwick University who arranged for the magnet pole pieces to be machined at his University's workshop; Dr.Y.Chikaura of Kyushu Institute of Technology, Japan, for the valuable discussions he offered me during his three month visit to Durham University in the summer of 1977; Mr.R.L.Smith who proof-read the final text; Mr.G.Clark and Miss J.Morgan for assistance with the photography, and Mrs R.L.Reed, secretary to Van Mildert College, who typed out the text.

CONTENTS

Page

Chapter 1 Magnetostriction

Chapter 2 Strain gauge measurement of magnetostriction

Chapter 3 Magnetostriction measurements by X ray diffraction techniques

Chapter 4 Proposed method of magnetostriction measurement and review of double crystal diffractometry

Chapter 5 The electromagnet. Design and construction

Chapter 6 The double crystal diffractometer

Page

Chapter 7 Alignment of the Diffractometer

Chapter 8 Magnetostriction measurements

Chapter 1

Magnetostriction

1.1 Introduction

Magnetostriction is the lattice deformation which accompanies the magnetization of a magnetic crystal. Literature on the subject is extensive, going back to the last century when Joule (1842) reported the expansion of an iron bar as it was magnetized in a given direction. The effect is quite small, corresponding typically to a strain of 10^{-5}. Study of the effect may throw light on the nature of the internal forces at play in a magnetic crystal. The phenomenon is also of use in investigating magnetization processes, and analyzing magnetization curves. Calculations of magnetostriction versus magnetization curves have been made by Akulov (1931) for iron single crystals. Such calculations are unambiguous when the magnetization proceeds in a known manner. The theory for the magnetostriction of nickel single crystals in terms of the magnetization has been given by the same author (1956). A schematic representation of magnetization and magnetostriction versus applied field is shown in Figure 1.1. It may thus be seen that there exists some relation between the magnetostriction and the state of magnetization of a crystal. A knowledge of the magnetostriction of a magnetic material is of practical importance, being required for the production of electromechanical transducers and bubble domain devices for example.

A comprehensive discussion of magnetostriction, including a historical review, has been given by Lee (1955), while a more recent account by Birss and Isaac (1975) pays particular attention to the effect in magnetic oxide materials.

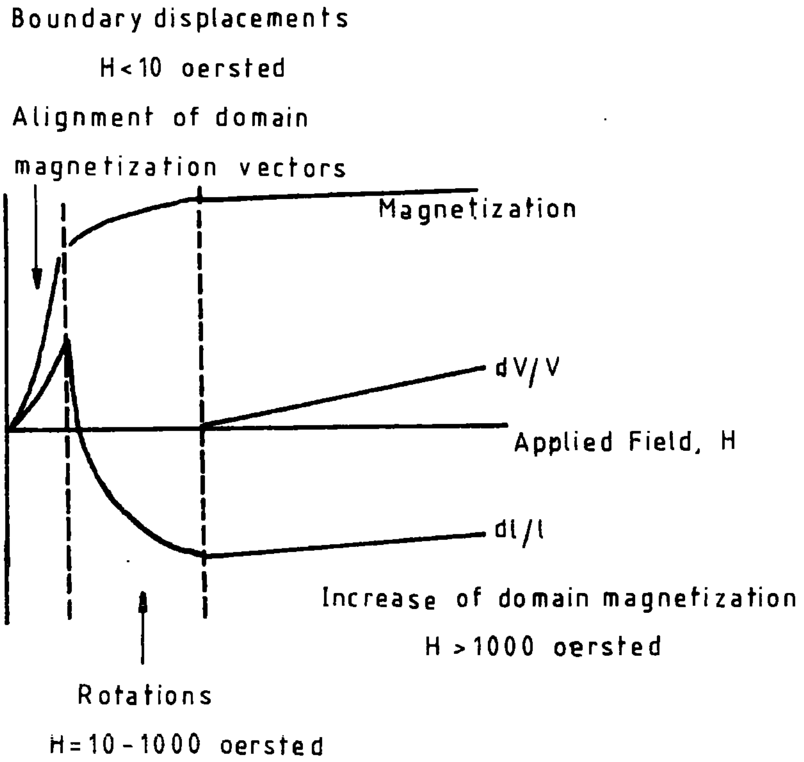

Fig.1.1 Schematic representation of magnetization, linear and volume magnetostriction of iron as a function of magnetic field strength. All ferromagnetics show essentially the same behaviour. Lee (1955).

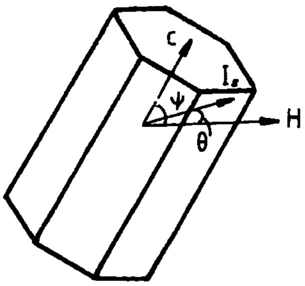

Fig.1.2 Magnetization of a uniaxial crystal.

1.2 Magnetostriction and magnetization

When a crystal is magnetized from the demagnetized state by a field which is applied in a given direction, two types of magnetostriction are associated with the process. As the crystal is taken from an average demagnetized state, a displacement of magnetic domain boundaries occurs followed by rotation of the magnetization vectors towards the direction of the applied field till technical saturation is reached, that is, till the magnetization of the crystal is uniform in one direction. When the crystal is taken beyond technical saturation, an increase of the spontaneous magnetization occurs within the single domain. An anisotropic magnetostriction is associated with the process up to the state of technical saturation; beyond this point an isotropic volume magnetostriction occurs.

For a given domain structure, if the magnetostriction within each domain depended solely on the magnitude of the saturation magnetization within the domain, then no magnetostrictive strain would accompany the magnetization process. The observation that bulk magnetostrictive deformations occur as a crystal is taken from a demagnetized to the saturated state is therefore an illustration of the anisotropic nature of the strains within a domain, and also of the dependence of the strains on the orientation of the saturation magnetization with respect to the crystallographic axes. The anisotropic deformation within each domain is referred to as the spontaneous magnetostriction, that is, the magnetostriction associated with the appearance of spontaneous magnetization. At any stage during the magnetization process, the bulk magnetostriction of the crystal as a whole is therefore correlated with the average magnetization via the spontaneous magnetostriction within each domain. On completion of the process, when the domain magnetization vectors are all aligned, the bulk deformation reaches a value referred to as the saturation magnetostriction. The volume magnetostriction is proportional to the magnitude of the applied field. The two types of striction may be treated separately, and the work of this thesis is concerned with the anisotropic effect.

1.3 Magnetostriction in cubic crystals

Formally, the origin of spontaneous magnetostriction is taken to be a strain dependence of the magnetic energy associated with the crystal. On this basis, a decrease in magnetic energy is produced by the occurrence of appropriate magnetostrictive deformations, the tendency to deform spontaneously being opposed by the increase in elastic energy associated with increasing deformation. Thus the equilibrium strains are those for which the "magnetic" forces and "elastic" forces are equally balanced.

In order to obtain a satisfactory expression describing the magnetostriction for a single crystal, account must be taken of the symmetry of the crystal. Such an account is given in detail by Birss (1964).

The strain is given here for the case of a cubic crystal. The strain in any direction in the crystal, whose direction cosines are β_1, β_2 β_3 (that is, the direction of measurement has these direction cosines) with respect to the Cartesian coordinate system x,y,z, can be shown to be given by the expression

$$\frac{d\ell}{\ell} = e_{ij}\beta_i\beta_j \qquad (1.1)$$

where e_{ij} are the components of the strain tensor. (Repetition of the i and j here denotes summation from 1 to 3.) The axes of the coordinate system coincide with the crystal axes. It is then assumed that the strain depends in some way on the direction of the magnetization with respect to these axes, that is, that $e_{ij} = f(\alpha_1, \alpha_2, \alpha_3)$, where the α's are the direction cosines of the magnetization. The problem then is to find the form of the function $f(\alpha_1, \alpha_2, \alpha_3)$. It turns out that the form which f takes is completely determined by the requirements of lattice symmetry. The energy terms which are relevant are the magnetocrystalline anisotropy energy at zero strain, E_K^o, the magnetostriction energy, E_M and the elastic energy, E_L.

Magnetocrystalline anisotropy means that the magnetization of a magnetic body has preferred directions in which it is relatively easy for the body to be magnetized. This means that the free energy depends on the orientation of the magnetization with respect to the directions characterizing the body. The energy required to rotate the magnetization from a "hard" to an "easy" direction is the anisotropy energy. This subject is given an adequate description by Chikazumi (1964).

E_K^o depends only on the α_i, whilst E_L depends only on the components of the strain tensor e_{ij}. E_M is assumed to be a function of both e_{ij} and α_i. For a cubic crystal then these terms are:

$$E_K^o = K_1 \ (\alpha_1^2\alpha_2^2 + \alpha_2^2\alpha_3^2 + \alpha_3^2\alpha_1^2) \tag{1.2}$$

$$E_M = B_1 \ (\alpha_1^2 e_{11} + \alpha_2^2 e_{22} + \alpha_3^2 e_{33}) \tag{1.3}$$

$$+ 2B_2 \ (\alpha_1\alpha_2 e_{12} + \alpha_2\alpha_3 e_{23} + \alpha_3\alpha_1 e_{31})$$

$$\begin{aligned} E_L = {} & \frac{1}{2}C_{11} \ (e_{11}^2 + e_{22}^2 + e_{33}^2) \\ & + C_{12} \ (e_{11}e_{22} + e_{22}e_{33} + e_{33}e_{11}) \\ & + 2C_{44} \ (e_{12}^2 + e_{23}^2 + e_{31}^2) \end{aligned} \tag{1.4}$$

where K_1 is the first anisotropy constant, $B_{1,2}$ are the magnetoelastic coupling constants introduced by Kittel (1949), and the c's are the elastic constants of the material. In order to see the strain dependence of the anisotropy energy, Kittel expanded the latter in a Taylor series:

$$E_K = E_K^o + \left[\frac{\delta E_K}{\delta e_{ij}}\right]^o e_{ij} + \frac{1}{2}\left[\frac{\delta^2 E_K}{\delta e_{ij}\delta e_{k\ell}}\right]^o e_{ij}e_{k\ell} + \ldots \tag{1.5}$$

The first term refers to the anisotropy energy at zero strain. The second term, describing the interaction between the magnetocrystalline anisotropy and the state of strain, is called the magnetoelastic energy density. The components of $\left[\frac{\delta E_K}{\delta e_{ij}}\right]^o$ involve products of the magnetoelastic coupling constants B_i with the direction cosines α_i. The final term is formally regarded as the magnetostrictive contributions to the elastic stiffness constants, describing the lowering of the intrinsic symmetry of the lattice by the magnetostriction. It can be seen then that the terms E_K^o and E_M are given by the first two terms in the series expansion.

The three terms E_K^o, E_M, E_L are added together and the sum is minimized with respect to the e_{ij}'s. The equations thus obtained are solved to give the equilibrium strain components. An expression for the strain is then found using equation (1.1). For a demagnetized crystal, with a perfectly random distribution of domains, $\frac{d\ell}{\ell} = 0$. In this state, the mean values $\overline{\alpha_i^2}$ and $\overline{\alpha_i\alpha_j}$ are equal to $^1/3$ and 0 respectively both when [100] and [111] are the easy directions. The expression finally obtained is

$$\frac{d\ell}{\ell} = \frac{-B_1}{C_{11}-C_{12}} (\alpha_1^2\beta_1^2 + \alpha_2^2\beta_2^2 + \alpha_3^2\beta_3^2 - {}^1/3) \qquad (1.6)$$

$$\frac{-B_2}{C_{44}} (\alpha_1\alpha_2\beta_1\beta_2 + \alpha_2\alpha_3\beta_2\beta_3 + \alpha_3\alpha_1\beta_3\beta_1)$$

To obtain the strain when the magnetization is along [100], parallel to the measurement direction, then $\alpha_1 = 1$, $\alpha_2 = \alpha_2 = 0$ and $\beta_1 = 1$, $\beta_2 = \beta_3 = 0$, thus

$$\frac{d\ell}{\ell} = \frac{-B_1}{C_{11}-C_{12}} \cdot \frac{2}{3} = \lambda_{100} \qquad (1.7)$$

When the measurement direction and the magnetization are parallel to [111], the strain, with $\alpha_i = \beta_i = 1/\sqrt{3}$, is

$$\frac{d\ell}{\ell} = \frac{-B_2}{C_{33}} \cdot \frac{1}{3} = \lambda_{111} \qquad (1.8)$$

λ_{100} and λ_{111} are the magnetostrictions obtained when the crystal is magnetized along the [100] and [111] directions respectively from the state of demagnetization. A corresponding value for the λ_{110} may be obtained, and this can be shown to be given by

$$\lambda_{110} = \frac{1}{4}\lambda_{100} + \frac{3}{4}\lambda_{111} \qquad (1.9)$$

Equation (1.6) may be rewritten

$$\frac{d\ell}{\ell} = \frac{3}{2}\lambda_{100}\left(\alpha_1^2\beta_1^2 + \alpha_2^2\beta_2^2 + \alpha_3^2\beta_3^2 - {}^1/_3\right) \qquad (1.10)$$

$$+ 3\lambda_{111}\left(\alpha_1\alpha_2\beta_1\beta_2 + \alpha_2\alpha_3\beta_2\beta_3 + \alpha_3\alpha_1\beta_3\beta_1\right)$$

The ideal demagnetized state is not always easily obtained. Thus in any experiment λ_{100} and λ_{111} are usually obtained from measurements of the strain difference which occurs between different directions of magnetization of the crystal.

A two constant expression might not always account adequately for the measurements of magnetostriction for a given crystal. For such cases, a higher order approximation in the expression for E_K may be taken, that is, the third term of equation (1.5) may be included. In this way, a five constant expression is obtained. The magnetostrictions of iron and nickel are usually expressed in terms of a five constant expression. However, the two constant expression accounts for many results quite adequately.

For a uniaxial material, it is shown by Chikazumi (1964) that when the angle between the magnetization and the uniaxial direction is changed from 0 to Ψ, as shown in Figure 1.2, the elongation changes by an amount given by

$$\Delta\frac{(d\ell)}{\ell} = \frac{3\lambda}{2}\left(1 - \cos^2\Psi\right) \qquad (1.11)$$

where λ is the magnetostrictive deformation along the uniaxial direction.

1.4 Quantum mechanical formulation

The classical formalism, in which the magnetization is coupled to the strain by magnetoelastic coupling constants has been extended by Callen and Callen (1963) to a quantum mechanical approach in which the ionic spins are coupled to the various permitted strain modes. The coupling is included in a Hamiltonian which is made up of the following terms:

$$H = H_M + H_e + H_{me} + H_\alpha \qquad (1.12)$$

These four terms are respectively the intrinsic magnetic energy, the elastic energy, the magnetoelastic coupling and the intrinsic anisotropy energy. The Hamiltonian was constructed for a crystal of cubic symmetry. The anisotropy energy is that given by the single ion model. For a discussion of this model, reference may be made to Chikazumi (1964). In this, the orbital electrons are coupled to the electrostatic crystal field which has the symmetry of the lattice. The ionic spin thus sees the crystal lattice via the mechanism of spin orbit coupling. The isotropic exchange interaction, which is strain dependent, is then modulated by the anisotropy. The terms H_{me} and H_α are taken as perturbations on the unperturbed Hamiltonian H_M whilst H_e appears as a classical additive term. The equilibrium strains are then obtained formally by minimizing the free energy again with respect to the strains.

The single ion approach has been extended by Callen and Callen (1965) to include other crystal symmetries, and also to include possible two ion interactions, where significant magnetoelastic coupling arises from the strain modulation of the anisotropic exchange interactions between two ions. Callen (1968) has reviewed magnetostriction measurements in terms of their correlation with the single ion and two ion models.

1.5 Structure and magnetostriction in garnet materials

The measurements to be descriped in Chapter 8 involve the magnetostriction in the rare earth iron garnet material $Tb_2LuFe_5O_{12}$. A description of the relevant aspects of the crystal structure of the rare earth garnets, and of the magnetostriction, will be given here.

1.5.1 Structure

The composition which typifies the garnet structure is $Y_3Fe_5O_{12}$, yttrium iron garnet. The possibility of substitution of Y^{3+} and $A\ell^{3+}$ for Mn^{3+} and Si^{4+} in the natural garnet $Mn_3A\ell_2Si_3O_{12}$ was pointed out by Yoder and Keith (1951). They thus obtained for the first time the garnet $Y_3A\ell_5O_{12}$ free from silicon. Various substitutions may be carried out which yield many materials with interesting and technologically important properties.

The Fe^{3+} ion may be substituted by a trivalent ion such as Cr^{3+}, $A\ell^{3+}$, Ga^{3+}, Sc^{3+}, In^{3+}, Co^{3+}, or by a pair of tetravalent and divalent ions such as Ti^{4+} and Cd^{2+}, Zr^{4+} and Co^{2+}, Si^{4+} or Sn^{4+} and Mn^{2+}, Zr^{4+} or Hf^{4+} and Co^{2+} or Ni^{2+}, Ge^{4+} and Cd^{2+}, or by a pentavalent ion V^{5+}, Nb^{5+}, Ta^{5+}.

The Y^{3+} may be substituted by an ion of rare earth from Pm^{3+} to Lu^{3+}, whose atomic radii are comparable. Substitutions may be carried out completely or partially.

The crystalline structure has three types of cation sites: dodecahedral, octahedral and tetrahedral. The large yttrium ions are in a dodecahedral position. The Fe^{3+} ions with small ionic radii are located in a tetrahedral ($3Fe^{3+}$) position with four nearest oxygen ion neighbours, amd in an octahedral ($2Fe^{3+}$) position surrounded by six oxygen ions. Each yttrium ion is surrounded by eight oxygen ions. The fact that all of the sites are occupied by cations contributes to the high stability of the compound. The various aspects of the structure are shown in Figure 1.3. The crystal lattice is cubic centre with a unit cell parameter (typically) of $a = 12.4\overset{o}{A}$. Each unit cell contains four formula units.

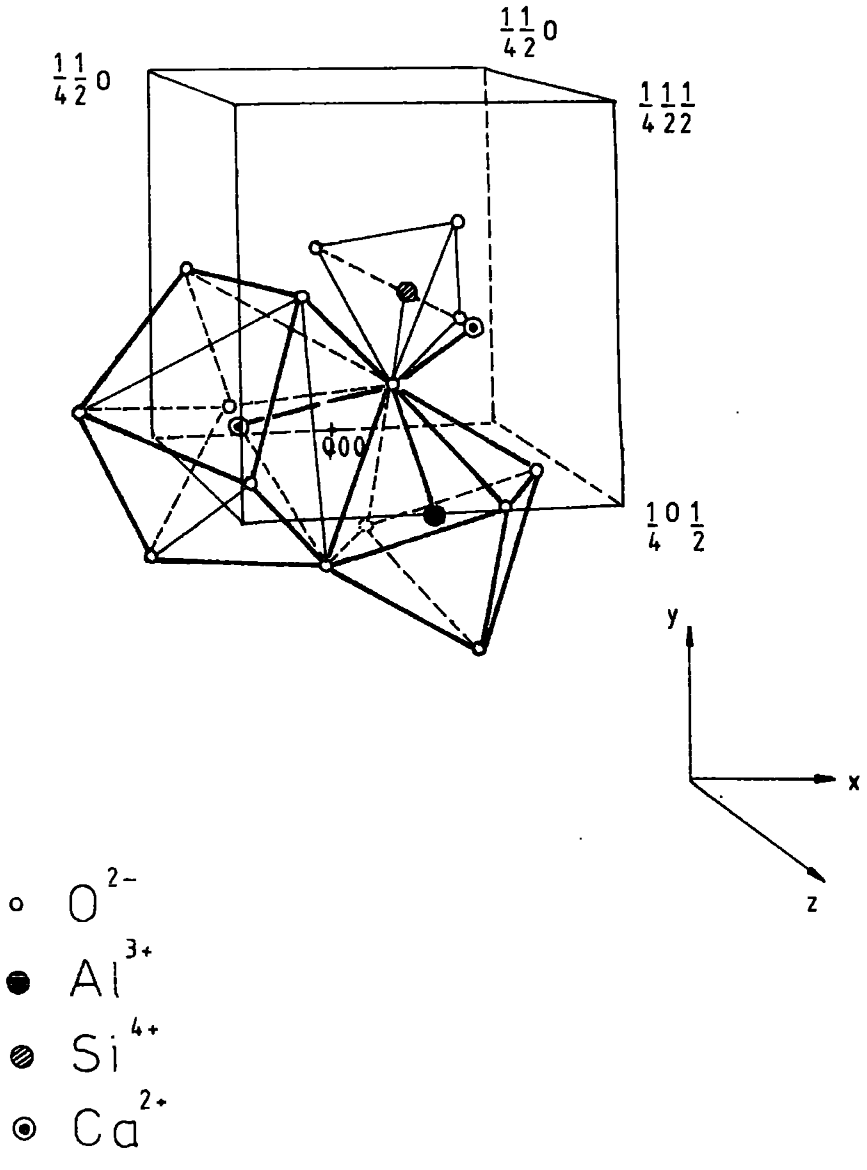

Fig.1.3. Coordination about an oxygen ion in the garnet grossularite. (Makram and Vichr (1975)).

1.5.2 Growth of garnet materials

Growth processes for the production of garnet materials have been described by Makram and Vichr (1975). These include the Czochralski method and the flux method. Gadolinium gallium garnet ($Gd_3Ga_5O_{12}$ or G.G.G.) crystals have been grown by the Czochralski technique. G.G.G. single crystals are widely used as substrate material onto which magnetic garnet thin films are deposited epitaxially.

There are two important processes for the growth of such thin films. Liquid phase epitaxial growth of mixed rare earth garnets onto G.G.G. substrate has been described by Shick et. al. (1971), while chemical vapour deposition has been used, and described, by Robinson et. al. (1971) to grow mixed garnets on SmGa garnet and SmGdGa garnet substrates. In both cases the thin films were used for bubble domain devices. The structural perfection of the substrate plays an important role in determining the quality of the thin film produced.

The strain inducing imperfections which occur during the growth of the substrate are dislocations, growth striations and facet regions. Cockayne and Roslington (1973) have described how almost dislocation free crystals have been obtained by careful alteration of the rotation rate during the Czochralski growth process. With few exceptions, dislocations observed appear to be generated from the seed/crystal interface. During growth, the crystals develop a solid/liquid interface which is convex to the melt. When the growth direction belongs to <111>, facets of the type {211} and {110} form at low rotation rates (10-50 revolutions per minute). The facets produce a macroscopic strain. However, it is observed that the crystals containing facets are dislocation free, that is, the facets serve to block dislocation propagation from the seed over the volume of crystal they occupy. When the rotation rate is increased to typically 80-100 revolutions per minute, the interface becomes planar so that facets no longer form, and the macroscopic strain effect is eliminated. Thus if the rotation rate used throughout growth is low, and then increased at the end, G.G.G. substrate materials free from both localized and macroscopic strain centres may be produced. Dislocations appearing at the seed have also been rendered ineffective by the formation of a narrow neck ahead of the main portion of the boule, as was pointed out by O'Kane et. al. (1973). Dislocations in the form of helices and closed loops, which appear in the substrate, and which do not have their origin at the seed, have been studied by Stacy (1974a) and Miller (1973). They can be prevented by addition of excess Gd_2O_3 to the melt.

1.5.3 Effects of substrate defects on the perfection of the thin films

(i) Dislocations. Stacy (1974b) has studied the extent to which imperfections in the substrate are replicated in the epitaxial layer. The magnetic layers grown on dislocation free substrates remain free of dislocations when no other localized strain centres (e.g. inclusions) are present. Generally dislocations do not readily form in garnets. The large lattice parameter ($a \doteqdot 12.4\text{Å}$) together with a reluctance to form partial dislocations, leads to dislocations with a large Burgers vector, and thus a large energy of formation. Misfit dislocations between the garnet substrate and the epitaxial layer are not likely to be observed. Matthews and Klokholm (1972) have pointed out that when the substrate layer lattice misfit exceeds about 10^{-3}, as is just the case here, the stress is relieved by cracking instead of by nucleation of dislocations.

(ii) Facets. It has been shown by Cockayne et. al. (1973) and Glass (1972) by X ray diffraction measurements that in the faceted regions of a G.G.G. crystal the lattice parameter is slightly larger than that of the unfaceted regions ($\Delta a/a \doteqdot 10^{-4}$). When a garnet platelet containing a facet region is used as a substrate for an epitaxially deposited magnetic layer, the strain associated with the facet is carried on through into the film. Stacy (1974b) has shown this with a comparison of X ray topographs of the substrate and of the film layer immediately above. Hansen et. al. (1973) have pointed out that such strain can cause a local change in the magnetic anistropy in the film. It was suggested by Cockayne et. al. (1973) that the origin of the facet strain lies most likely in the segregation of oxygen in the facet region.

(iii) Growth striations. Growth rate fluctuations during Czochralski growth give rise to compositional variations, which appear as growth striations in a double crystal X ray topograph. Growth rate fluctuations occur for all Czochralski grown crystals. Although growth striations provide one way of studying interface shape history, the strain associated with them, typically $<5 \times 10^{-5}$, does mean that rocking curves obtained on a double crystal X ray diffractometer will, owing to the striations alone, be typically 12 to 15 seconds of arc wide at the intensity half height.

The strain fluctuations owing to striations in the substrate crystal may not always be transferred into the magnetic film. Basterfield et. al. (1968) have pointed out that there is a strain anisotropy associated with the striations. In the substrate crystal the strain associated with a particular striation is normal to the striation surface, and is zero in the plane of the striation. Only those strain components which are parallel to the substrate surface are carried over into the epitaxial layer. If a series of striations with strain amplitude "e" intersects the substrate surface at an angle Θ, the strain amplitude transmitted to the epitaxial layer will be $e.\sin^2\Theta$.

1.5.4 Magnetostriction in garnet materials

Detailed calculation of the magnetostriction for a real material is a more formidable problem than that of the magnetocrystalline anisotropy. For the former, further complication is introduced in that evaluation of strain potentials involving the first derivatives of energy density terms is necessary. Also, in order to calculate the magnetostriction constants from the magnetoelastic constants, a knowledge of the elastic constants is required. For the magnetic oxides, the available experimental data are sparse. Consequently, detailed calculations of magnetostriction constants have been carried out for only a few materials (for example, calculations were made for ferrite materials by Tsuya (1958), and on the magnetostrictive behaviour of Co^{2+} in spinels by Slonczewski (1961)).

Magnetostriction measurements were made by Callen et. al. (1963) on yttrium iron garnet (Y.I.G.), in which the magnetization is due solely to the Fe^{3+} ions. The results were compared with the phenomenological equations of the single ion theory, and the agreement was good. Measurements by Clark et. al. (1968) on partially substituted dysprosium yttrium iron garnet shows that the magnetostriction is linear in rare earth concentration. This observation is evidence for the validity of the single ion model in the garnets. It is possible to relate the rare earth magnetostriction to the rare earth magnetization by subtracting the Y.I.G. contributions from the overall magnetostriction and magnetization. Thus where a significant magnetoelastic coupling arises from the strain modulation of the anisotropic exchange interactions, the rare earth magnetostriction can be considered as the sum of contributions from the different sublattices. Measurements on 10% Yb^{3+} ions in Y.I.G. and Ce^{3+} ions in Y.I.G. by Comstock and Raymond (1967) were accounted for by the anisotropic exchange interaction between rare earth and iron ions, rather than by the single ion crystal field model. A similar report is also made by Smith and Jones (1967) for measurements on Yb substituted Y.I.G. The marked effect of small amounts of terbium impurities in Y.I.G. has been demonstrated by Belov et. al. (1966) in poly-crystalline samples.

Magnetostriction measurements have been made by Iida (1963, 1967) on a whole series of rare earth iron garnets. These measurements are to be referred to again in several of the later chapters. The most detailed study of magnetostriction in rare earth iron garnets has been carried out by Clark et. al. (1964, 1966) on Gd, Dy, Ho and Er iron garnets. Here the single ion theory was applied as it was to Y.I.G., but account had also to be taken of the third magnetic sublattice.

It perhaps should be pointed out that in the case of Néel collinear ferrimagnets, the crystal is considered to be made up of individual sublattices. Each has its own magnetization with different temperature dependences. When the separate sublattice magnetoelastic coupling constants are of opposite sign, and the behaviour with temperature is different, then magnetostriction compensation points may occur, that is, temperatures may occur where the magnetostriction is zero. Correspondingly, magnetization compensation points may occur also. At the latter points, the measurements of Clark et. al. (1964, 1966) on Dy, Ho and Er iron garnets dip sharply to zero, since there the sublattice moments do not remain parallel to the applied field.

1.6 Uniaxial anisotropy in garnet films

Thin films of magnetic garnet materials grown by the method of liquid phase epitaxy or chemical vapour deposition usually have an induced uniaxial magnetic anisotropy. This is superimposed on the normal cubic magnetocrystalline anisotropy. Heinz et al. (1971) have pointed out that the dominant source of the uniaxial anisotropy observed in magnetic oxide films formed by chemical vapour deposition onto non-magnetic substrates is magnetostriction. The magnetic films are normally in a state of mechanical stress owing to a mismatch between lattice constants and thermal expansions of the film and substrate. If the film is magnetostrictive, then this stress produces a uniaxial magnetic anisotropy.

Kurtzig and Hagedorn (1971) have studied the non cubic anisotropies in thin film garnets. It was noted that the thin films $Y_3 Fe_{4.1} Ga_{0.9} O_{12}$ and $Tb_{2.4} Er_{0.6} Fe_5 O_{12}$, grown by chemical vapour deposition, retained their induced anisotropy to within 10% after long anneals at 1350°C. It was also observed that strain relief had a strong effect in all of a large number of cracked films. Near a crack in a film, the domain walls appeared wider, and the domains, which have a vermicular appearance in the garnet films, were darker owing to the rotation of the easiest axis of magnetization away from uniaxial direction, usually the film normal, towards the normal to the plane of the crack. These observations indicate that the non cubic anisotropy in these films is mostly strain induced.

In the films grown by liquid phase epitaxy, however, the effect of similar annealing is to reduce the induced anisotropy. Measurements by Shick et al. (1971) showed that when films of $Eu_2 Er_1 Ga_{0.7} Fe_{4.3} O_{12}$ and $Eu_1 Er_2 Ga_{0.7} Fe_{4.3} O_{12}$ were annealed at 1250°C in oxygen, the respective losses in induced anisotropy were 100% and 96%. The above observations of the effects of strain relief near cracks were extended to films grown by liquid phase epitaxy, and no effect was observed.

The uniaxial anisotropy in these latter films is thought to be induced mostly by ordering resulting from the growth, and not by strain. Such induced anisotropy is similar to that described by Rosencwaig and Tabor (1971) and by Callen (1971). Their descriptions were for the case of induced anisotropy under certain growth faces of bulk grown mixed garnet crystals.

Callen (1971) showed that pair ordering of a rare earth ion with its first and second nearest tetrahedral-iron ions is achieved by preferential occupation of particular rare earth sites. The mechanism is seen most clearly if just nearest neighbours are considered. For some rare earth sites, the nearest neighbours are to the left and the right (X sites), for others they are in front and behind (Y sites), and for others they are above and below (Z sites). If, for example, the growth plane is (001), then the crystal spacing at the growth surface is severely strained in the z direction but not in the x or y directions. This strain is, of course, later alleviated as new planes are added and the old surface becomes the new "bulk". As a rare earth ion leaves the melt and settles into a site on the surface, it finds that the nearest ligand of a Z site is displaced, whereas those of the X or Y sites are not. Depending on size and compressibility, this will almost certainly lead to a preferential occupation of the new ions among the different rare earth sites. The model was then extended to second nearest tetrahedral neighbours, which are the source of the observed anisotropy.

Chapter 2

Strain gauge measurement of magnetostriction

2.1 Techniques for magnetostriction measurement

Since early observations of magnetostriction by Joule (1842), the phenomenon has challenged experimentalists to devise a number of measurement techniques, and thus to determine the parameters which describe it in the many different materials. Optical interferometry was used as early as 1893 by Lochner to study the effect in a bar of iron, while Lloyd (1929) used a combination of optical, mechanical and electrical methods for his study. The value of Young's modulus for a ferromagnetic material changes when its state of magnetization is varied. This phenomenon is known as the ΔE effect, and has its origin in the magnetostrictive deformation. It has been studied, for example, by Street (1948).

2.2 Electrical measurement of magnetostriction

The most widely employed technique of magnetostriction measurement is that involving the resistance strain gauge. In this method, introduced by Goldman (1947), a typical experimental arrangement may be given as follows. A sample with cubic crystal structure is cut in the shape of a disk, whose flat surface is parallel to the (110) plane. On one flat side of the disk, a resistance strain gauge, of composition for example of platinum (92%) tungsten (8%), is cemented to the crystal in the direction $[001]$, and on the other side a second strain gauge is cemented to the crystal in the direction $[1\bar{1}0]$, at right angles to the first gauge. The gauges are incorporated in a D.C. Wheatstone bridge network. The magnetization is rotated in the plane of the disk. From the variation in the resistance of the gauges, as they strain along with the magnetostrictive strain of the sample, expressions for the sample strains may be deduced, which are then expressed in terms of the magnetostriction constants of the material. Bozorth and Hamming (1953) measured the strain along two crystallographic directions as the field was rotated through 90° by 10° intervals. They then employed a least squares method to solve a set of linear equations and thus obtained "a most probable value" for each of the five magnetostriction constants of the material being studied.

Similar measurements of magnetostriction may be made using a capacitance bridge technique. The sample is coupled to one of the plates of a capacitor, as described by Corner and Hunt (1955) for example. The variation in capacitance as the crystal strains in the magnetic field is then used to obtain values for the magnetostriction constants.

2.3 Errors arising in strain gauge measurements

Greenough et al. (1976) have studied the application of the resistance strain gauge technique to the measurement of magnetostriction in iron single crystals. Particular attention was paid to the various sources of error involved, and thus a set of values for the five magnetostriction constants was obtained.

The errors may have a variety of origins and are described as follows.

(i) Field misalignment. The initial alignment of the applied magnetic field is not always easily accomplished, especially when the sample is concealed in a cryostat or furnace. The typical error in the magnetic field setting is $\pm 1^{\circ}$.

(ii) Strain zero error. This is closely allied to the problem of magnetic field alignment and arises from the uncertainty in the position of zero strain levels. The previous error, along with this, may be taken account of to some extent in the curve fitting procedures used in the analysis of the results.

(iii) Gauge misalignment. This source of error, which arises from a misalignment of the strain gauge with a given crystallographic direction, is one of the more difficult to treat. Experimental data will almost certainly contain errors due to gauge misalignment of up to $\pm 1^{\circ}$. Corrections which take account of the major contributions to these errors need to be applied to the analysis of the results.

(iv) Magnetic anisotropy. Owing to magnetocrystalline anisotropy, the angle between the direction of the external applied field and the magnetization vector in the sample may be different from zero unless a saturation field is applied. Suitable corrections may be made for this during the analysis of the results by considering the sum of the anisotropy energy, the energy of magnetization of the sample in the applied field, and the demagnetization energy which arises owing to the sample shape. The total energy is minimized with respect to a given crystallographic direction and the magnetization direction, and the equilibrium angle values are found. This is compared with the angle between the external field and the reference direction, and thus with a knowledge of the differences between these two angles, the appropriate corrections may be made for the effects of anisotropy.

(v) Form effect. A ferromagnetic material will tend to decrease in volume and increase in length along the direction of magnetization, since the demagnetizing energy is lowered by the reduction in volume and the change in the demagnetizing factor. The latter is a constant of a particular sample, dependent on its shape. When a sample is magnetized, the uncompensated magnetic poles at the surface give rise to a reverse field, the demagnetizing field. The shape dependent demagnetizing factor relates the energy associated with the demagnetizing field, the demagnetizing energy, to the saturation magnetization of the sample. The dependence of the demagnetizing energy on the lattice deformation gives rise to a further type of magnetostriction referred to as the form effect.

When the ratio of the thickness to diameter of a disk shaped sample is small, it may be seen that the contribution of the form effect to the measured magnetostriction is also small, and is usually neglected for such samples.

(vi) Calibration and latent errors. Calibrations both of the strain gauges and of the bridge networks are required, and these may lead to errors which need to be corrected.

Some latent inaccuracies are produced, for example, by deviations from the recommended strain gauge installation procedures. These lead to variations in glue line thickness, or elasticity of the bond, which affect the apparent gauge factor. The latter, which is the factor relating the relative change in resistance to the relative change in lattice spacing, may vary, and normally does, from one strain gauge to another.

Also, slight variations in composition from one crystal to another, or any departures from a perfect single crystal structure may affect the results. An example is the case of subgrain boundaries occurring in the crystal. If the strain gauge is placed across a number of such boundaries, then a given lattice direction will not always be in line with the gauge. The contribution to the magnetostrictive deformation owing to the resultant change in direction cosines of the measurement direction is proportional to the angle of misorientation across the boundary to first order. The total error may then amount to several percent. If just the strain gauge technique is used, then the influence of impurities and defects on the magnetostriction constants is impossible to assess.

Callen et al. (1963) used the strain gauge technique to measure the magnetostriction in garnet materials. They have pointed out that a large magnetoresistive effect, which occurs as the magnetic field is applied to the sample, especially at low temperatures, needs to be corrected for in the experimental procedure.

2.4 Examples of magnetostriction measurements

In order to illustrate the considerable spread of various authors' measurements of the magnetostriction constants of iron, Greenough et al. (1976) have collected together a series of values, which is shown in Table 2.1. A survey of the literature has yielded a similar set of data for nickel single crystals, and these magnetostriction constants are shown in Table 2.2. All the measurements in the tables were made by means of the resistance strain gauge technique, and are given for room temperature. The averages of the different values are given for each constant, together with the signs which occur in individual series. Also, the maximum variation about the mean is given for each constant.

It can be seen that the maximum variations about the means are considerably greater for nickel, although the variations are quite serious for both cases. It is noted however that the last two sets of measurements for nickel are in considerable agreement with one another.

2.5 Disadvantages of the strain gauge method

There are several fundamental sources of error which must be met in all measurement techniques which involve the use of an applied magnetic field. Examples are the effect of magnetocrystalline anisotropy, and the contribution to the magnetostriction from the form effect. However, gauge misalignment, along with variation of gauge factor from one gauge to another and the effect of magnetoresistance are disadvantages which are characteristic of the strain gauge technique. In the report by Iida (1967) on the measurements on rare earth iron garnets, the author points out that at 78^{o}K the uncertainty in gauge factors leads to a systematic error possibly as large as 20%. The fact that the method is "indirect", involving further calibration corrections, is a further disadvantage.

Table 2.1

Previous measurements of the magnetostriction constants of iron $h_1 \ldots h_5 \times 10^6$

	h_1	h_2	h_3	h_4	h_5
Webster (1925)		-31.0			
Kaya and Takaki (1936)	38.0				
Carr and Smoluchowski (1951)	31.0	-31.0			
Gersdorf (1961)	36.2	-34.0			
Radeloff (1964)	36.1	-33.0	3.4±0.9	0±4.0	7.0±2.2
Lourens and Viljoen (1966)			1.4±0.4	-3.2±0.8	4.7±1.0
Williams and Pavlovic (1963)	30.0	-28.0	12.7	12.7	-7.6
Mean values	34.3	-31.4	5.8	3.2	1.4
Sign	+	-	+	+ or -?	+ or -?
Maximum Variation about mean	12.5%	10.8%	119%	297%	643%

Table 2.2

Previous measurements of magnetostriction constants of nickel $h_1 \ldots h_5 \times 10^6$

	h_1	h_2	h_3	h_4	h_5
Bozorth and Hamming (1953)	-68.8 (± 3.8)	-36,5 (± 1.9)	-2.8 (± 3.1)	-7.5 (± 5.2)	+7.7 (± 3.1)
Tatsumoto and Okamoto (1965)	-45.0	-47.0	-4.0 (± 2%)	-51.0	-62.0
Benninger and Pavlovic (1967)	-85.0	-80.0	-10.0	-6.0	+12.0
Bower (1971)	-98.5 (± 1.4)	-43.1 (± 0.5)	+0.1 (± 0.9)	+3.4 (± 0.6)	+0.2 (± 0.9)
Lee and Asgar (1971)	-94.3	-42.5	-0.7	+0.2	+1.5
Mean values	-78.3	-49.8	-3.5	-12.2	-8
Sign	-	-	+ or -?	+ or -?	+ or -?
Maximum Variation about mean	42.5%	60.6%	185.7%	318%	665%

It is perhaps a reasonable observation that not a great deal of attention has been paid to the structural perfection of many of the samples studied, especially in the light of the considerable variety of results which have been obtained. The X ray technique used in the work of this thesis, and which will be described later, allows not only "direct" measurement of the magnetostrictive deformation in the sample, but almost simultaneously allows an assessment of its structural quality also. Thus the results obtained may be considered to a greater extent in the light of the perfection of the specimen.

Chapter 3

Magnetostriction measurements by X ray diffraction techniques

3.1 Magnetic domains

Below the magnetic ordering temperature, a spontaneous magnetization exists inside a volume of ferromagnetic material, owing to the quantum mechanical exchange interaction between the spin magnetic moments. Because of the magnetocrystalline anisotropy, the magnetization lies favourably along some crystal directions. The general features of the magnetic configurations existing inside a given material have been discussed by Chikazumi (1964). A spherical single crystal specimen is considered. If the specimen is composed of a single domain, as shown in Figure 3.1(a), then because of the uncompensated magnetic poles appearing on the surface, there is an associated magnetostatic energy. One way to avoid this is to make the inner magnetization rotate inside the sphere, as shown in Figure 3.1(b). There are then no magnetic poles, but instead the neighbouring spins make some angle with one another, so that some amount of exchange energy is stored. The choice between the two possibilities is essentially determined by a comparison of the two kinds of energy, which are dependent on the shape and volume of the specimen and on the exchange interaction. A minimization of total energy leads to the specimen having some stable magnetic structure. If the crystal has large magneto crystalline anisotropy, the inner magnetization is forced to point parallel to an "easy" direction. For crystals with easy directions along a <100> direction, the domain structure may look like that shown in Figure 3.1(c), whilst for crystals with uniaxial anisotropy, the inner magnetization must point either parallel or anti-parallel to the easy direction. In either case, the magnetostatic energy is much less than that associated with the single domain of Figure 3.1(a). The domains, regions of uniform magnetization, are separated by

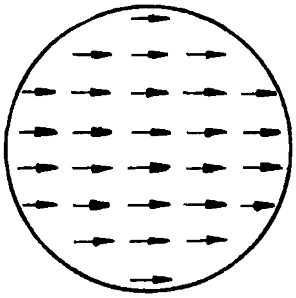

Fig.3.1(a). Single domain structure

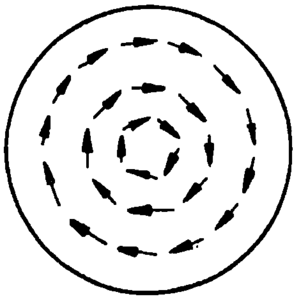

Fig.3.1(b). Domain structure of a material with small crystal anisotropy.

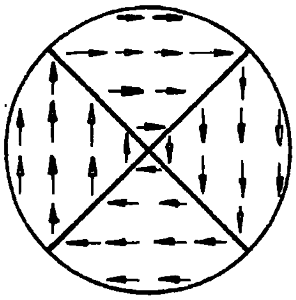

Fig.3.1(c). Domain structure of a material with large crystal anisotropy.

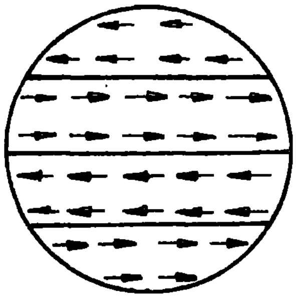

Fig.3.1(d). Domain structure of a material with uniaxial anisotropy.

domain walls, relatively very thin layers in which the magnetization gradually rotates from its direction on one side to its direction on the other. Because the direction of magnetization is different on either side of the domain wall, the magnetostrictive deformation in a given direction may also be different on either side, as pointed out by Tanner (1976). This latter difference provides the mechanism for contrast in the observation of magnetic domains by X ray diffraction topography.

3.2 Observation of domains by X ray topography

Observation of magnetic domains using X ray topography was first reported by Merz (1960), whose work is discussed in Chapter 4. The ferromagnetic domains studied were in cobalt zinc ferrite.

Magnetic domains in Fe-Si single crystals were observed by Polcarova and Lang (1962) using Lang's (1959) method of projection topography. Some of the important points they outlined regarding the use of X ray topography in the observation of domains are given as follows.

1. As well as surface configurations, the method shows up interior structures which are not observed by the colloid technique (described by Williams, Bozorth, Shockley (1949)).
2. Domains, dislocations and low angle boundaries can be seen simultaneously on the same topograph.

In a series of works since these first X ray observations, Polcarova, along with Lang (1971), Kaczer (1967), Gemperlova (1969) and Bradler (1972), have studied the X ray diffraction contrast of domains in Fe-Si single crystals. The studies with Lang (1971) have led to a proposed fire structure for some of the domain walls, whilst those with Bradler (1972) produced a measurement of one of the magnetostriction constants for this material. The latter work will be discussed later in this chapter.

In Fe-Si, the easy directions are along the cube axes <100>. Using transmission and reflection topography on a thin platelet cut parallel to the (001) plane, Polcarova and Kaczer (1967) were able to observe 90° walls and fir tree closure domains. A schematic representation is shown in Figure 3.2. The 180° domain walls were not visible, but their position could be determined from the position of the 90° walls and fir trees. Other topographs were taken using different diffractions from the one used above. It was noted that the 90° walls lie in (110) and ($1\bar{1}0$) planes, and it was noted that the walls became invisible if diffraction planes on the [$\bar{1}10$] zone or [110] zone were used. That is, no 90° walls or fir tree branches appeared in these diffractions. The direction of the zone axes is determined by the vector:

$$\underset{\sim}{o} = \hat{m}_2 - \hat{m}_1 \qquad (3.1)$$

where $\hat{m}_2$ and $\hat{m}_1$ are unit vectors in the direction of magnetization on both sides of the wall. The rule for the disappearance of the domain walls on X ray topographs is that

$$\underset{\sim}{o} \cdot \underset{\sim}{g} = 0, \qquad (3.2)$$

where g is the diffraction vector.

Referring to Figure 3.3, it can be seen that planes with $\underset{\sim}{g}$ not perpendicular to $\underset{\sim}{o}$ deviate on crossing the 90° wall. For Fe-Si then, the crystal has cubic structure when no magnetization exists, and a slightly tetragonal structure when the magnetization is present.

The lattice outside a plane (110) 90° wall undergoes only magnetostrictive deformation. For the planes which deviate across the wall, the latter may be conceived as a coherent twinning boundary. No 180° walls are observed at all, as the magnetostrictive deformation is the same on opposite sides of the wall. 180° domain walls may be made visible at the

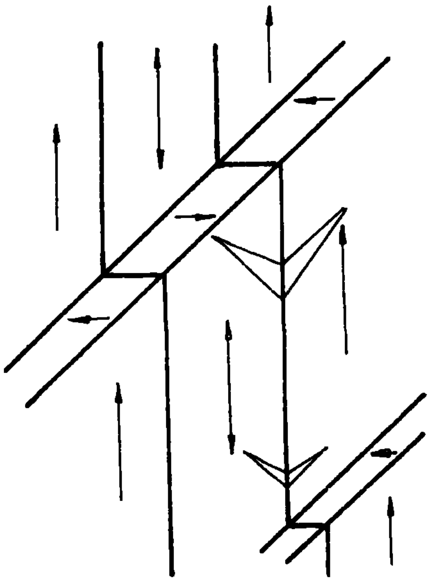

Fig.3.2 Schematic diagram of the domain structure of Fe:Si. In X-ray topographs only 90° walls are visible. 180° wall positions are determined from the position of fir tree domains.

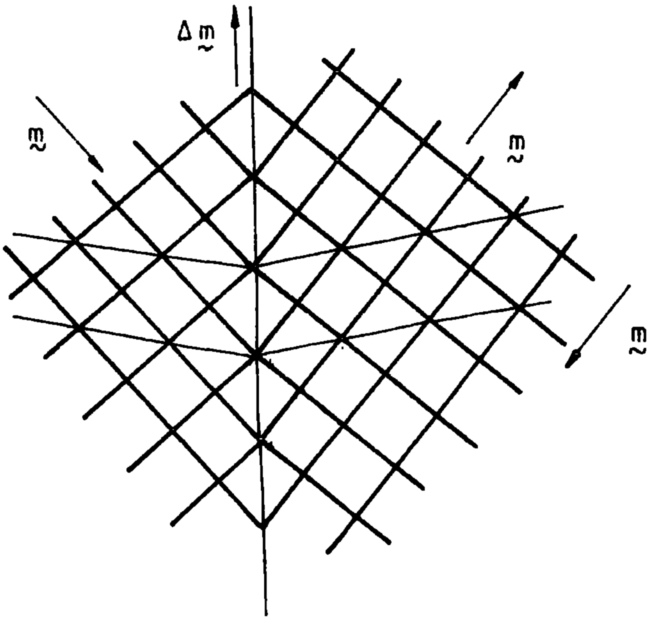

Fig.3.3 Lattice misorientation across 180° walls in iron. Planes with $\underset{\sim}{g}$ not perpendicular to $\Delta\underset{\sim}{m}$ are seen to deviate on crossing the 90° wall. All planes are continuous across the 180° wall.

surface of a sample in some cases when there is a strain relaxation effect as the wall meets the surface (see Sery et al. (1977)). The magnetostrictive deformation inside the wall is compensated by the elastic deformation, so that the total deformation is the same as that outside the wall.

3.3 Magnetostriction measurements with Lang topography

Because the magnetostriction constant is typically small (2×10^{-5} for iron) the difference in interatomic spacing and plane misorientation is very small in neighbouring domains. Therefore, the difference in Bragg angle in going from one domain to the next is much smaller than the typical divergence (>2' arc) of the primary X ray beam used in Lang topography. The Bragg condition is fulfilled for both domains simultaneously, different domains are visible sumultaneously, and there is just a change in contrast at the walls. Thus with the Lang method in this instance, the difference in Bragg angle, owing to misorientation of the diffraction planes across the domain wall, can not be measured and the magnetostriction thus can not be found.

However, if a material with a larger magnetostriction constant is to be studied, it is possible to measure the misorientation in going across a wall from one domain to the next. Such an experiment has been performed by Petroff and Mathiot (1974). They have determined the spontaneous magnetostriction coefficient of terbium iron garnet, $Tb_3Fe_5O_{12}$, by X ray diffraction at 77°K and 4.2°K. The garnet is ferromagnetic below 568°K, its easy axes being along <111>. The magnetostrictive distortion then is along <111>, and a rhombohedral structure of the lattice results. Magnetic domains can appear and are limited by 71°, 109° and 180° walls. In an X ray topographic study of (110) plates by the same authors, a Ni type structure was observed, in which the walls at 71° are in $\{1\bar{1}0\}$ planes, and the 109° walls are in {001} planes. 180° walls were not visible, in agreement with previous remarks. It was noted that at low temperatures, the 71° walls are practically the only ones present. In the experiment then, the (110) plate is mounted in a cryostat and positioned on a Lang camera. The geometry of the domains in the plate is shown in Figure 3.4.

In the domain denoted by I, the magnetization direction is $[\bar{1}11]$. In domain II, the magnetization is in the $[1\bar{1}\bar{1}]$ direction.

For certain reflections there appears an angular misorientation between the type I and II domains. Because the resultant magnetostrictive distortion here is rhombohedral and not tetragonal as for Si-Fe, equations for magnetoelastic equilibrium may be quite different. It is pointed out by Mathiot et al. (1973) that domain rules regarding domain contrast are not verified. Although Polcarova's rule has been supported by observations on Y.I.G., Patel et al. (1973) have observed domain contrast in Co substituted orthoferrites contrary to the predictions of Polcarova's model. Thus the whole subject can become quite complex.

The change in angle across the wall, $\delta(\Delta\Theta)_{1-11}$, is proportional to the component of strain, the equilibrium value of which is found by minimizing the energy density, and in Mathiot's experiment is given by: $e_{ij} = \frac{3}{2}\lambda_{111} \times \mu_i \mu_j$, where $\mu_{i,j}$ are direction cosines of the magnetization. For the final expression for $\delta(\Delta\Theta)_{1-11}$, two angles characteristic of the problem are used. These are, Ψ, the angle of asymmetry between the entrance surface and the normal to the reflecting plane, and ϕ, the angle between the trace of the wall on the entrance surface and that of the reflection plane. Then:

$$\delta(\Delta\Theta)_{1-11} = \sqrt{2}\,\lambda_{111} \sin 2\phi \cos^2\Psi \left[\tan\Theta - \tan\Psi\right] \qquad (3.3)$$

It is noted that the change is proportional to tan Θ and so rises with increasing order of reflection. Also $\delta(\Delta\Theta)$ is a maximum for $\phi = \pi/4$, that is for the reflecting plane whose trace on the entrance surface is at 45° to that of the wall. $\delta(\Delta\Theta) = 0$ for $\phi = \pi/2$ and 0.

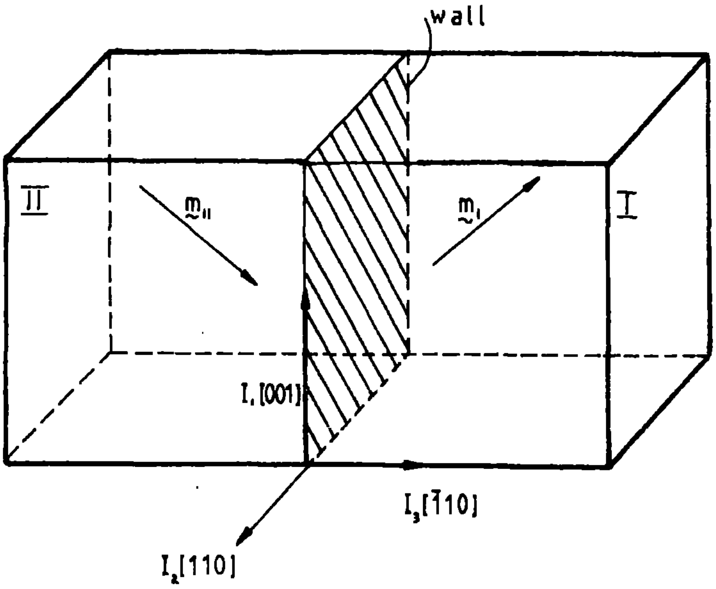

Fig.3.4 Domain geometry of crystal plate studied by Mathiot and Petroff. (1974).

Table 3.1(a). Results at 4.2°K.

Reflection	$\delta(\Delta\theta)$sec.	λ_{111}x10^6
$\bar{8}, 8, 8$	260	2198
$\overline{12}, 12, 12$	435	2151
$\bar{8}, 8, \bar{8}$	250	2113
$\overline{12}, 12, \overline{12}$	455	2250
$\bar{8}, 8, \overline{16}$	410	2267
$3, \bar{1}, \bar{2}$	265	2183
$\bar{3}, 1, 2$	160	2253
$6, \bar{2}, \bar{4}$	315	2132
$\bar{2}, 6, 4$	325	2200
$\bar{4}, 12, \bar{8}$	440	2121
$\bar{4}, 0, 2$	250	2202
$\bar{4}, 0, \bar{2}$	237	2088
$\bar{4}, 0, \bar{4}$	187	2189
$4, 0, 4$	322	2107

Table 3.1(b). Results at 77°K.

Reflection	$\delta(\Delta\theta)$sec.	λ_{111}x10^6
$\overline{12}, 12, \overline{12}$	105	519
$\overline{12}, 12, 12$	106	524
$\bar{2}, 6, \bar{4}$	80	542
$\bar{4}, 12, \bar{8}$	120	578
$\bar{4}, 8, \overline{12}$	100	482
$0, \bar{4}, \bar{2}$	102	513
$0, 4, \bar{4}$	80	523
$0, 8, \bar{8}$	95	501
$\bar{8}, 8, \overline{16}$	90	486

The measurements made at 77^{o}k and 4.2^{o}k are then shown in Table 3.1(a) and Table 3.1(b). The results are seen to agree with those of other authors, and thus display a technique for the measurement of the magnetostriction constant without the use of an applied magnetic field. Similar work extended to Dy.I.G.and Y.I.G.has been reported by the same authors (1975).

3.4 Measurements with large magnetostriction materials

In the first half of the sixties, Rhyne et al. (1963) reported "giant" magnetostriction in the heavy Rare Earth elements.

The constants describing the magnetostriction were evaluated by Darnell (1963) from X ray measurements of the crystal cell dimensions of Dy in its ferromagnetic state below 86^{o}K, and for Tb in its ferromagnetic state below 220^{o}K. The maximum observable single crystal magnetostrictions are estimated to be about 5×10^{-3} for both materials, this being at 22^{o}K.

It was pointed out that when such large values of magnetostriction are apparent, it becomes a matter of choice whether one wishes to consider the magnetized crystal in terms of magnetostrictive distortions superimposed on the original symmetry, or in terms of a new structure of lower symmetry.

Magnetostriction tetragonality of about 5×10^{-3} in Fe_2TiO_4 has been observed by Ishikawa et al. (1971). Here the structure determination below the magnetic ordering temperature, 142^{o}k, was made by X ray powder analysis. The diffraction lines showed a splitting completely explained by the tetragonal distortion.

Clark et al. (1976) has made measurements of the large magnetostriction constants of some rare-earth iron compounds, notably $TbFe_2$ and $DyFe_2$, along with the ternary and quaternary alloys of the form $R_xR_yR_zFe_2$ (R = Ce, Pr, Sm, Tb, Dy, Ho, Yb). These cubic rare earth iron materials are the only known compounds possessing such huge room temperature magnetostrictions. It is found that $\lambda_{100} << \lambda_{111}$, $\lambda_{111}/\lambda_{100}$ being more than 600 for $DyFe_2$. The values of λ_{111} are deduced from the splitting of selected X ray diffraction lines and values are shown in Table 3.2.

3.5 Studies of NiO

The distortions of the NiO lattice owing to its magnetic ordering have been studied by several authors, using X ray methods. The magnetic structure of NiO, which is antiferromagnetic, has been studied by Roth (1960) using neutron diffraction and optical methods, and by Slack (1960) who, besides X ray diffraction, also used optical methods.

The ordering below the ordering temperature T_N is shown schematically in Figure 3.5(a). The spins lie in ferromagnetic {111} planes. The antiferromagnetic ordering results in a slight rhombohedral distortion, which is seen as a contraction of the original cubic unit cell along one of the <111> axes. It is pointed out by Darnell (1963) that such structure change (as with FeO, CoO and MnO also) is not usually considered as magnetostriction, since application of normal fields causes no change in magnetization and thus no dimensional change. The distortion is referred to then as exchange striction.

Because this contraction may occur along any of four equivalent directions in the parent cubic crystal, crystallographic twinning which is related to the antiferromagnetic ordering may take place. These twin structures then describe a type of antiferromagnetic domains, referred to as T (twin) domains. Regions of different contraction axes are separated by T walls, which can belong to {001} or {110}, as shown in Figure 3.5(b).

Another type of domain wall exists in NiO, called an S (spin rotation) wall. This type of wall separates regions of the crystal in which there is no change in contraction axis, but merely a rotation of the spin within the ferromagnetic sheets. The magnetostrictive distortions associated with such variations of spin are considerably smaller than the "exchange" striction associated with the T domains.

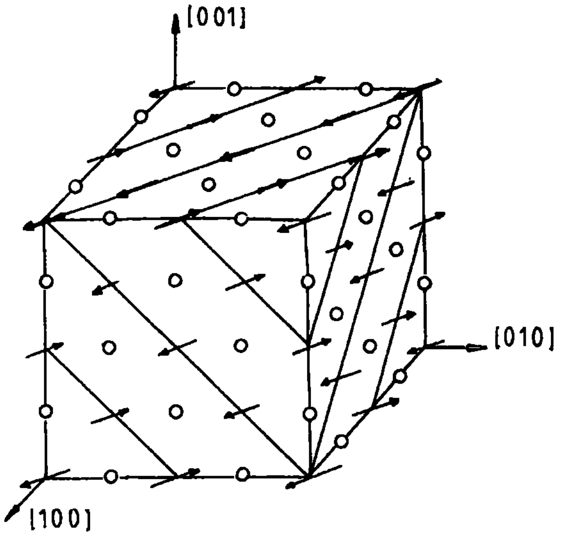

Fig.3.5(a). Antiferromagnetic structure of NiO. The open circles are oxygen atoms. The spins lie in (111) but the the direction within the ferromagnetic (111) plane is not specified. The contraction axis is [111] and the rhombohedral cell shown has $\alpha = 90^{\circ}4'$.

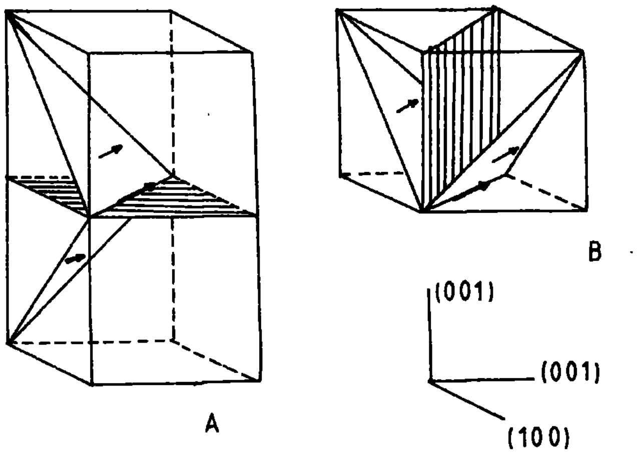

Fig.3.5(b). T walls in NiO. The T walls are shaded. A single ferromagnetic sheet in adjoining T regions is shown and the magnetization in adjacent sheets is antiparallel. The magnetic axis is [110]. The wall in A is I(001)II and that in B is I(110)II.

The rhombohedral angle of NiO at $300^{\circ}K$ has been given by Slack (1960) from X ray measurement to be $90^{\circ}4.2'$. Also a measured value of facial tilt angle of the (112) plane across a T wall was given as $11\pm1'$, leading to a fractional change along {111} of 1.3×10^{-3}.

An X ray diffraction study of T domain distortion has been described by Kohn and Iida (1969). Their experimental arrangement is shown in Figure 3.6(a). When a given area of the specimen has a perfect crystal structure, a homogeneous straight line diffraction pattern is expected on the photographic film. When the adjacent areas are misoriented with respect to each other, the diffraction pattern shift of one area leads to an overlap or gap on the film. This is shown schematically in Figure 3.6(b). From the amount of shift, the angle of misorientation is estimated. The smallest detectable misorientation was about 0.3' arc. Observed misorientation angles for twin planes (010) and $(1\bar{1}0)$ were 10' and 7'. Other misorientations of about 1' were observed and were thought to be related to "images" of S walls, suggesting a spontaneous magnetostriction of about 10^{-4}.

In order to investigate the sensitivity attainable with a single crystal and geometrical slit arrangement a single crystal diffractometer was constructed at Durham University. The collimation of the primary beam was made by two vertical slits which were 30μm and 80μm wide, separated by 90cms. The horizontal divergence of the beam then was not less than 30 seconds of arc. With the {444} reflection and $MoK\alpha_1$ radiation, not only was the $K\alpha$ doublet separated, at 14' arc, but a splitting of the $K\alpha_1$ peak of slightly more than 6' arc was observed. The width of the beam incident on the crystal was estimated to be about 100μm, wider than the 10μm T domain width which has been quoted by other workers. It is thought that this splitting was related to some T wall misorientation. However, the useful sensitivity of the arrangement was thought to be at its limit at this stage.

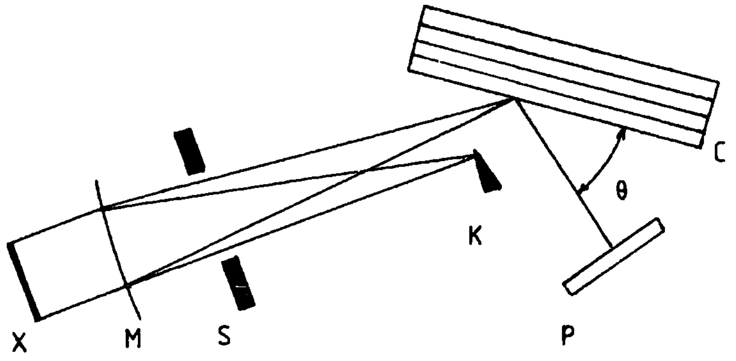

Fig.3.6(a) Sketch of X ray diffraction arrangement.

X Linear X ray source (Mo $K\alpha_1$)

M Bent quartz plate monochromator, radius 200 mm

S Slit

C Specimen mounted on a holder rotatable around the vertical axis

P Photographic plate

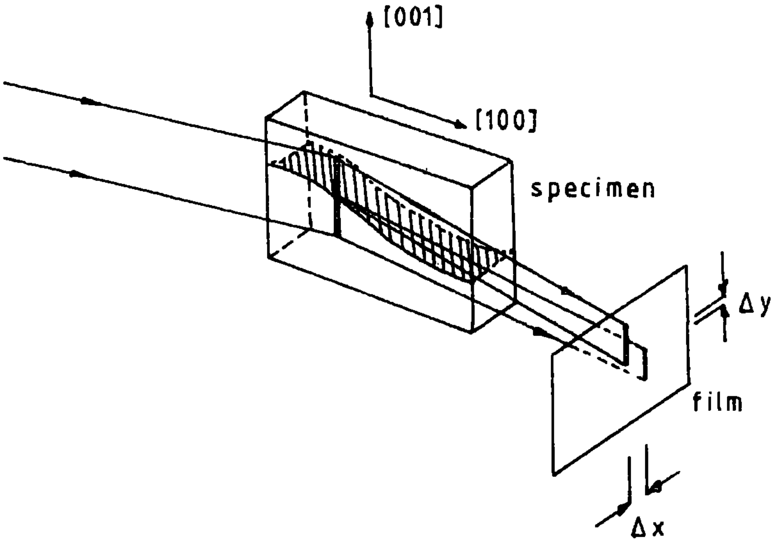

Fig.3.6(b) A schematic illustration of a shift of the pattern due to the misoriention of the lattice.

The magnetic anisotropy, magnetostriction and magnetic domain walls for the case of S domains have been treated both theoretically and experimentally by Yamada (1966). It was shown that the magnetostrictive distortions are given by an orthohombic deformation $e_{xx}-e_{yy}$ and a monoclinic deformation e_{zx}. The values obtained experimentally were $(9 \pm 3) \times 10^{-5}$ and $(1.6 \pm 1) \times 10^{-5}$ respectively. The experimental arrangement shown in Figure 3.7 involved a combination of double crystal (described in Chapter 4) and Berg Barrett topography (described recently by Tanner (1976)). The results did not agree with the predicted values of 2.4×10^{-4} and -1.5×10^{-4} respectively. It was also pointed out that the value of the orthorhombic deformation was larger than that determined from other methods of measurement at that time. Crystal imperfections were said to be partly responsible, and also the amount of spontaneous magnetostriction seemed to change locally depending upon the strain distribution produced by the crystal inperfections. It was stated that the value of the striction obtained by measuring "overall" strain may be said to have become smaller as compared with the value obtained by measuring "local" strain, as in the case of Yamada's work. Nakahigashi et al. (1975) repeated measurements similar to those above using Berg Barrett topography. The values obtained for the deformations were larger and of the correct sign as predicted theoretically by Yamada. The improved results were explained by the better quality of crystals used compared with Yamada's experiment.

3.6 Low magnetostriction measurement

It has been seen so far that magnetostrictive distortions of the order 10^{-3} may be deduced by using fairly simple monocrystal techniques such as the powder method and the single crystal goniometer. For values of the order 10^{-4}, the Lang technique has been used, whilst for deformations approaching values below this, which will be described in detail in Chapter 4,

Fig.3.7

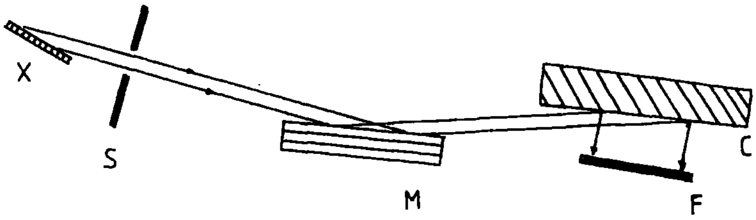

Schematic drawing of double crystal arrangement used by Yamada et al. (1966)

X X ray source

S Slit

M Ge monochromator

C Specimen

F Photographic film.

Table 3.2 Magnetostriction of RFe_2 Compounds. Clark et al. (1976).

	$\lambda_{111} \times 10^6$
$TbFe_2$	2460
$SmFe_2$	-2100
$DyFe_2$	1260
$ErFe_2$	- 300

a double crystal method has been used. The more typical value of magnetostriction of about 10^{-5} has been measured by Bradler and Polcarova (1972) who studied the relative inclination of the lattice planes on either side of 90° domain wall in Fe-3% Si. The experimental arrangement used is shown in Figure 3.8(a). The second crystal was rotated through the reflecting position and the intensity of the reflected beam was measured by a scintillation counter. The result of their measurement is shown by the curve in Figure 3.8(b). Also topographs were taken at the different angular positions and the blackening recorded for two neighbouring domains was studied with a photometer; this led to a similar curve. From the separation of the decomposed curve, a value of λ_{100} was found to be 2.7×10^{-5}, in agreement with other authors' results. It was pointed out that errors in the rocking curve widths observed were probably due to a small misalignment of the crystals and an uncertainty in reading the angle of crystal rotation, the total error being 2". Thus it was claimed that the magnetostriction value quoted does not exceed the accuracy of those values given by other methods.

All the methods of magnetostriction measurements discussed in this chapter have the common advantage that no magnetic field is required in deducing the values of spontaneous magnetostriction. The case where only 180° walls exist is discussed in the following chapter. The previous methods may not be applied to this case, as has been indicated.

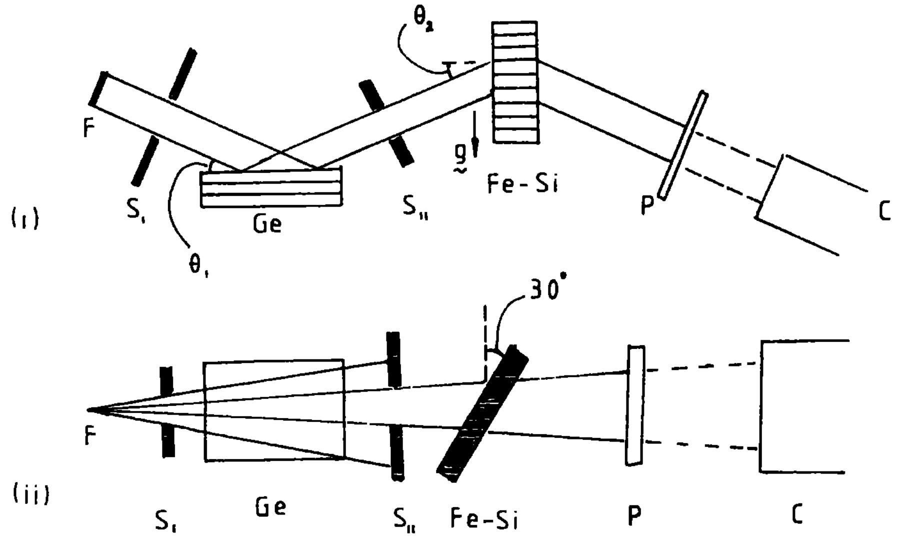

Fig.3.8(a) Schematic diagram of double crystal arrangement used by Bradler and Polcarova (1972). (i) plan, (ii) elevation. F, focus, S_I, S_{II} slits, P, photographic plate, C, counter.

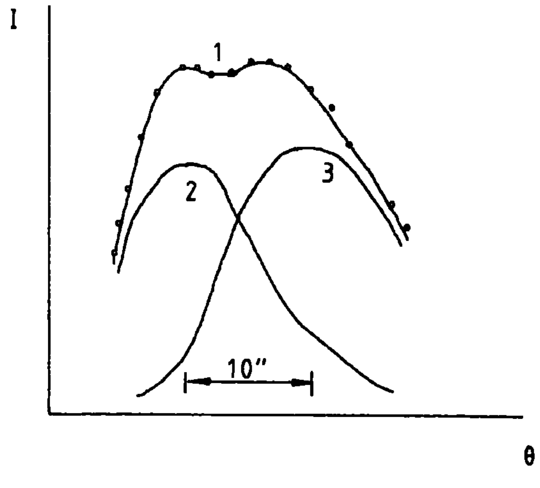

Fig.3.8(b). 1, measured reflection curve. 2 & 3 obtained by numerical decomposition of curve 1.

Chapter 4

Proposed method of magnetostriction measurement and review of double crystal diffractometry

4.1.1 The use of a double crystal X ray diffractometer for the measurement of magnetostriction

The disadvantages of measuring magnetostriction by the most widely used technique, the resistance strain gauge, have been outlined in Chapter 2. An important point is that the method allows just indirect contact with the crystal lattice planes. The use of X ray diffraction techniques to measure magnetostriction, as described in Chapter 3, provides one way of overcoming this difficulty. The successful use of X rays requires crystals of good lattice perfection. However, once this requirement is fulfilled, the fundamental nature of the results obtained may be emphasised.

One of the drawbacks in using the X ray diffraction techniques which have been discussed is that they may not be applied to the measurement of the magnetostrictive distortion in crystals which contain only 180° magnetic domain walls.

It can be seen then that there is room for at least one further measurement technique which may be entirely different from those already discussed, or which may be based on some combination of aspects of the two mentioned above.

The basis of the measurement technique used, and which is being described in this thesis, can be seen through a differentiation of the Bragg equation which keeps the wavelength, λ, constant.

$$\lambda = 2d \sin \Theta$$

$$0 = 2d \cos \Theta \Delta\Theta + 2\Delta d \sin \Theta$$

$$\frac{+\Delta d}{d} = \frac{-\Delta\Theta}{\tan \Theta} \qquad (4.1)$$

This equation relates the fractional change in lattice spacing, $\Delta d/d$, to the change in Bragg angle, $\Delta\Theta$, which occurs when the lattice spacing is changed by Δd. When a crystal is mounted on a diffractometer and rotated through the Bragg angle, the rocking curve represents the relation between the Bragg reflected X ray intensity, I, recorded in the detector, and the rotation angle, Θ. From Figure 4.1(a) it can be seen that the maximum change in intensity for a change $\Delta\Theta$ occurs on either flanks of the curve.

A magnetic field of sufficient strength to saturate a magnetic crystal can be rotated to change the direction of magnetization in the crystal. If the crystal is set on the flank of the rocking curve, the fractional change in lattice spacing, $\Delta d/d$, which accompanies the rotation of the magnetization, may be related through equation (4.1), and the rocking curve, to the change in the reflected X ray intensity.

For a typical value of $\Delta d/d$ of 10^{-5} and a Bragg angle of 45^{o} it can be seen that the value of $\Delta\Theta$ is about 2 seconds of arc. For the sensitivity required to measure $\Delta\Theta$ in the way described, rocking curves of the order of 10 seconds of arc width are needed. It has been seen in Chapter 3 that Polcarova and Bradler (1972) obtained narrow rocking curves by using a double crystal X ray diffractometer, and such an instrument was employed in the work of this thesis. The general theory of the double crystal diffractometer is described in section 4.2. The geometry of the experimental arrangement is shown in Figure 4.1(c).

4.1.2 Previous X ray techniques involving an applied magnetic field

In an X ray study of ferromagnetic domains in cobalt zinc ferrite, Merz (1960) described his magnetostriction measurement technique which involves essentially the same principles as those described above. However, there are some important differences between his work and the project described here.

Merz observed domains in cobalt zinc ferrite crystals using a double crystal diffractometer and the Berg Barrett method. The crystals had been magnetothermally annealed, such treatment leaving the magnetization in a known direction. A magnetic field was applied perpendicular to this direction and the crystal was rotated until the domains which had been shown to be reflecting in the original Berg Barrett micrographs were again shown to be Bragg reflecting. From the rotation he deduced a value for the magnetostriction.

Although a double crystal camera had been used here, no special mention was made of the high sensitivity which may be achieved with such an instrument. In fact, it was stressed that a material with a large magnetostriction (the value of $\Delta\ell/\ell$ for cobalt zinc ferrite is -335×10^{-6}) was deliberately chosen, and so the sensitivity aspect of the experimental arrangement was essentially ignored. The minimum width in any of the rocking curves which were recorded was 63 seconds of arc, indicating that the crystal lattice perfection was not of the highest possible.

The magnetic field used in Merz's work had a maximum achievable value of 5000 Oe. In Chapter 5 the magnet used in the present work will be described and the magnetic field obtainable will be shown to be considerably higher. Thus from the point of magnetic fieldstrength alone, the present apparatus to be described may be applied to a wider choice of materials.

It should perhaps be pointed out that experiments studying the effects of a magnetic field on the reflection of X rays from a crystal set in the Bragg condition have quite a long history. de Broglie (1913) performed an experiment along these lines and "Physical Review" records a series of such experiments by Compton and Trousdale (1915), Compton and Rognley (1920), Becker (1922), Yensen (1928) and Stearns (1930). All were designed to determine the nature of the ultimate magnetic particle. None of the experiments was successful in observing any change in Bragg reflected X rays when a magnetic field (typically 1000 Oe) was applied to the crystal lattice.

4.2 Theory of the double crystal diffractometer

4.2.1 Introduction. The geometrical arrangement of the double crystal diffractometer has been referred to in several previous sections. Generally it has been seen that X rays are Bragg reflected from one crystal, the reference, and then the X rays are further Bragg reflected from a second crystal, the specimen. The advantage of a double crystal diffractometer over a single crystal instrument is principally due to the greater angular resolving power attained. This increase is caused by the selective action of the first crystal upon the incident beam. Monochromatic constituents of it are diffracted in parallel bundles in the beam leaving the crystal.

The theory describing the operation of a double crystal diffractometer was presented by Compton and Allison (1935). From this, some of the elementary properties of the instrument may be seen. In the following, a resumé of that theory which applies to the setting of the diffractometer used in the work of this thesis will be given. A general equation for the instrument will be developed. The functions appearing in this equation depend in part on certain angles which are important in the operation of the instrument. Thus these angles, together with some assumptions as to the experimental arrangement will be considered first. Finally it will be shown how the important properties of the instrument may be obtained from the general equation.

4.2.2 Settings of the diffractometer

It is assumed that the two axes of rotation of the crystals lie in a vertical plane, and that they are accurately parallel. Further, it is necessary that the reflecting crystal planes are parallel to these axes. The discussion is applicable to the case of the X rays being reflected from the crystal surface, but is not adequate to cover the case of transmission through a crystal slab.

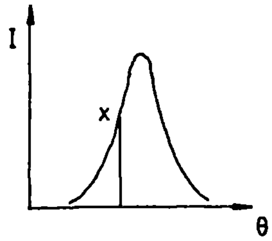

Fig. 4.1(a). Rocking curve showing the position of the crystal on the flank of the curve used for high strain sensitivity.

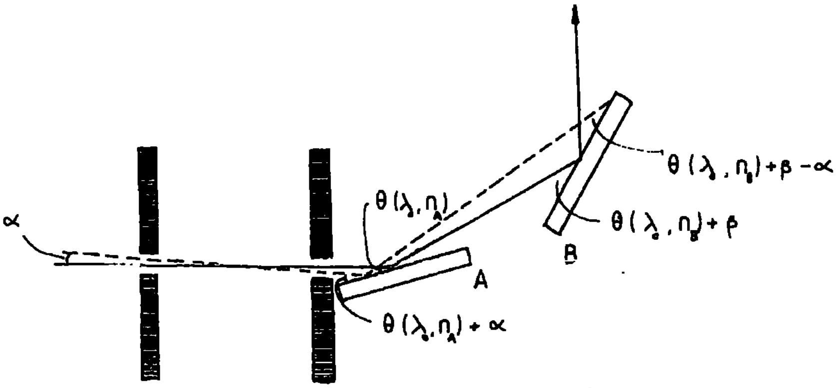

Fig 4.1(b). Type 1, (+,+) position of double crystal diffractometer.

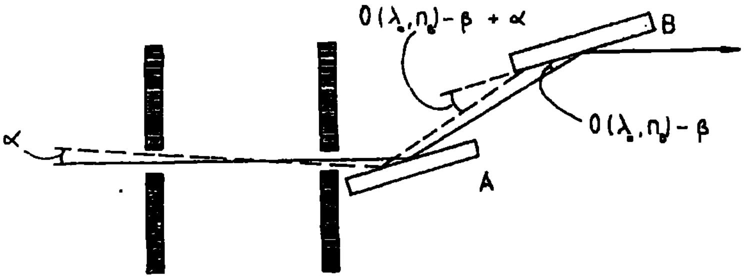

Fig. 4.1(c). Type 2, (+,-) position of double crystal diffractometer. For zero dispersion the crystals are parallel and their lattice spacings are equal.

The positions of the two crystals fall into two main classes. These are shown in Figures 4.1 (b) and (c). The first type is the (+,+) or (n,n) setting. Here, the rays incident on the reference crystal and leaving the specimen crystal are on the same side of the ray between the crystals. The second type is the (+,-) or (n,-n) setting. Here the rays incident on the reference crystal and leaving the specimen crystal are on opposite sides of the ray between the crystals. The (+,-) setting was used in the work reported here.

4.2.3 Beam divergence

The vertical divergence, ϕ, of the ray is the angle made with its projection on a plane which is perpendicular to the axes of the instrument. The functions appearing in the instrument are symmetrical with respect to rays lying above or below this plane.

The horizontal divergence, α, of a ray is the angle made with its projection on a vertical plane containing the central ray, the ray which passes through the geometrical centre of the slit aperture. The value of α may be defined as positive or negative depending on whether the glancing angle made by the ray on the reference crystal is greater or less than the glancing angle of the central ray.

4.2.4 Rays incident upon the reference crystal

Three quantities characterize a ray in the beam incident upon the reference crystal. These are (λ,α,ϕ), the wavelength, and the horizontal and vertical divergences respectively. The glancing angle of such a ray may be found in terms of α and ϕ. If the ray with $\alpha = \phi = 0$ makes the glancing angle $\phi(\lambda_o,\eta_A)$, then for small α and ϕ, it can be seen from Figure 4.2 that the required glancing angle is:

$$\phi(\lambda_o,\eta_A) + \alpha - \frac{1}{2}\phi^2 \tan\Theta\,(\lambda_o,\eta_A) \qquad (4.2)$$

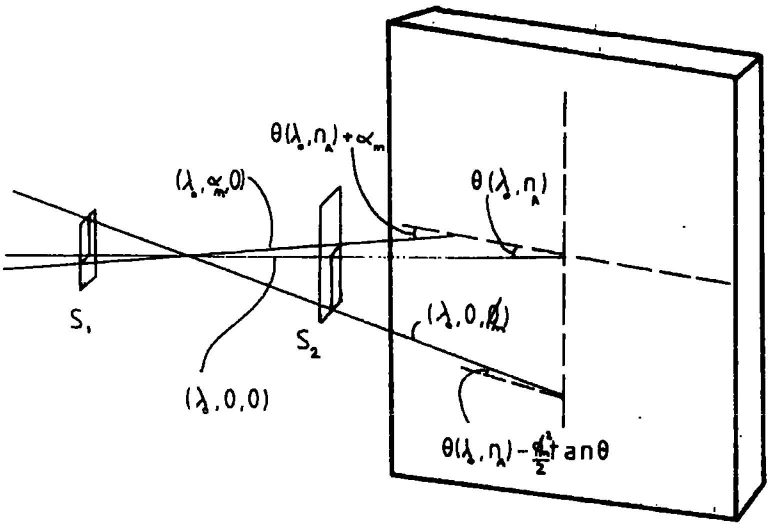

Fig.4.2. Incident ray on first crystal may be designated by three symbols (λ,α,ϕ). Glancing angles shown are those made by rays $(\lambda_0,\alpha_m,0)$ and $(\lambda_0,0,\phi_m)$ when the glancing angle of the central ray $(\lambda_0,0,0)$ is $\theta(\lambda_0,n_A)$.

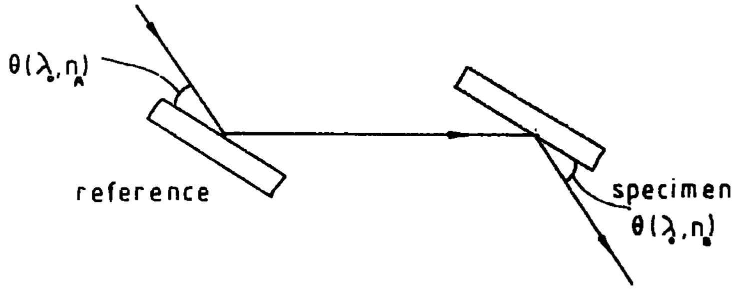

Fig.4.3. For $n_B > n_A$, the specimen crystal passes from shorter to longer wavelengths when rotated clockwise.

λ_o may be thought of as some characteristic wavelength such as the centre of a spectral line or an absorption limit.

The deviation of the angle $\Theta(\lambda,\eta_A)$ from the glancing angle (λ,α,ϕ) is now required. This deviation is the argument of the reference crystal diffraction pattern function which will appear in the general equation. $\Theta(\lambda,\eta_A)$ is the reference angle corresponding to λ in the n^{th} order. It may be written

$$\Theta(\lambda,\eta_A) = \Theta(\lambda_o,\eta_A) + (\lambda - \lambda_o)\frac{\partial}{\partial\lambda_o}\Theta(\lambda_o,\eta_A) \qquad (4.3)$$

The required angular deviation is the difference of (4.2) and (4.3). If the diffraction pattern of the reference crystal approaches that of a perfect crystal and this deviation,

$$\alpha - \frac{1}{2}\phi^2 \tan\Theta(\lambda_o,\eta_A) - (\lambda - \lambda_o)\frac{\partial}{\partial\lambda_o}\Theta(\lambda_o,\eta_A) \qquad (4.4)$$

is more than a few seconds of arc, then the intensity of reflection of ray (λ,α,ϕ) from the reference will be very small. Theoretically, however, each ray incident on the reference is reflected at least to some extent.

4.2.5 Rays incident on specimen crystal

It is assumed that the method of operation is such that the rocking curve is obtained from rotation of the second crystal alone. $\Theta_o(\lambda_o,\eta_B)$ is the exact Bragg angle obtained from the Bragg equation when the wavelength λ_o is reflected in order η_B. The reflection of a given wavelength λ_o will take place through certain small ranges about the glancing angle (Θ_o,η_B). It is convenient to speak of the deviations of the specimen from this characteristic angle. The deviation which it is necessary to consider is very small and is represented by β. As with α, this may be decided as being positive or negative by definition.

Let the specimen crystal be set so that its angular deviation is β from a position where the glancing angle of the central ray upon it is

$\Theta\ (\lambda_o,\eta_B)$. The glancing angle of the central ray upon the specimen crystal is then $\Theta\ (\lambda_o,\eta_B) - \beta$, and the glancing angle made by the ray (λ,α,ϕ) is:

$$\Theta\ (\lambda_o,\eta_B) - \beta + \alpha - \frac{1}{2}\,\phi^2 \tan\Theta\ (\lambda_o,\eta_B) \qquad (4.5)$$

The deviation of the glancing angle of this ray from the angle $\Theta\ (\lambda,\eta_B)$ is

$$-\beta + \alpha - \frac{1}{2}\,\phi^2 \tan\Theta\ (\lambda_o,\eta_B) - (\lambda - \lambda_o)\,\frac{\partial}{\partial\lambda_o}\,\Theta\ (\lambda_o,\eta_B) \qquad (4.6)$$

This deviation is the argument of the single crystal diffraction pattern function of the specimen crystal.

4.2.6 Power in element of incident beam

The power in an element of the beam incident on the reference crystal may be written

$G(\alpha,\phi)\ J(\lambda - \lambda_o)\ d\alpha\, d\lambda\, d\phi$, where the element has wavelengths between λ and $\lambda + d\lambda$, and horizontal and vertical divergences $d\alpha$ and $d\phi$ respectively in the vicinity of values α and ϕ. The geometrical function G depends on such parameters as slit aperture shape, and intensity distribution in the focal spot. The function J gives the distribution of energy in the incident spectrum.

4.2.7 General equation

After diffraction of this incident beam from the reference, the power in the resultant beam will depend on the deviation of the glancing angle from the angle $\Theta\ (\lambda,\eta_A)$. Such a dependence is given by the single crystal diffraction pattern function, which is called the C function. Hence the power in the elementary beam after diffraction from the reference crystal can be written:

$$G(\alpha,\phi)\ J\ (\lambda - \lambda_o)\ C_A\left[\alpha - \frac{1}{2}\,\phi^2 \tan\Theta\ (\lambda_o,\eta_A) - (\lambda - \lambda_o)\,(\partial/\partial\lambda_o)\ \Theta\ (\lambda_o,\eta_A)\right] d\lambda\, d\alpha\, d\phi \qquad (4.7)$$

This is subsequently diffracted by the second crystal. Again the diffracted beam depends on the deviation from the glancing angle $\Theta\ (\lambda_o,\eta_B)$, and this dependence is given through the C function for the specimen crystal. Upon integration, the entire intensity reflected from the specimen is then written:

$$P'(\beta) = \int_{-\phi_m}^{\phi_m} \int_{\lambda_{min}}^{\lambda_{max}} \int_{-\alpha_m}^{\alpha_m} G(\alpha,\phi)\ J\ (\lambda-\lambda_o)$$
$$C_A\ \left[\alpha - \frac{1}{2}\ \phi^2\ \tan\ \Theta\ (\lambda_o,\eta_A) - (\lambda-\lambda_o).\frac{\partial}{\partial\lambda_o})\ \Theta\ (\lambda_o,\eta_A)\right]$$
$$C_B\ \left[-\beta+\alpha-\frac{1}{2}\ \phi^2\ \tan\ \Theta(\lambda_o,\eta_B) - (\lambda-\lambda_o)(\partial/_{\partial\lambda_o})\ \Theta\ (\lambda_o,\eta_B)\right]$$
$$d\alpha d\lambda d\phi \qquad (4.8)$$

This general equation for the double crystal instrument is written assuming that the change in the C functions with wavelength may be reflected. This is the same as assuming that the range of wavelengths covered in any rocking curve is very small. The limits of λ in any practical case do not extend farther than the limits of the range of wavelengths reflected by the reference crystal, which depend upon the horizontal divergence of the beam incident upon the reference.

4.2.8 Dispersion

In order to find the dispersion expression, the limiting case is considered in which the diffraction patterns of the two crystals are so narrow that no appreciable contribution to $P'(\beta)$occurs except when the arguments of both C functions are zero. Such an assumption is, however, unphysical. It corresponds to an elementary treatment in which it is assumed that there is a perfectly discrete Bragg angle for any incident wavelength. If such a case were to be true, then no power would be diffracted from a divergent incident beam at any position.

The arguments are equated to zero:

$$\alpha - \frac{1}{2}\ \phi^2\ \tan\ \Theta\ (\lambda_o,\eta_A) - (\lambda-\lambda_o)(\partial/_{\partial}\lambda_o)\ \Theta\ (\gamma_o,\eta_A) = 0 \qquad (4.9)$$

$$-\ \beta + \alpha - \frac{1}{2}\ \phi^2\ \tan\ \theta\ (\lambda_o,\eta_B)-(\lambda-\lambda_o)(\partial/\partial\lambda_o)\theta\ (\lambda_o,\eta_B) = 0 \qquad (4.10)$$

α is eliminated from these two expressions, and the following equation is obtained:

$$\beta - \frac{\phi^2}{2}\left[\tan\theta\,(\lambda_o,\eta_A) - \tan\theta\,(\lambda_o,\eta_B)\right] - (\lambda-\lambda_o)\left[\frac{\gamma\Theta(\lambda_o,\eta_A)}{\gamma\lambda_o} - \frac{\gamma\theta(\lambda_o,\eta_B)}{\gamma\lambda_o}\right] = 0 \qquad (4.11)$$

The symbol D is introduced, where

$$D = \frac{\partial\Theta(\lambda_o,\eta_A)}{\partial\lambda_o} - \frac{\partial\theta(\lambda_o,\eta_B)}{\partial\lambda_o} \qquad (4.12)$$

From a differentiation of Bragg's equation, $\eta\lambda = 2d \sin\theta$, D may be written as:

$$D = \frac{\eta_A}{2d\cos\theta(\lambda_o,\eta_A)} - \frac{\eta_B}{2d\cos\theta(\lambda_o,\eta_B)} \qquad (4.13)$$

or, $$D = \frac{1}{\lambda_o}\left[\tan\theta(\lambda_o,\eta_A) - \tan\theta(\lambda_o,\eta_B)\right] \qquad (4.14)$$

If equations (4.13) and (4.14) are substituted in equation (4.11), then the following may be written:

$$\beta = \frac{1}{2} D\lambda_o\phi^2 + D(\lambda-\lambda_o) \qquad (4.15)$$

The dispersion of the double crystal diffractometer when the specimen is rotated is defined naturally as $d\beta/d\lambda$. If equation (4.15) is differentiated in this way then

$$\frac{d\beta}{d\lambda} = D, \qquad (4.16)$$

that is, the dispersion may be written

$$\text{Dispersion} = \frac{d\beta}{d\lambda} = \frac{1}{\lambda_o}\left[\tan\theta(\lambda_o,\eta_A) - \tan\theta(\lambda_o,\eta_B)\right] \qquad (4.17)$$

Thus for the (+,-) position, where $\eta_B > \eta_A$, the dispersion is negative. For the arrangement shown in Figure 4.3 the sense of rotation of the specimen crystal to pass from shorter to longer wavelengths is clockwise, and vice versa for positive dispersion.

4.2.9 Properties deduced from general equation

If it is assumed that the C functions of the two crystals are identical, i.e. $C_A = C_B = C$, and $\theta(\lambda_o,\eta_A) = \theta(\lambda_o,\eta_B) = \theta$, then the general equation is written:

$$P'(\beta) = \int_{-\phi_m}^{\phi_m} \int_{\lambda_{min}}^{\lambda_{max}} \int_{\alpha_m}^{\alpha_m} G\,(\alpha,\phi)\; J(\lambda-\lambda_o) \tag{4.18}$$

$$C\left[\alpha-\tfrac{1}{2}\phi^2\tan\theta-(\lambda-\lambda_o)\left({}^{\partial\theta}/\partial\lambda_o\right)\right]$$

$$C\left[\alpha-\beta-\tfrac{1}{2}\phi^2\tan\theta-(\lambda-\lambda_o)\left({}^{\partial\theta}/\partial\lambda_o\right)\right]d\alpha\, d\lambda\, d\phi$$

To interpret this expression, it is necessary to consider the characteristics of the functions C, J and G. If the crystals are nearly perfect, C is negligibly small everywhere except in a narrow range of its argument close to zero. The range in crystals of good lattice perfection is close to the width of the single crystal diffraction pattern, which is about 10^{-5} radians.

$G(\alpha,\phi)$ may be considered to be the product of two functions:

$$G(\alpha,\phi) = G_1(\alpha)\; G_2(\phi) \tag{4.19}$$

G_1 and G_2 are finite over a range of some minutes of arc, which is usually the extent of the horizontal and vertical divergence of the beam. Thus the range over which these functions are finite is about 100 times the range over which C is finite. In most cases the term $\frac{1}{2}\,\phi^2\tan\theta$ is very small, of about diffraction pattern width order.

Some of the characteristics of the rocking curves obtained in the (+,-) parallel setting may be obtained from equation (4.18) if the above considerations are kept in mind.

Firstly, for any monochromatic constituent of the beam of wavelength λ, the effective values of α lie very close to the value $(\lambda-\lambda_o)(\partial\theta/\partial\lambda_o)$. If this were not true, then the argument of the first C function would be large, and thus the function itself very small. This then is what is meant in saying that the action of the reference crystal is to separate the beam into monochromatic parallel bundles.

Secondly, the value of the function $P'(\beta)$ can only be significantly different from zero over a small range of the deviation β. If β were large, then in order for the second C function in equation (4.18) to have a reasonable value, $\alpha - (\lambda-\lambda_o)(\partial\theta/\partial\lambda_o)$ would need to be large, so that the total argument could be sufficiently small. But if this were the case, then the first C function would be negligible since its argument would be large, and thus the entire integrand function would be negligible. Hence the parallel position rocking curves have widths comparable to those of the diffraction pattern of a single crystal.

Thirdly, it can be seen from equation (4.17), with $d_A = d_B$ that the dispersion for the setting under discussion is zero when $n_A = n_B$. This can be further seen by noting that the effective wavelength range reflected by the specimen crystal is at any position, β, independent of β, and covers the relatively large range:

$$\lambda = \lambda_o \pm \frac{\partial\lambda_o}{\partial\theta}\alpha_m \qquad (4.20)$$

This is so, since for a very small value of β, it is sufficient that $\alpha - (\partial\theta/\partial\lambda_o)(\lambda-\lambda_o)$ be small for an appreciable value of the integrand product to be obtained. This condition is satisfied by values of λ very close to the value $\lambda = \lambda_o + (\partial\lambda/\partial\theta)\ \alpha$, and since the range of α is $-\alpha_m < \alpha < +\alpha_m$, equation (4.20) may be deduced. Therefore, in the (+,-) parallel setting the beam entering the detector from the specimen crystal at any position on the rocking curve contains effective contributions from every wavelength reflected from the reference crystal, which is another way of saying that the dispersion is zero.

Finally, integration of equation (4.18) with respect to α may be considered, whilst λ, ϕ and β are held constant. Thus the entire integrand is considered to be a function of α. It has been seen that the only pertinent values of α under these conditions lie in a narrow range near $(\partial\theta/\partial\lambda_o)(\lambda-\lambda_o)$. The change of the slowly varying function $G_1(\alpha)$ is neglected, and so

$$G_1(\alpha) = G_1\ ((\lambda-\lambda_o)\,\partial\theta/\partial\lambda_o) \qquad (4.21)$$

Also, the angular range in which the important values of α are found, λ and ϕ being constant, is several seconds of arc, whilst the range of α given by the limits of the integral is $2\alpha_m$, which is several minutes of arc. Hence the limits of the α integration may be extended to ± ∞ without the value of the integral being affected, If the limits are extended to ± ∞, then use may be made of the theorem which states that if the function F is finite and continuous everywhere then

$$\int_{-\infty}^{\infty} F(\alpha)\,d\alpha = \int_{-\infty}^{\infty} F(\alpha - a)\,d\alpha \qquad (4.22)$$

where a is any constant. If the argument of the first C function of equation (4.18) is replaced by $k\ell$, where k is a constant and ℓ is the variable. then equation (4.18) may be rewritten:

$$P'(\beta) = k\int_{\gamma_o - (\partial\lambda_o/\partial\Theta)\alpha_m}^{\lambda_o + (\partial\lambda_o/\partial\Theta)\alpha_m}\int_{-\phi_m}^{\phi_m} G_1((^{\partial\Theta}/\partial\lambda_o)(\lambda-\lambda_o))G_2(\phi)J(\lambda-\lambda_o)\,d\phi\,d\lambda$$
$$\int_{-\infty}^{\infty} C(\ell)C(\ell-\beta)\,d\ell \qquad (4.23)$$

$$\text{or } P'(\beta) = K\int_{-\infty}^{\infty} C(\ell)C(\ell-\beta)\,d\ell \qquad (4.24)$$

The constant K is proportional to the power of the beam incident on the reference crystal. The change to the variable ℓ may be interpreted as a change in the unit of angle, the unit being k radians.

Using the theorem mentioned above then, the important result is obtained that the shape of the rocking curve in the (+,-) parallel positions is independent of the width or the height of the aperture slits and of the spectral energy distribution of the radiation used. This assumes that the diffractometer is adjusted correctly, with the axis of rotation being parallel to and passing through the crystal faces.

In summary then, the properties of the diffractometer as deduced from the general equation of the instrument in the (+,-) parallel setting may be given as follows:

1. The action of the reference crystal is to separate the beam into monochromatic parallel bundles
2. The parallel position rocking curves have widths comparable to those of the diffraction pattern of a single crystal, typically 10^{-5} radian
3. The dispersion is zero
4. The shape of the rocking curve is independent of the height or width of the aperture slits, and of the spectral energy distribution of the radiation used.

4.3 Measurements with the double crystal arrangement

4.3.1 Early measurements

The first measurements using a double crystal diffractometer were made to investigate the quantities : coefficient of reflection and half width at half maximum of the rocking curve. The important works on the coefficient of reflection were those by Compton (1917), Bragg et. al. (1921), Davis and Stempel (1921). The crystals used were natural crystals of calcite and rock salt. Compton measured for this the ratio of the energy of wavelength λ reflected from the second crystal to the incident energy of the same wavelength. There was some debate as to what should be defined as the coefficient of reflection. Some surprise was expressed by Davis, at the large value of the percentage reflection when the crystals were in the parallel positions. His results gave a percentage reflection greater than 50%.

Rocking curve widths were investigated for various characteristic X ray wavelengths, and comparisons made with theoretically obtained values. Theoretical values were obtained, for example, by calculating the value of P (β = 0) (see equation (4.8)) and then finding the value of β for which $\frac{1}{2}$ P (β = 0) would be obtained. Some typical results of Allison (1932) and by Parratt (1932) are shown in Table 4.1. It was noted by Richtmyer et.al. (1933) that the rocking curve widths decreased after suitable polishing and etching of calcite. An important point regarding early work was that finely sensitive measurements were made with cleaved natural crystals.

4.3.2 Double crystal topography

The first measurements made with the double crystal diffractometer concentrated on comparing experimental results with theoretical predictions for the performance of the instrument. The X ray beam reflected from the second crystal was monitored by an ionisation detector and no variation across the section of the reflected beam was investigated. The double crystal diffractometer was developed by Bond and Andrus (1952) as an instrument for examining the topography of atomic planes. The resolution of the method went beyond that obtained by Wooster and Wooster (1945) who used just a single crystal arrangement to investigate a number of diamonds. The arrangement used by Bond and Andrus is shown in Figure 4.4(a). It can be seen here that although the reflecting planes of the two crystals are parallel, the setting is asymmetric. The use of asymmetric reflection on the first crystal acts to broaden the reflected beam and thus a wider field of the specimen surface may be inspected. If symmetric reflections are used, then just a narrow band of the crystal is scanned. The K characteristic

Table 4.1 Results obtained by Allison and Parratt on w (width at half height) for calcite specimens in the (1,1) position; values are given for three samples together with some calculated values.

Radiation	w (calcite V)	w (calcite III)	w (calcite II)	w (calculated)
Mo $K\alpha_1$	7.2"	2.6"	3.9"	2.3"
Cu $K\alpha_1$	7.8"	4.9"	5.6"	4.9"

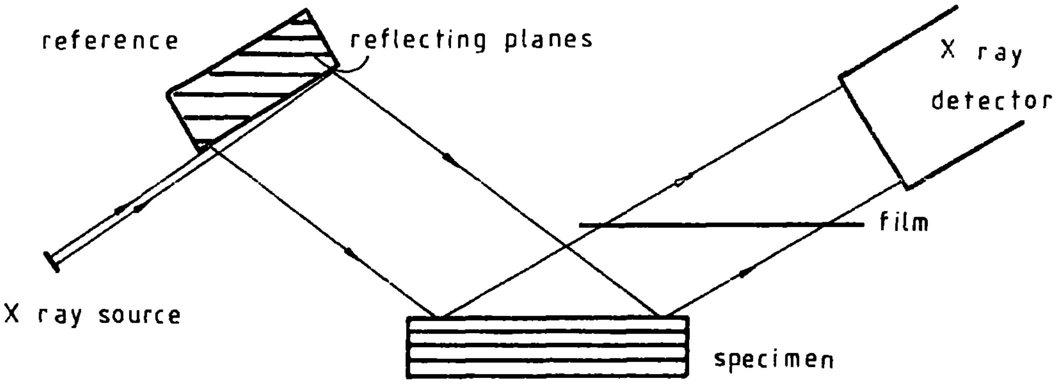

Fig.4.4(a). Double crystal arrangement used by Bond and Andrus (1952).

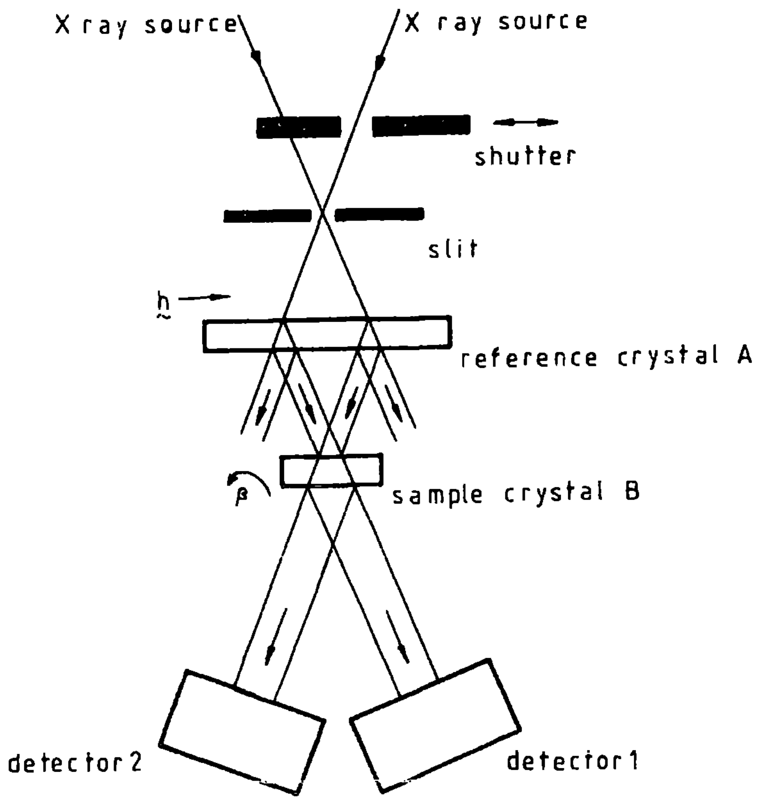

Fig. 4.4(b) Multiple Bragg reflexion arrangement used by Hart (1968).

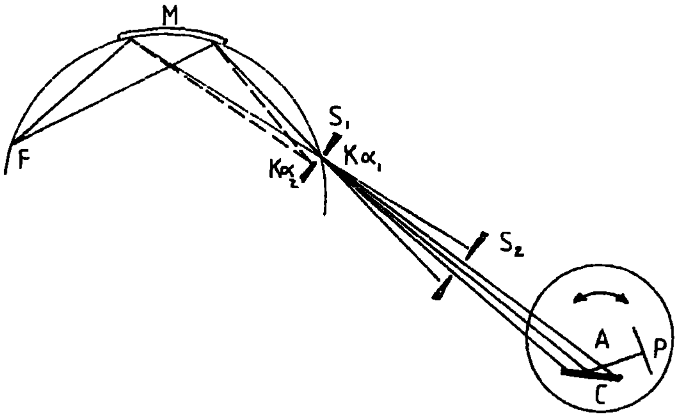

Fig. 4.4(c). Schematic diagram of experimental arrangement used by Kohra and Takano (1968). F, Xray source, M, monochromator, S_1, slit for selecting $K\alpha_1$, S_2, slit, C, specimen, P, photographic plate, A, rotation axis.

line is usually used when the topographs are taken, since it is intense compared with the rest of the spectrum. However, this line consists of a doublet, $K\alpha_1$ and $K\alpha_2$, and these components reflect at slightly different angles. Hence two overlapping pictures are given unless the plate is placed as close to the specimen as possible, when the offset can be kept to a few thousandths of a centimetre.

In simple terms, if the reflecting planes of the two crystals are not parallel, no ray can be reflected from both crystals. If a minor part of the second crystal is slightly misorientated, this part will not reflect most strongly at the same angle setting as does the major part of the crystal. If the second crystal is rotated to make the minor part reflect most strongly, the major part reflects less strongly. The emulsion plate will show in each case from which part of the crystal the strong reflection came.

In any one exposure, if the crystal is set on the flank of the rocking curve, where the variation of intensity with angle is approximately linear, the relative change in intensity can be related to lattice distortion by the simple geometrical expression of Bonse (1962).

$$\frac{\Delta I}{I} = k \left(\tan \Theta \frac{\Delta d}{d} \pm \underset{\sim}{\eta}_g \cdot \underset{\sim}{\eta}_t \, \Delta\Theta\right) \qquad (4.25)$$

k is the slope of the rocking curve at the point where the crystal is positioned, typically 10^5. $\underset{\sim}{\eta}_g$ is a unit vector normal to the incidence plane. $\underset{\sim}{\eta}_t$ is a unit vector parallel to the tilt axis of the crystal. This expression is found to give a good description of most of the contrast observed in double crystal topographs.

Bond and Andrus used double crystal topography to study the imperfections in natural quartz crystals, which had remained invisible when ordinary tests such as etching and single crystal reflection had been used. The method was further adopted by Bonse and Kappler (1958) to study the strain field around dislocation outcrops in Germanium single crystals.

4.3.3 Device grade materials and highly perfect materials

Single crystals of naturally occurring quartz found the first large scale application in the manufacture of quartz oscillator plates, and have been used extensively in the optical industry for the construction of polarizing optical systems. Although effort is now put into growing crystalline quartz, earlier on, sufficiently perfect quartz crystals were available in large enough quantities for the needs of the oscillator industry. The same has not been the case for other technologically important materials. Isherwood and Wallace (1974) have pointed out that the far-reaching advances in materials technology in the past two decades have relied on the production of good quality single crystals. Production techniques developed by Dash (1958) who grew samples of Si, and Tweet (1958) who grew specimens of Ge, made possible the supply of these two materials in the dislocation and planar defect-free form. These materials have been essential for the transistor industry. Materials such as gallium arsenide (GaAs), indium antomonide (InSb), gallium phosphide (GaP), ($A\ell_2O_3$) and calcium tungstate ($CaWO_4$) which have been used for the production of optical components, microwave devices, lasers and radiation detectors also do not occur with high perfection in nature. They require a well controlled growth process. More recently rare earth iron and rare earth gallium garnets have been important in the production of magnetic bubble memory cells. Many methods by which crystal defects may be detected have been developed as crystal growing techniques have improved. Of these, the double crystal method is the most sensitive to minute lattice strain. It has been able to image strain regions in crystals of less than one part in ten millions. At this stage other techniques would render the appearance of a perfect structure.

Hart (1968a) has used an extension of the double crystal arrangement to make some high precision, non dispersive measurements of relative lattice parameters for Si. The arrangement is shown in Figure 4.4(b). The reference crystal and sample crystal are mounted on the two axes of a double crystal diffractometer, and rocking curves are obtained by rotating the sample. It can be seen that there are two sources and two detectors. The $(\eta,-\eta)$ rocking curve (from source 2 to detector 2) and the $(-\eta,\eta)$ rocking curve (from source 1 to detector 1) are recorded simultaneously. If both crystals have the same lattice parameter then both detectors record a peak simultaneously at the sample setting $\beta = 0$, when the Bragg planes of the two crystals are precisely parallel. When the two crystals have different lattice parameters, d_A and d_B, the two detectors record rocking curve peaks at different angular settings β of the sample crystal. It is noted that the instrument now operates in transmission. Through the Bragg law for the case of symmetric transmission, the expression $\Delta\beta = 2 \tan \Theta \, \Delta d/d$ (4.26) is obtained. The system is non dispersive, and rocking curves of 10^{-6} radian full width at half height may be attained. If the centroid positions are measured to within 0.1% of the peak width, then equality of Bragg angle can be detected to within 10^{-9} radian, which implies that equality of lattice parameter can be detected with uncertainties of one part in 10^{9}. Preliminary measurements were made on two Si wafers which were known to have lattice parameters equal to better than two parts in 10^{7}. From the displacement of the two rocking curves a value of $\Delta d/d$ of $1.2 \times 10^{-7} \pm 0.6 \times 10^{-7}$ was found.

A major trouble with sensitive measurements is that the actual measurable quantity is easily cloaked by some error in the system. In this particular case careful alignment of the two crystals is needed.

Various arrangements based on transmission through the crystals, or multiple reflections at the crystal surfaces may be used as extensions of the above, depending on the experimental requirements.

Silicon crystals grown by the Czochralski technique contain oxygen as an impurity, which leads to the formation of impunity bands perpendicular to the growth axis. Highly perfect low oxygen float zone silicon (LOPEX) crystals have predominant oxygen bands leading to lattice parameter fluctuations of only one part in ten millions. Hart (1968b) has used double crystal topography with high order Bragg reflections and short wavelength X rays to attain adequate strain sensitivity and high spatial resolution to observe these lattice parameter fluctuations. Two pairs of wafers were used, cut parallel to $(\bar{1}\bar{1}2)$ and $(1\bar{1}0)$ surfaces. With the first pair a full width at half height of only 0.34 seconds of arc was obtained, giving a rocking curve slope of $k = -6.3 \times 10^5$ and a contrast +1 for a lattice parameter fluctuation of $\delta d/d = -1.6 \times 10^{-8}$. The corresponding values for the second pair were 0.29 seconds, $k = 6.8 \times 10^5$ and $\delta d/d = +1.3 \times 10^{-8}$.

The topographic technique has been used by Baker, Hart et al. (1975) to study the variation in lattice parameter across crystals of GaAs containing various amounts of dopants of Si and Te. Topographs were taken of one side of the crystal, which was then rotated by 180° for a further topograph to be taken of the reverse side. The expressions for $\Delta I/I$ were obtained from optical density measurements on the two topographs and $\Delta d/d$ obtained after elimination of the term $\underset{\sim}{\eta}_g \cdot \underset{\sim}{\eta}_t \, \Delta\Theta$. Such measurements gave $\Delta d/d$ to 1 part per million at points 350μm apart along lines across the sample.

4.3.4 Measurement of lattice parameter differences between epitaxial layers and substrates

The double crystal diffractometer arrangement has been used by Hart and Lloyd (1974) to measure the difference in lattice parameter between a substrate of gadolinium gallium garnet and a layer of mixed garnet $Y_{2.2}Gd_{0.5}Yb_{0.3}Ga_1Fe_4O_{12}$ which was grown epitaxially onto it. The difference in lattice parameter for such materials has a value typically of ${}^{\delta d}/d > 10^{-4}$. In such a case the composite rocking curve which would be obtained from a substrate/layer system with a single crystal arrangement may be resolved into its two components with standard curve fitting routines. However the two rocking curves may be well resolved with considerable time saving when the double crystal arrangement is used. Typically a couple of hundred seconds separate the rocking curves which have widths typically of 13 seconds of arc for the substrate and 20 seconds for the film, and angular resolutions of about 1 second of arc were available with Hart's arrangement. Thus with careful alignment, accurate comparison of the lattice parameters become quite routine.

Similar measurements were made by Estop et al. (1976). Aluminium substituted gallium arsenide layers $A\ell_x Ga_{1-x} As$ were deposited on substrates of GaAs by liquid phase epitaxy. Both crystals have a different lattice parameter at room temperature, and a double crystal diffractometer was used to measure accurately the difference in lattice parameter between the epitaxic layer and the substrate.

4.3.5 Some variations of the double crystal arrangement

From the differential form of Bragg's equation, $\Delta d/d = -\Delta\Theta\cot\Theta$ it can be seen that as the angle Θ approaches 90°, the sensitivity of the instrument will increase accordingly. It is rare that allowed reflections with Bragg angles very close to 90° will be found if characteristic X radiation is used. In order to make use of the high sensitivity, white X rays may be used. Double crystal diffractometers based on this principle have been described by Sykora and Peisl (1970) and Bottom and Carvalho (1970). One of the problems associated with the arrangement is that the value of Θ needs to be known exactly. Practically speaking, this can be difficult. In Sykora's instrument the problem is overcome by keeping the angle constant. The system is then passed through the condition of non-dispersion and double Bragg reflection by varying the lattice parameter of one of the two crystals through an alteration of its temperature. A lattice parameter change of the other crystal caused by defects can then be determined from the temperature difference of the two crystals necessary to give a maximum scattered intensity.

A further problem lies in the X ray beam being absorbed along the path in the diffractometer. High Bragg angles imply high order reflections, which are of less intensity than those of low order. The X ray beam being white will be of relatively low intensity in any case. Absorption along the X ray path, which is quite long (about 3 metres here) is therefore a problem. The system then needs to be evacuated. With good crystals it has already been pointed out that in most cases adequately sensitive measurements may be made at a lower Bragg angle with characteristic radiations. Okazaki and Kawaminami (1972) have pointed out that high angle diffractometers are useful for accurate measurements on crystals of not so good quality. They used the instrument for measurement of the variation of the lattice constant of potassium nickel fluoride, $KNiF_3$, over a wide range of temperatures. One of the problems encountered was a geometrical one, that the low temperature crystal obstructed the beam so that the highest Bragg angle which could be used was less than 89°, but at this angle the X ray path is quite long. The Bragg angle used in Sykora's arrangement was 89.6°.

Kohra and Takano (1968) have described a modified arrangement of the double crystal diffractometer shown in Figure 4.4(c) which can be used for the topography of distorted crystals. The first crystal is bent. A divergent monochromatic beam is reflected from this. The source and focus of the reflected beam lie on a circle whose curvature is equal to that of the bent reference crystal. The reference crystal and photographic plate are rotated in an oscillatory fashion about the same axis. The resultant exposure on the plate is similar to a Lang topograph in detail. However in the latter method the angular divergence of the incident beam is reduced by a slit system to a few minutes of arc so only the $K\alpha_1$ component is diffracted from the specimen. Thus if a lattice plane misorientation goes beyond the angular divergence of the incident beam, then the part of the crystal affected will not diffract. In the method proposed by Kohra, all the distorted regions are passed through the diffraction condition as the specimen oscillates. The whole crystal can thus be studied. In principle, the facilities available with the diffractometer to be described in Chapter 6 could also be extended in use, beyond that described in this thesis, to include an arrangement such as Kohra's.

Chapter 5

The Electromagnet. Design and Construction

5.1 Magnetic fields used in the measurement of magnetostriction

The magnetostriction measurement techniques which have been described in the previous chapters can be effectively divided into two types. One type is that in which the magnetostriction constant is obtained from measurement of the crystal plane misorientation across a domain wall, and here no magnetic field needs to be used. The second type is that in which the constants are obtained by measuring macroscopic strain using a variety of methods, e.g. the strain gauge technique, the electrical capacitance technique, etc. In these latter measurement techniques, a magnetic field needs to be applied in various directions relative to the crystal axes of a single crystal.

In Table 5.1 a summary of the magnetic fields used in the measurement of the magnetostriction of some interesting magnetic materials is given.

When magnetostriction measurements are made, the magnetization is pulled wholly into the direction of the applied field. For the state of saturation to be reached in such a way, the applied magnetic field needs to overcome the demagnetizing field of the specimen and also its anisotropy field. The first of these problems is simplified to some extent through the choice of a specimen shape for which the demagnetizing factor has a suitably low value. The second problem however depends only on the size of the applied magnetic field versus the anisotropy field. As can be seen in the table, fairly moderate fields can be used to achieve the state of saturation in the transition elements cited and in the garnets. Somewhat higher fields have had to be used in the rare earth element measurements. The anisotropy fields in these latter materials are considerably higher.

Table 5.1

Material	Magnetic field	Author
Co	Up to 17k Oe	Alberts and Alberts (1963)
Fe	7k Oe	Lourens and Viljoen (1966)
Ni	5k Oe	Birss and Lee (1960))
	8k Oe	Benninger and Pavlovic (1967))
Dy	Up to 26k Oe	Legvold (1963)
Ho	Up to 26k Oe	Legvold (1963)
Tb	Up to 30k Oe	Rhyne and Legvold (1965)
Gd		Alstad and Legvold (1964)
Er	Up to 30k Oe	Rhyne and Legvold (1965)
$R_3Fe_5O_{12}$	Up to 14k Oe	Iida (1967)

(R = Sm, Eu, Gd, Tb, Dy, Ho, Er, Tm, Yb, Y)

5.2 Fields obtainable from different types of electromagnet

The magnetic field values used in laboratory experiments may be divided into four groups. The groups are:

(i) weak , < 1 Oe

(ii) moderate , 1 Oe → 20 kOe

(iii) strong , 20 kOe → 100 kOe

(iv) very strong , > 100 kOe

The production of weak magnetic fields is accomplished straightforwardly by the use of simple wire coils through which an electric current is passed. The main problem is that of screening the field produced from other unwanted components; for example the earth's magnetic field, and the stray fields from electric cables in the laboratory. In the lower part of the moderate field region, up to values of about 1 kOe, again fairly simple coil systems may be used. Higher electric currents are required and a larger number of turns is used. However, the power level is low enough so that air cooling suffices.

Depending on the experimental requirements; for example uniform magnetic field, uniform magnetic field gradient; different coil configurations are used to give the desired electric current distributions. Adequate details of these various magnetic fields and their production can be found in the book by Zijlstra (1967).

If the air core of a solenoid is filled with a high magnetic permeability material (iron, low carbon steel), the field from the solenoid may be used to magnetize the material. In this way a magnetic field can be produced in an air gap in the iron. Fields in the region 1-20 kOe can thus be produced. The magnetization of the iron reaches saturation at a fluse density of 21 k Gauss, and it becomes more difficult to produce magnetic fields beyond 20 kOe using soft iron electromagnets. A simple soft iron electromagnet arrangement is shown in Figure 5.1.

For the strong magnetic fields, beyond 20 kOe, arrangements which combine the field contribution from the soft iron with a field contribution from the electric solenoid may be used. A suitable arrangement, which shows an axial symmetry of the core and solenoid, is shown in Figure 5.2(a).For such an arrangement, a typical specification might be:

$H_{solenoid}$	:	84,000	Oe
H_{Fe}	:	36,000	Oe
H_{total}	:	120,000	Oe
Solenoid current	:	10^4	ampères

Magnetic fields in the strong region may also be produced by solenoids made of a superconducting material, for example NbTi, NbSn, NbZr. These operate at low temperatures, < 18^{o}k, and thus require cryogenic systems to be built around them.

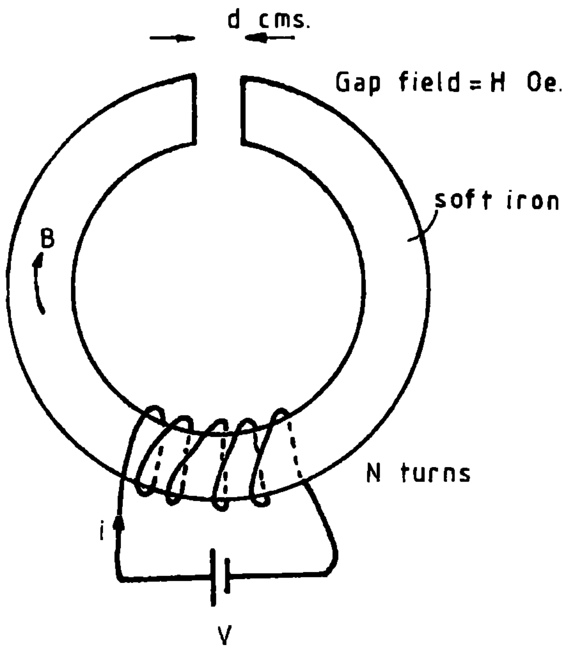

Fig.5.1 (a).

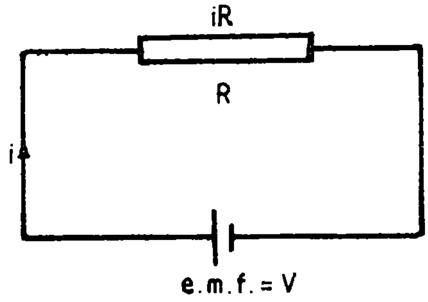

Fig.5.1 (b). Basic magnetic and electric circuits. The magnetomotive force is $0.4\pi Ni$, the air gap of the main load is d. The electromotive force is V and the main load is the resistance R.

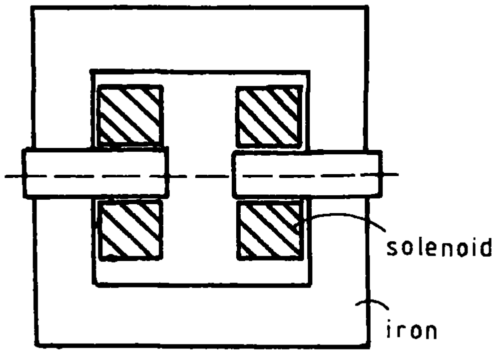

Fig.5.2(a). Cross section of electromagnet with cylindrical symmetry.

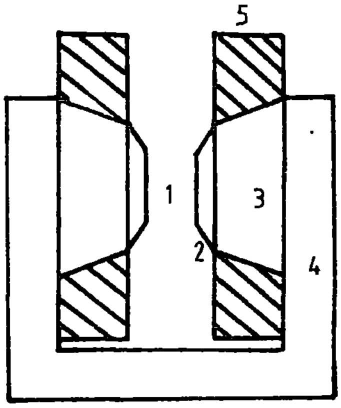

Fig.5.2(b).
Typical parts of electromagnet, 1, air gap, 2, pole pieces, 3, core, 4, yoke, 5, magnetizing solenoid.

As one goes into the region of very strong magnetic fields using a conventional electromagnet it can be seen that the contribution from the iron circuit becomes less and less important. The iron may be omitted from the system and high power solenoids used alone. The magnetic fields produced from these high power solenoids, and the technical problems associated with their production, have been discussed by Bitter (1939). High power water cooled magnets, with and without iron, have also been discussed by Bitter (1961).

Magnetic fields greater than 150 kOe are produced using a pulsed magnet. In this arrangement a large electrical charge is passed through a coil of low inductance. In the system used in Amsterdam, 9 megawatts are taken from the mains supply for 1 second. The field builds up to a maximum 400 kOe for about 0.1 second and then dies off over about 5 seconds.

The production of the strong and very strong magnetic fields generally takes place in laboratories which are built especially for this purpose because of the magnitude of the technical problems involved.

For the magnetostriction measurement described in this thesis, it was decided to construct a low carbon steel-core electromagnet, as this could provide an adequate field of at least 10 kOe over a suitable volume.

5.3 General description of magnetic fields and iron core electromagnets

5.3.1 The quantities used

The important quantities used in the description of the field of a magnet are the magnetic flux, flux density (induction), $\underset{\sim}{B}$, fieldstrength, $\underset{\sim}{H}$, and magnetomotive force. The flux and flux density are easily visualised as lines of force emerging from the magnet. The flux is then defined as the number of lines of force passing through a certain cross section and the flux density as the number of lines of force passing through unit area. To maintain a certain flux density over a given length, a magnetic potential is required, and the gradient of the magnetic potential is the field strength. The magnetic potential is generated by the magnetomotive force.

5.3.2 General equations

In vacuum, or in another non-magnetic material, $\underset{\sim}{B}$ is related to $\underset{\sim}{H}$ by the permeability, so that

$$\underset{\sim}{B} = \mu_o \underset{\sim}{H} \qquad (5.1)$$

In the S.I. system of units, μ_o is equal to $4\pi \times 10^{-7}$ henry/metre. For magnetostatic fields it is more convenient to put μ_o equal to 1 and dimensionless. There is then no difference in magnitude and dimension of $\underset{\sim}{B}$ and $\underset{\sim}{H}$ and both may be measured in the same unit, the gauss. Thus for magnetic fields in non-magnetic materials the flux density and fieldstrength have not only the same dimension but also the same numerical value, and this leads to the use of field strength, where flux density is intended. In non-magnetic materials though, this does not lead to any confusion. The unit oersted for field strength distinguishes the magnetomotive force per cm from the flux density. The distinction is useful in magnetized matter, where, because of the presence of magnetic dipoles, less magnetomotive force is required to maintain a given flux density. The following relation between $\underset{\sim}{B}$ and $\underset{\sim}{H}$ can be written:

$$\underset{\sim}{B} = \underset{\sim}{H} + 4\pi \underset{\sim}{M}\underset{\sim}{\alpha} \qquad (5.2)$$

where $\underset{\sim}{M}$ is the magnetic moment per cubic cm of the material and α is a factor depending on the geometry of the medium. In an infinitely long bar, the value of α is 1, then

$$\underset{\sim}{B} = \underset{\sim}{H} + 4\pi \underset{\sim}{M} = \mu \underset{\sim}{H} \qquad (5.3)$$

where μ is the permeability of the material. For iron, μ is very large, so hardly any magnetomotive force is needed to cause a magnetic flux to pass through the material. Magnetostatic fields can be described by Maxwell's equations written in the following form

$$\underset{\sim}{\nabla} . \underset{\sim}{B} = 0 \qquad (5.4)$$

$$\underset{\sim}{\nabla}_{\wedge} \underset{\sim}{H} = 0.4\pi n i$$

where $\underset{\sim}{B}$ and $\underset{\sim}{H}$ are in gauss and oersteds, and η is the number of current loops per square cm and i is the current contributing to the field. The first equation states that the flux entering a certain volume and the flux leaving it are equal. The second equation gives the relation between the current loops and the magnetomotive force present in the system. It can be rewritten via Stokes' law as

$$\oint \underset{\sim}{H} . d\underset{\sim}{\ell} = 0.4\pi \ Ni \qquad (5.6)$$

This means that the magnetomotive force acting in a certain closed path is equal to 0.4π times the total number of ampère turns, Ni encircled by the path.

5.3.3 The magnetic circuit

The two equations are illustrated by a magnetic circuit. This model shows a resemblance to an electrical circuit consisting of a resistance and a battery, as is shown in Figure 5.1(a) and (b). The coil in the magnetic circuit is equivalent to the battery in the electric circuit. It has Ni_o ampère turns, which generate a magnetomotive force (m.m.f.) of $0.4\pi \ Ni_o$. The high permeability iron around which the coil is wrapped is equivalent to the electrical leads connecting the battery and the resistance. The iron has a low magnetic resistance, and the air gap is where the main part of the magnetic resistance is located. Thus the m.m.f. $0.4\pi \ Ni_o$ sends a flux density B across the gap of width d. The magnetic potential over the gap is $H_g d$, and if the rest of the material provides no magnetic resistance i.e. $\mu = \infty$, then $H_g d = 0.4\pi \ Ni$. This means that the fieldstrength, H_ℓ is actually written as

$$\underset{\sim}{H}_\ell = \underset{\sim}{B} - 4\pi \ \underset{\sim}{M} \qquad (5.7)$$

In most ferromagnetic materials $4\pi \hat{=} \underset{\sim}{M} \hat{=} \underset{\sim}{B}$, so provided $\underset{\sim}{B}$ is low, $\underset{\sim}{H}_\ell$ is very small. For increasing $\underset{\sim}{B}$ however, $4\pi\underset{\sim}{M}$ approaches a maximum value $4\pi \ \underset{\sim}{M}_o$ which is a constant of the material. If $\underset{\sim}{B}$ exceeds $4\pi \ \underset{\sim}{M}_o$, $\underset{\sim}{H}_\ell$ increases rapidly and the material is said to be saturated. For soft iron $4\pi \ \underset{\sim}{M}_o \hat{=} 21400$ gauss, and so saturation effects are observed for flux densities approaching this value.

5.3.4 The demagnetizing field and the stray field

The action of $\underset{\sim}{B}$ on the magnetic dipoles in the magnetic material is to align them in the direction of $\underset{\sim}{B}$. Inside the material, the north poles of one set of dipoles are compensated by the south poles of the next dipoles, so no magnetic "charges" are present. At the air gap, as is shown in Figure 5.3, no compensating poles are present, and so there are magnetic surface charges on the faces open to the air gap. The flux density in the air gap can be thought to result from the action of these surface charges, and can be calculated for different geometries of the gap. The surface charges also produce a field in the flux conducting bars. This field is opposite to that originally present and so is referred to as the demagnetizing field. The demagnetizing field is stronger if the gap is larger. The result of the appearance of the demagnetizing field is that the flux density near the air gap face is lower than at a point more remote from the gap. The equation $\underset{\sim}{\nabla}.\underset{\sim}{B} = 0$, however, requires that the total flux passing through any plane is constant. As the flux density inside the material decreases nearer the gap, the area in which the flux flows must increase. Thus the surface charges "push", with their demagnetizing field, the lines of force outside the magnetic circuit. This part of the flux that crosses the air gap midplane outside the air gap is called the stray flux.

If the flux density in the material is known, then calculation of the gap field amounts to calculating in the first place the stray flux.

The stray flux can also be described by using the magnetic potential of the circuit. In Figure 5.4 the two ends of the circuit have an opposite magnetic potential $\pm V$, where the gap field $H_g = {}^{V}/d$. A closed loop is formed, indicated by the dotted line, and the potential gained or lost in this loop is integrated, $\int Hdx$; this value must be zero since there are no ampere turns in the loop. Hence

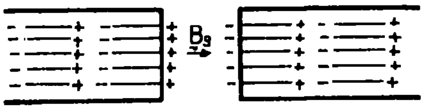

Fig.5.3. Inside a magnetized medium the + and - poles of the magnetic dipoles compensate each other. The uncompensated poles appear on the surface and generate a flux density B_g in the air gap.

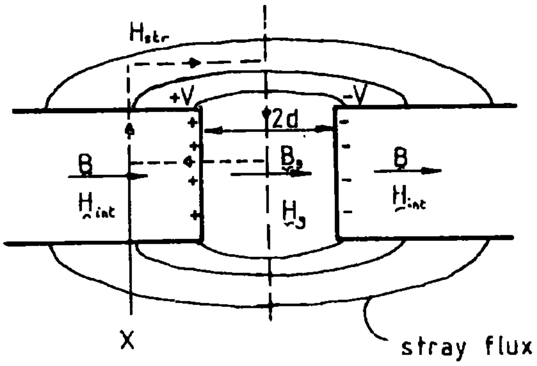

Fig.5.4 Stray flux of a magnetized pair of poles. The potential at the face of the air gap ±V gives rise to a flux density in the gap, B_g, the field strengths of the gap field and the stray field are H_{int} and H_{str} respectively.

$$\int H_{stray}\,dx + H_g d + \int H_{int}\,dx = 0 \qquad (5.8)$$

Even if the internal field, $\underset{\sim}{H}_{int}$, were neglected, there would nevertheless be a stray field, and only a fraction of the flux passing through the bar would appear in the air gap.

5.3.5 Units

A diagram showing the essential parts of an electromagnet is given in Figure 5.2b.

In the design of magnets and magnetic fields, the units used in the formula tend to be mixed, on the grounds of convenience, for example, the Fabry formula (Bitter, 1961) gives the field due to a solenoid

$$H = G \left[\frac{W\lambda}{\rho a}\right]^{\frac{1}{2}} \qquad (5.9)$$

G is a geometry factor, W is the power in megawatts, λ is a space factor, ρ is in ohm cms, a is in cms and H is in kilogauss.

In the calculations which will follow, the units used will be oersteds for fieldstrength, gauss for flux density, cms for distance and ampere turns for magnetomotive force. However, in Table 5.2 a comparison is shown for convenience of some units in the Gaussian and S.I. or mks A system.

5.4 The equations used for the design of electromagnets

5.4.1 Some sources of reference

The three important references used in the design of the electromagnet described in this thesis are the works by Montgomery (1961), Zijlstra (1967) and Kroon (1968). Montgomery's work describes the calculation of the gap fields by means of equivalent surface poles or surface charges. The calculations are given for a variety of iron pole piece geometries. He reiterates the calculations, by considering distributed volume dipoles.

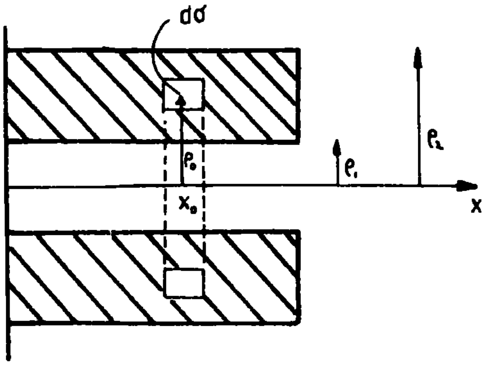

Fig.5.5 Thick solenoid with winding element.

Table 5.2

Comparison of unit systems

Gauss		mksa
$Oe = 10^3\ A.m.^{-1}$ ...	magnetic field strength...	Amp/ metre
$Gauss = 10^4\ V.s.m.^{-2}$...	magnetic induction ...	Volt second/metre^2

Finally he analyzes a number of existing magnets, and gives a method by which the performance of a magnet might be predicted. The method is based on the measured properties of the particular magnets analyzed.

Kroon's book describes the calculations of the gap field. He also presents a method for calculating the stray flux and thus the total ampère turn requirement, and generally he gives a comprehensive account of the basic information required for the design of a laboratory electromagnet.

Zijlstra gives a more mathematical treatment of the magnetic potential, potential gradient, field gradient etc. He also gives a detailed calculation of the field of an air core solenoid. The equations for an air core solenoid are taken from Zijlstra's book. The equations for the gap field of the iron pole pieces are taken from Montgomery and Kroon, whilst the equations for the stray flux are taken from Kroon. A description of the magnet performance prediction by Montgomery is also given. In any case, the material from the three works overlaps to some extent.

5.4.2 Equations for an air core solenoid

A cylindrical core of rectangular cross section is considered as shown in Figure 5.5. The density of turns is considered to be the same at every point, and to each point a current density is attributed, which is also uniform throughout the cross section. The field H_x is required at a point on the x axis, which is taken as the origin. The magnetic potential at the origin may be written

$$V = \sum_{\ell=o}^{\infty} a_\ell \, x^\ell \qquad (5.10)$$

The contribution da to the coefficient a, caused by the circular current $\tau d\cdot\sigma$ flowing through the element $d\sigma$ is then

$$da_1 = \frac{-1}{2} \frac{\rho^2 \, d\rho \, dx_o}{(x_o^2 + \rho^2)^{3/2}} \qquad (5.11)$$

ρ is the distance of $d\sigma$ from the x axis and x_o is its x coordinate. da_1 is integrated for the coil with inner radius ρ_1 and outer radius ρ_2 (= $\alpha\rho_1$) and extending axially from $X_o = 0$ to $X_o = \beta\rho_1$. Then from

$$\left[\frac{\partial^{\ell-1} H_x}{\partial x^{\ell-1}}\right]_{x=o} = \ell !\, a_\ell \qquad \left[\frac{\partial^{\ell-1} H_x}{\partial x^{\ell-1}}\right]_{x=o} = \ell !\, a_\ell \tag{5.12}$$

the fieldstrength is given by

$$H_x\,(0) = \frac{\tau}{2}\,\rho_1\beta\,\ell n\,\frac{(\alpha + (\alpha^2 + \beta^2)^{\frac{1}{2}})}{1 + (1 + \beta^2)^{\frac{1}{2}}}$$

$$= \tau\,\rho_1\,F_1 \tag{5.13}$$

where F_1 is then a geometrical constant.

5.4.3 Equations for the gap field from the iron pole pieces

It is sometimes said that the tapered pole piece causes the flux to "converge" on the air gap. However the field in the pole is usually parallel to the axis, so that no convergence exists. Also, the part of the flux appearing in the air gap is, as a rule, a small fraction of the total flux in the yoke. Thus there is certainly no "lens focussing" action, but some concentration of flux density occurs. Only the geometry of the pole and the properties of the magnetized medium determine the field in the gap.

The surface charge density on the pole is assumed to be constant, which means that the magnetization of the pole is constant. As the flux density in the pole does vary, this assumption will be valid only for completely saturated poles.

The field between two uniformly and axially magnetized rods is considered, as shown in Figure 5.6(a). If σ is the magnetization per unit volume, it is also the uniform charge per unit area. If the area dA is measured normal to the direction of magnetization, then the field arising from any infinitely long pair of cylindrical rings of radius r and section dr is

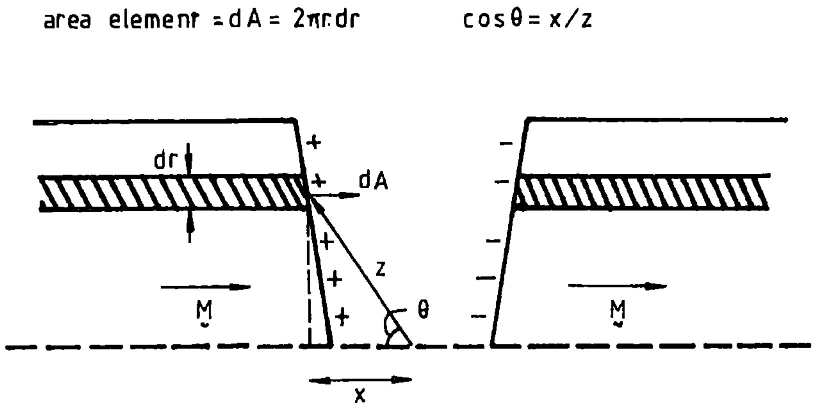

Fig.5.6(a) Arrangement for calculation of gap field from consideration of surface magnetic charge distribution.

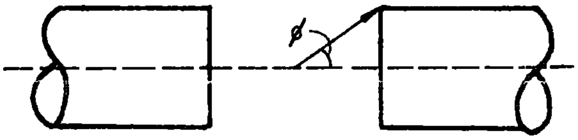

Fig.5.6(b) Cylindrical flat poles.

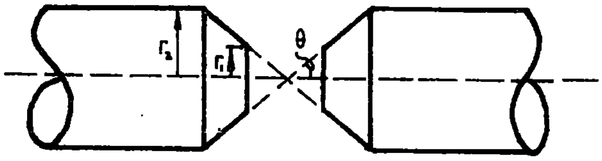

Fig.5.6(c) Tapered poles with coinciding apices.

$$dH = 2k\sigma \; \frac{2\pi \; rdr}{r^2} \sin^2 \Theta \cos \Theta \qquad (5.14)$$

This is integrated over several different pole geometries. For cylindrical flat poles, see Figure 5.6(b), the field is

$$H = 4\pi \; k \; \sigma \; x \int_o^{r_1} \frac{r \; dr}{(x^2+r^2)^{3/2}}$$

$$= 4\pi \; k \; \sigma \quad (1 - \cos \Theta) \qquad (5.15)$$

For poles with coinciding apexes, see Figure 5.6(c), the field is

$$H = 4\pi \; k \; \sigma \; \left[1 - \cos \Theta + \int_{r_1}^{r_2} \frac{r \cot \Theta \; r \; dr}{r^3 (\cot^2 \Theta + 1)} \right]$$

$$H = 4\pi \; k \; \sigma \; \left(1 - \cos \Theta + \cos \Theta \sin^2 \Theta \ell n \; \frac{r_2}{r_1} \right) \qquad (5.16)$$

The first two terms, $4\pi \; k \; \sigma \; (1 - \cos \Theta)$, represent the contribution of the flat face, and the last term $4\pi \; k \; \sigma \; (\cos\Theta \sin^2\Theta \; \ell n \; \frac{r_2}{r_1})$ represents the contribution of the conical surface.

These represent the interesting cases of relevance for the work discussed in this thesis. Other geometries may also be discussed. $4\pi \; k \; \sigma$ represents the maximum saturation flux density, which is 21400 gauss for iron. Thus for flat pole pieces, the limiting field is 21400 Oe, which is reached at $\Theta = 90^o$, i.e. the gap is then zero. For conical pole pieces however, this limiting value can be exceeded by suitable choice of r_2 and r_1 and Θ.

5.4.4 Equations for the stray field

The ampère turns, Ni, present in the magnetizing solenoid, provide a magnetomotive force, 0.4π Ni. Some of this drops over the "leads" of the magnetic circuit, and the remainder in the air gap. The total number of ampère turns consumed depends on the geometry of the circuit, the magnetic properties of the material and on the flux density in the air gap. To estimate the magnetomotive force, the magnet is split into the gap and the iron path.

As was mentioned in section 5.3, the main difficulty in the design of electromagnets is the calculation of the integral $\int (H_{stray} + H_i)dx$, which represents the magnetic potential required for the entire magnetic circuit except the air gap. It should be possible to calculate exactly the quantities such as flux density, stray flux, magnetic potential, and so on, as they form part of rather simple differential equations. The boundary conditions for the general case of tapered poles, and the non linear relation between the magnetic fieldstrength, $\underset{\sim}{H}_i$, and the flux density $\underset{\sim}{B}$, provide complications which make it necessary to use somewhat rough approximations. The first approximation is that the field strength $\underset{\sim}{H}_g$ in the gap is perfectly homogeneous (and thus also the flux density $\underset{\sim}{B}_g$). Thus the magnetic potential across the gap can be written $V_g = 2H_g . d$.

The second approximation is described as follows. In the material of the poles and cores, the flux density and fieldstrength are assumed to be parallel to the core axis, and both quantities are assumed to depend only on the axial x coordinate. The flux density is assumed to be homogeneous in the radial direction.

The third approximation can be seen after considering Figure 5.7(a) and (b). In (a) the lines of force are shown for a pair of poles. On the conical surface the lines of force of the stray flux are perpendicular to the conical surface, resulting from the boundary conditions for the field strength. In Figure 5.7(b) a contour is described by the dotted line, over which there is no potential increase or decrease because no current windings pass through the loop. As a result of the first two approximations, the potential at the conical surface at x + d from the air gap mid plane is

$$V(x) = H_g d + \int_0^x H_i \, dx \qquad (5.17)$$

Following the path further, it can be seen that

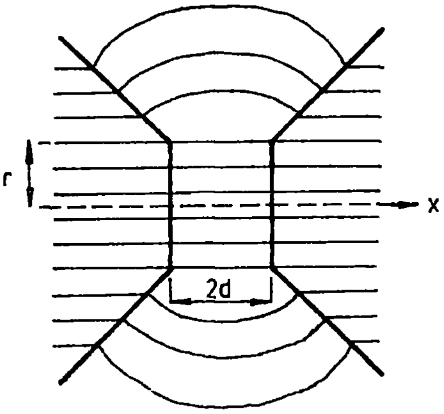

Fig. 5.7(a) For the calculation of the stray flux it is assumed that the lines of force inside the poles are parallel to the axis, at the boundary between pole and air the flux is perpendicular to the surface.

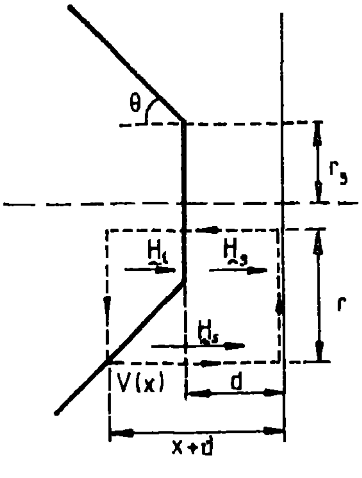

Fig. 5.7(b) Magnet pole having a face-radius r_s, taper θ, and half air gap d. The pole is assumed to be magnetized parallel to the x-axis. The dotted rectangle represents a contour described to find the magnetic potential V(x) of the pole and the stray field $\underset{\sim}{H}_s$.

$$V(x) = \int_{o}^{x+d} H_s dx \tag{5.18}$$

where H_s is the stray field. Eliminate $V(x)$ to obtain

$$\int_{o}^{x+d} H_s dx = H_g d + \int_{o}^{x} H_i dx \tag{5.19}$$

The third approximation is then that

$$\int_{o}^{x+d} H_s dx = H_s (x+d) \tag{5.20}$$

This means that the stray field strength at a certain distance from the axis is constant in the axial direction.

The latter two assumptions are justified on the grounds that it is the average value of the field that counts and not the exact distribution.

The three assumptions in summary are: that the magnetization is parallel, that there is no radial dependence, and that $H_s = V(x)/(x+d)$.

A pole, as shown in Figure 5.8, is considered. The taper of the pole is Θ, so $r = r_g + kx$, where $k = \tan\Theta$. According to the assumption made, the stray field flux density is written

$$B_s = \frac{1}{(x+d)} \left[B_g d + \int_{o}^{x} H_i dx \right] \tag{5.21}$$

As the flux leaves the pole normal to the surface, the stray flux $d\phi_s$ leaving aside the pole between x and x+dx is taken as the product of B_s and the surface of revolution between x and x+dx, that is,

$$\phi_s = 2\pi \left[k^2+1\right]^{\frac{1}{2}} \int_{o}^{x} dx \, \frac{r_g+kx}{x+d} \left[B_g d + \int_{o}^{x} H_i dx \right] \tag{5.23}$$

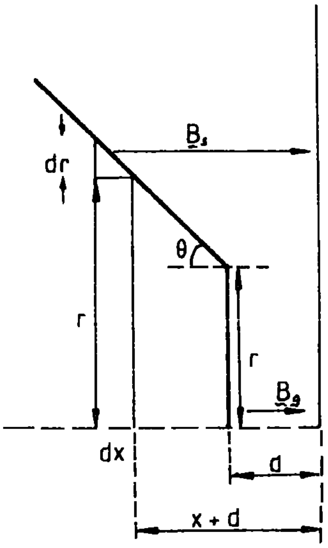

Fig.5.8 Geometry of a magnet pole used for stray flux calculation. The flux density in the gap is $\underset{\sim}{B}_g$. The flux density of the stray field at the pole between (x + d) and (x+d) + dx is $\underset{\sim}{B}_s$.

and the total flux passing through the pole is

$$\phi_t = \pi\, r_g^2\, B_g + \phi_s$$

$$= B_{pole}\, \pi\, (r_g + kx)^2 \qquad (5.24)$$

where B_{pole} denotes the flux density in the pole. For low and medium gap fields where the pole is not at saturation the term $\int_o^x H_i dx$ can be neglected.

If the drop in magnetomotive force in the pole can be neglected, the flux density in the pole can be calculated directly. The integral for the stray flux becomes simple and the stray flux is written:

$$\phi_s = 2\pi\; B_g\, d\, \left[\, k^2+1\, \right]^{\frac{1}{2}}\; \left[\, kx+(r_g-kd)\; \ell n\; \frac{x+d}{d}\, \right] \qquad (5.25)$$

For x/d and r_g/d substitute E and ρ_g respectively so then

$$\phi_s = B_g\; \pi r_g^2\;\; 2\left[\, k^2+1\, \right]^{\frac{1}{2}}\; \left[\, kE\; +\; (\rho_g - k)\ell n(E+1)\, \right]/\rho_g^2$$

$$= B_g\; \pi r_g^2\; S(E) \qquad (5.26)$$

where S(E) is the stray function which can be calculated for various values of the taper angle.

At the end of the pole the flux enters the core. The stray flux extending from the core can be calculated from

$$\phi_{s\ core} = B_g\; \pi\; r_o^2\;\; S'\;\; \frac{d}{d'} \qquad (5.27)$$

where S' is the stray function of a pole with zero tapering. The values of ρ_g' and d' will be explained more fully later when the actual calculation with this equation is described.

The total flux passing through the core is found to be

$$\phi_{t\ core} = \phi_g + \phi_{s\ pole} + \phi_{s\ core} \qquad (5.28)$$

To obtain the required number of ampère turns per solenoid, or the magnetomotive force to operate the magnet, the relation

$$Ni = \frac{Hd}{0.4\pi} \qquad (5.29)$$

is used where 2d is the gap in cms, H is the fieldstrength, N is the number of turns in the solenoid, and i is the current in ampères.

To prevent loss of ampère turns over the yoke the flux density in the yoke has to remain far from the saturation value. If the yoke is made of cast steel the acceptable value for the flux density is 15000 Gauss.

5.4.5 Montgomery's comparison

Montgomery considered a variety of magnets with tapered pole tips by way of comparison. The maximum fields for some thirty six magnets at a variety of pole diameters, pole tips and gaps were predicted from the equations derived on the basis of the model of homogeneous surface charges. The actual fields lay between 90% and 120% of predicted fields for all magnets. 85% of the magnets were able to be predicted within ± 4% by use of an empirical factor $F(r_1, r_2, \ell_g, \beta_c)$. This is written

$$F(r_1, r_2, \ell_g, \beta_c) = 2 + \log_{10} \left[\frac{2r_i}{\ell_g} \right] - \frac{r_1}{r_2} - \beta_c \qquad (5.30)$$

The remaining 15% are magnets where β_c is small and the yoke contribution is high and the actual fields are higher than predicted by about 20%.

The parameters on which the F factor depends are shown in the pole piece diagram in Figure 5.9. In this figure the ratio of the measured iron field to the predicted iron field is plotted as a function of F. For the magnets considered by Montgomery the representative points lay in the areas indicated and the figure may be used to predict whether a particular magnet design will produce a maximum field less than or greater than that actually calculated. The figure shows that magnets with a large gap, and/or r_2/r_1 approaching 1, and/or a long core, tend to produce less field than predicted and magnets with a small gap, large r_2/r_1 and short cores, produce greater fields. The poor results at wide gaps arise from two sources. The first is that saturation takes place in the core near the yoke. The second is that

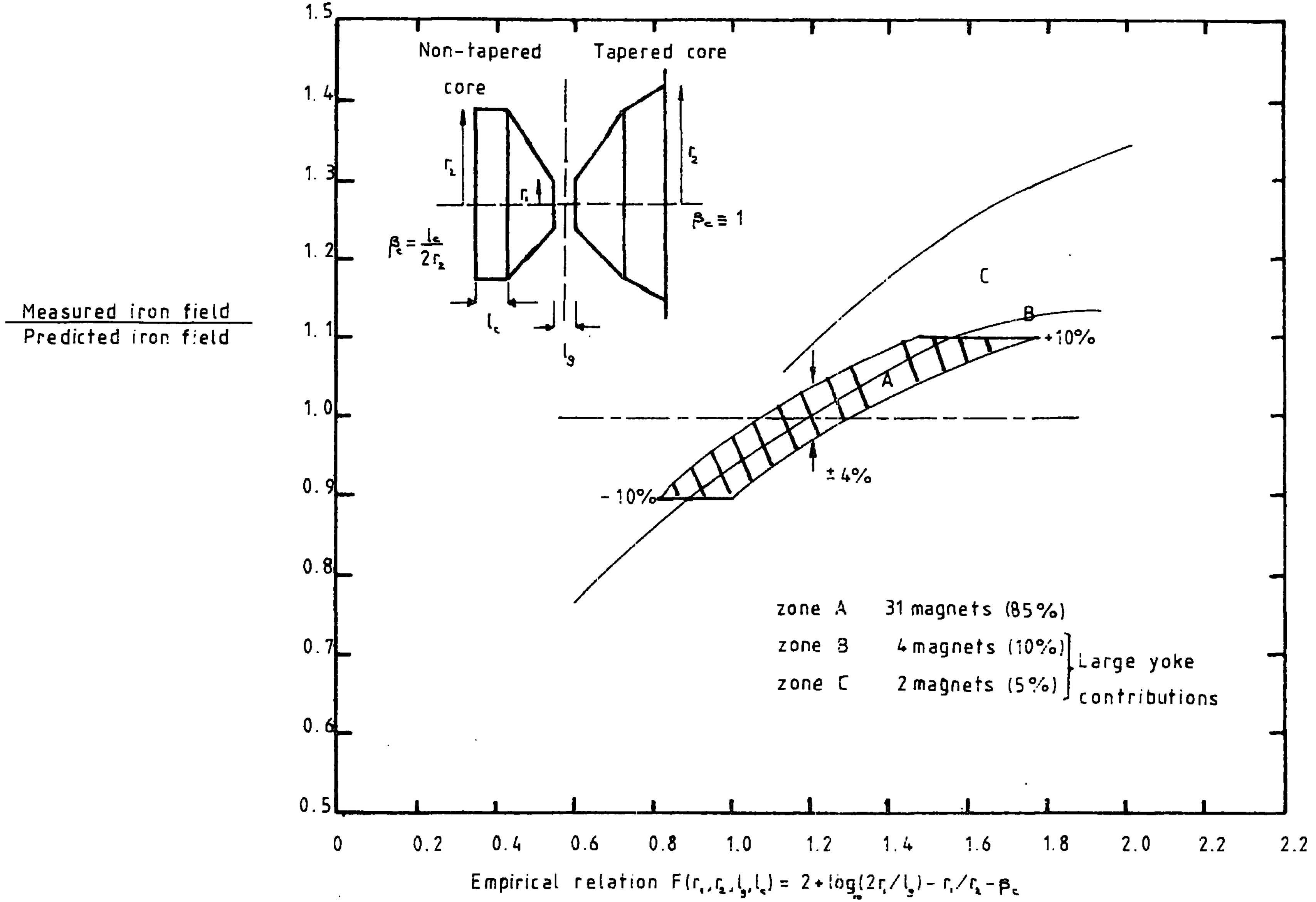

Fig.5.9 Prediction results for 36 tapered pole magnets. Montgomery (1961).

the magnetization may not be parallel to the axis at the pole edges, which reduces the gap field. Magnets having short cores (ℓ_c/r_1 small) show a better performance due to the fact that magnetization of the yoke will contribute also to the gap field.

It is difficult to compare magnets as there exists no universal criterion, and as will be seen, the magnet design arrived at in this thesis has its own peculiarities and the magnet shows considerable differences at least from the others in the laboratory here.

5.5 Geometrical and experimental requirements of the magnet

Four basic requirements of the magnet were known at the outset. These requirements were used as original design criteria. They may be given as follows.

(a) Magnitude of Gap Field

It can be seen from Table 5.1 that some magnetostriction work can be done using magnetic fields of up to 10k Oe. Fields of up to 15k Oe would make measurements on Rare earth garnets possible. It has already been stated that the saturation flux density of iron is 21.4 kilo Gauss. To produce gap fields greater than 21k Oe, a contribution to the field would be required from the solenoid, or a pole piece geometry where r_2/r_1 is high and the taper angle is large would be needed. It will be pointed out in more detail in section 5.6 that neither of these situations may be allowed. The figure decided on then is a minimum field of 10k Oe.

(b) Pole piece gap

It was decided that a pole piece gap of 4cms be used. This would give sufficient room for low temperature apparatus, or the goniometer system required, to be easily inserted, beside the fact that a reasonable amount of space is required for the X ray beam entering and leaving the specimen area.

(c) Taper angle of pole pieces

From the equation $\frac{\Delta d}{d} = \frac{-\Delta\Theta}{\tan\Theta}$ (see Chapters 3, 4) it is seen that the sensitivity of the double crystal camera increases as Θ approaches 90°.

A taper half angle of 42° would enable a Bragg angle of slightly more than 87° to be used, if needed, whilst in the meantime the field may be rotated through 90° without the pole pieces getting in the path of the X ray beam. This is illustrated in Figure 5.10. If the field does not need to be rotated, much lower Bragg angles may be used when lower order Bragg reflections are required. The specimen needs to be at the centre of the gap volume, and so that the tips of the pole pieces do not block the path of the beam, a taper half angle of 42° was decided on, and the apices of the pole piece need to be coincident.

(d) Rotation of magnetic field

Benninger and Pavlovic (1967) measured the magnetostriction of Ni by taking data points at 10° intervals of the angular setting of the magnet over a total of 90°. The method was formulated by Bozorth and Hamming (1953). If the method of measurement being described in this thesis were extended to cover Bozorth and Hamming's technique, it is clear that the field would need to be rotated. Since different Bragg angles are used in individual experiments, the angular setting of the magnet would need to be changed in any case.

5.6.1 Iron circuit

A gap of 4cms together with a taper ½ angle 42° leads to the pole piece geometry shown in Figure 5.11. From the equation

$$H = 4\pi M_o \left(1 - \cos\Theta + \cos\Theta \sin^2\Theta \ \ell n \frac{r_2}{r_1}\right) \qquad (5.31)$$

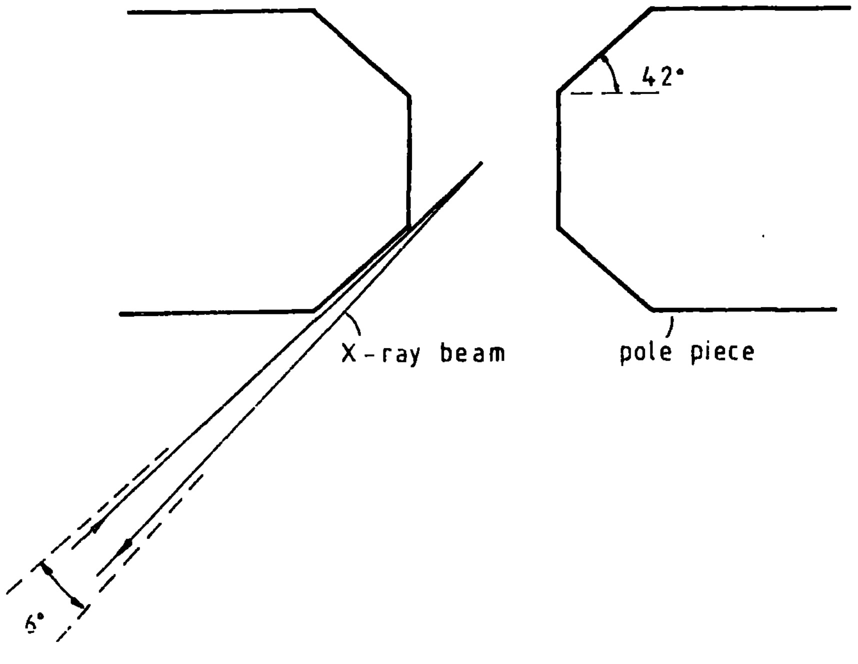

Fig. 5.10 Schematic diagram of geometrical arrangement of magnet pole pieces and X-ray beam if high Bragg angles are used and magnet needs to be rotated through 90°.

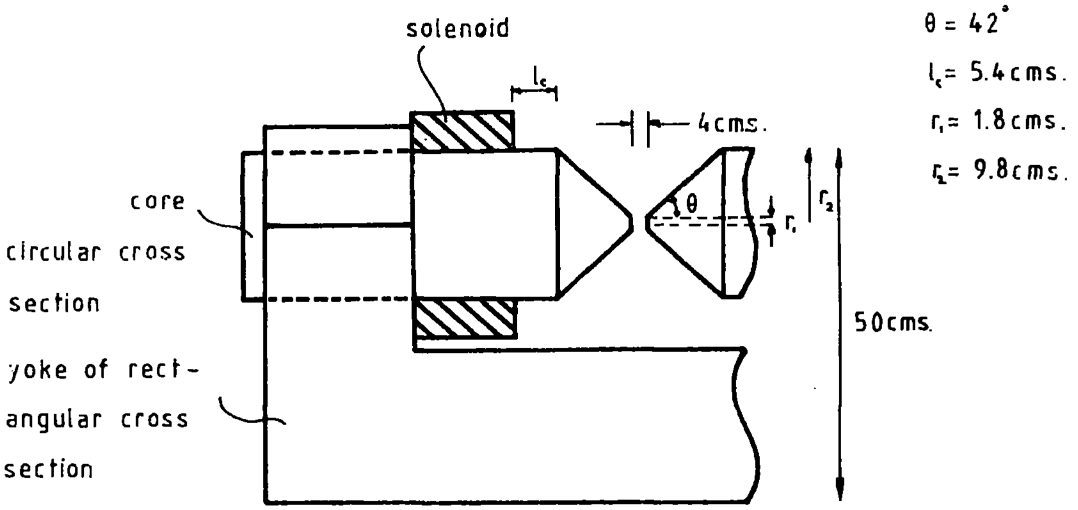

Fig.5.11 Schematic diagram showing front view of half section of original magnet design, and cross section of space available for solenoid.

it can be seen that for a gap field of 10k Oe, the value of the magnetization M_o is about 12 kilo Gauss. As 10k Oe is a minimum figure being aimed at, a value of about 15k Gauss would be better. This would be in accordance with the value mentioned previously on which the stray flux equations are based.

The value of ℓ_t in Figure 5.11 is decided on by considering Montgomery's empirical prediction factor.

$$F = 2 + \log_{10} \left[\frac{2r_1}{\ell_g}\right] - \frac{r_1}{r_2} - \beta_c \qquad (5.32)$$

Using a value of ℓ_t about 5.5cms, it can be seen that the value of F is 1.49. From Figure 5.9 it can be seen that the ratio $\frac{\text{measured iron field}}{\text{predicted iron field}}$ is between 1.0 and 1.1. To provide suitable "leads" in the magnetic circuit, it was decided to have a yoke of rectangular cross section (20cms x 26cms) as indicated in Figure 5.11.

If the magnetic field required to produce a flux density of about 12 kilo Gauss in soft iron is calculated from the expression for the field of an air core solenoid, it is seen that only a few Oersteds are required, and the current required is less than 1 ampère. However when the air gap provides the "resistance" in the magnetic circuit, the current requirement increases for the same solenoid as is now shown by the stray field calculations.

5.6.2 Stray flux and ampère turn requirement

(i) Gap flux

The gap flux is

$$\Phi_{gap} = \pi r_1^2 B_g \qquad (5.33)$$

$$= 101828 \text{ Gauss cm}^2 \text{ if } B_g \simeq 10 \text{ kilo Gauss}$$

(ii) Cone stray flux

The cone stray flux is

$$\Phi_{s_{cone}} = \pi r_1^2 B_g \, 2 \left[k^2+1 \right]^{\frac{1}{2}} \frac{\left[kE+(\rho_g-k)\ell\eta(E+1) \right]}{\rho_g^2} \qquad (5.34)$$

$$= 1384860 \text{ Gauss cm}^2$$

(iii) Core stray flux

The core stray flux is

$$\Phi_{s_{core}} = \pi r_o^2 \, S'(E') \, \frac{d}{d'} \qquad , \; k = 0 \qquad (5.35)$$

$S'(E')$ is the stray function for a taper angle of zero. d' is the length of the core between the conical section and the solenoid.

The values of the parameters used in calculations are summarized in Table 5.3.

In order to estimate the total ampère turn requirement per solenoid, the total flux can be treated in two ways. The flux from the core, cone and gap can be divided by the respective area of each component to give an average flux density.

For the core, the average flux density is 1486 Gauss. The average distance (D) over which this is taken per solenoid is 13.8cms. From

Ampère turns = Ni = HD/0.4π

16300 ampere turns are required.

For the cone, the average flux density is 3044 Gauss. This is taken over an average gap of 6.5cms, and 15858 ampère turns are required.

For the gap, the flux density is 10 kilo Gauss. This is taken over 2cms, and 15909 ampère turns are required. The total ampère turn requirement is then about 48000 ampère turns.

If the total flux requirement is considered to be taken over the cross section of the core, then an average flux density of 6500 Gauss is obtained. This is considered to be taken over a distance per solenoid of 16.5cms. This leads to an ampère turn requirement of about 85000 ampère turns. The actual value required should probably be taken somewhere between the two values at about 65000 ampère turns.

Table 5.3

taper = θ = 42^o

r_1 = 1.8cms

r_2 = 9.8cms

2d = ℓ_g = 4cms

β_c = $^{\ell c}/2r_1$ = 1.5

tan θ = k = 0.9

E = x/d = 4.5(5)

ρ_g = r/d = 0.9

S(E) = 13.6

d' = 11.1cms

E' = x'/d' = 0.5

$S'(E')$ = 0.9

x = 9.1cm

x' = ℓc = 5.4cm

5.6.3 Solenoid

In considering the iron circuit in Figure 5.11, it can be seen that the cross sectional area available for the solenoid is 4cms x 12.5cms = 50 square cms. It was decided to make the solenoids from soft copper tape. The tape would be wound into pancakes and the pancakes connected together to produce the final solenoids.

At this stage, the design depends on what standard sizes were available for the cross section of the copper tape. The three standard sizes which were considered to be most suitable were

(A) 0.64cm x 0.16cm
(B) 0.64cm x 0.24cm
(C) 0.95cm x 0.16cm

The length of each solenoid using the different tapes was estimated. Allowing 0.15cm between each winding and 0.15cm between each pancake for spacing, and for passing cooling fluid through the solenoid, the number of turns possible for each solenoid was estimated. Thus from the ampère turn requirement given above, the current was found. Using the resistivity of copper as 1.7×10^{-6} ohm cm, the power dissipation also was found. A summary of these calculations applied to each cross section of strip is given in Table 5.4.

From these calculations, it is seen that the power levels are prohibitively high.

Even if a thinner strip, say of 0.1cm x 0.1cm cross section was used, so that the number of turns is 5000 and the current requirement is about 15 amps, the resistance goes up to about 64 ohms. Thus the power level is still at least 9000 watts per solenoid.

Also, to produce an iron circuit as described, the cost for casting and machining is becoming prohibitive. If more room is allocated for the solenoid, or if r_2/r_1 is increased, this problem will be aggravated.

Table 5.4

	Solenoid (A)	(B)	(C)
cross section of conductor	0.64cm x 0.16cm	0.64cm x 0.24cm	0.95cm x 0.16cm
possible no. of turns per solenoid	204	163	147
current	318 amps	398 amps	440 amps
resistance	0.32 ohms	0.16 ohms	0.15 ohms
power dissipation	30 kwatts	25 kwatts	29 kwatts

5.7 Final design

5.7.1 Basic idea

From the problems mentioned, it can be seen that some way of maintaining the pole piece geometry needed to be found whilst sufficient space could be allocated for the ampère turn requirement without the path of the X ray beam being blocked, or the dimensions of the iron circuit becoming too large.

It was decided to consider having the solenoids placed below the pole pieces, with their axes vertical instead of horizontal as in the original design. Such an arrangement is shown in Figure 5.12(a). As can be seen, a cross sectional area of 12cms x 26cms = 312cms^2 can be used for the solenoid. If the copper strip of cross section 0.95 x 0.16cm^2 is used, and an allowance of 0.15cms is given between windings and pancakes, it is seen that about 900 turns per solenoid can be obtained. The ampère turn requirements for the gap and the cone will be the same as those for the original design.

5.7.2 Stray flux and total ampère turns requirement

The stray flux from the curved parts of the pole pieces, corresponding to $\Phi_{s_{core}}$, will not be so easy to calculate even on the assumptions made in the stray flux equations. On the basis that the area of the curved surface would be near one quarter of the surface area of a sphere of radius 20cms, i.e. about 1250cms^2, and the surface area of the core originally used is about 330cms^2, the stray flux function is taken to be about four times that used in the original calculation. The total stray flux for this part of the pole piece is then

$$\Phi_{s_{core}} = 1978840 \text{ Gauss cms}^2$$

This leads to an average flux density of 1650 Gauss which if taken over an average distance of 26.5cms leads to an ampère turn requirement of about 35000 ampère turns.

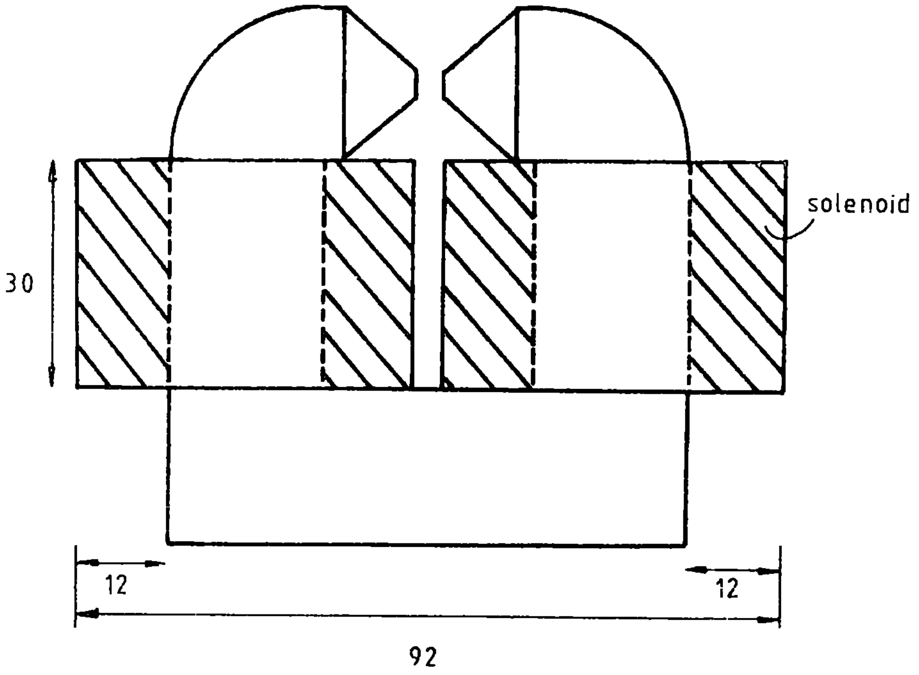

Fig 5.12(a) Final magnet design, schematic cross section. Dimensions in cms.

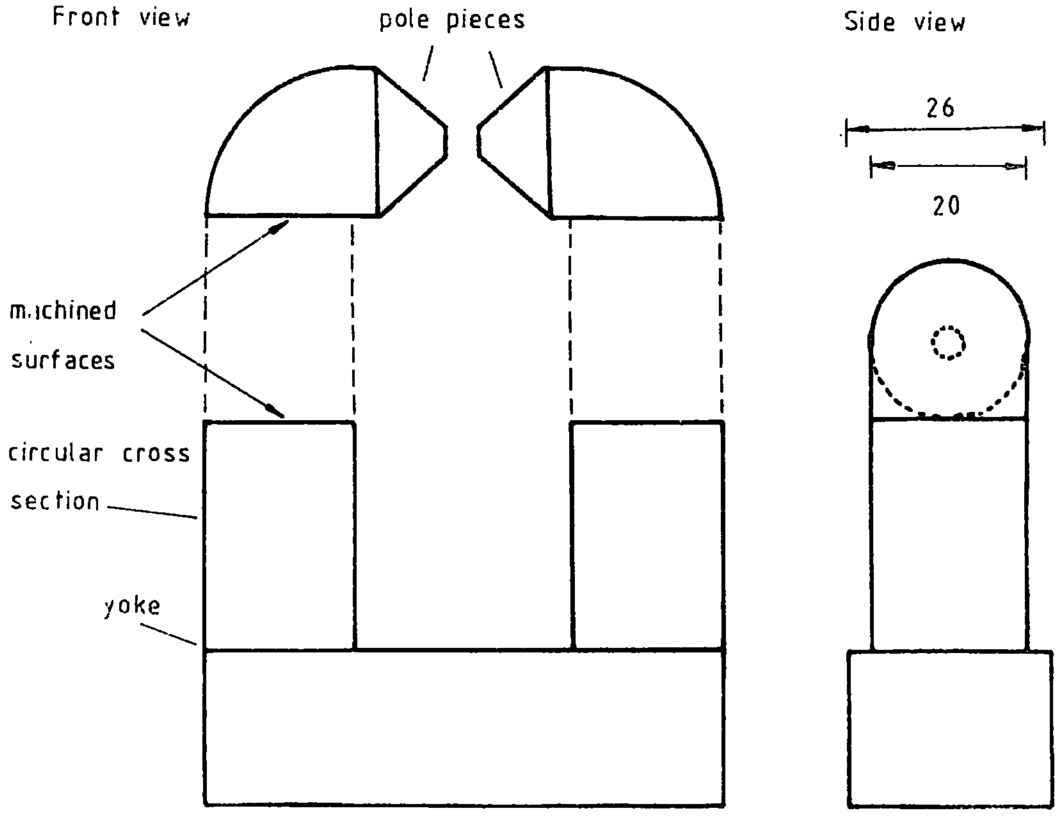

Fig 5.12(b) Soft iron circuit of magnet.

Thus the total ampère turn requirement is about 32000 for gap and cone plus about 35000 for core, i.e. 67000 ampère turns. This means that with 900 turns per solenoid, the current requirement would be in the region of 75 ampères.

For a solenoid of about 900 turns, using the copper strip of dimensions 0.95cms x 0.16cms, the estimated resistance is 1 ohm. Thus the power dissipation per solenoid is about 5600 watts.

5.7.3 Solenoid

For a proposed cross sectional area of 26cms x 12cms it can be seen that 23 pancakes may be wound, with 39 turns in each.

The copper strip of 0.95 x 0.16cm^2 cross section was used.

The windings are insulated from each other by wrapping nylon fishing line of 0.5mm thickness about the copper strip. This caused the pancakes to be wound somewhat tighter than originally envisaged. The pancakes were separated by strips of nylon 12cms by 2cms. Six of these were placed symmetrically between pairs of pancakes.

The pancakes were connected together by copper tags which were soldered to them, so that the sense of the current in the solenoid at any point would be always clockwise, or always anti-clockwise, depending on the applied voltage. A photograph of the solenoids under construction in situ on the yoke of the magnet is shown in Figure 5.13.

The solenoids are contained in watertight containers. These consist of concentric brass tubes closed at the top and bottom by tufnol circular plates. The inner tube just fits over the vertical cylindrical yoke sections.

Diagrams describing the detailed construction of these solenoid containers are shown in the first appendix. The solenoid is insulated from the brass walls by nylon sheets wrapped around the inner and outer curved surfaces of the solenoid.

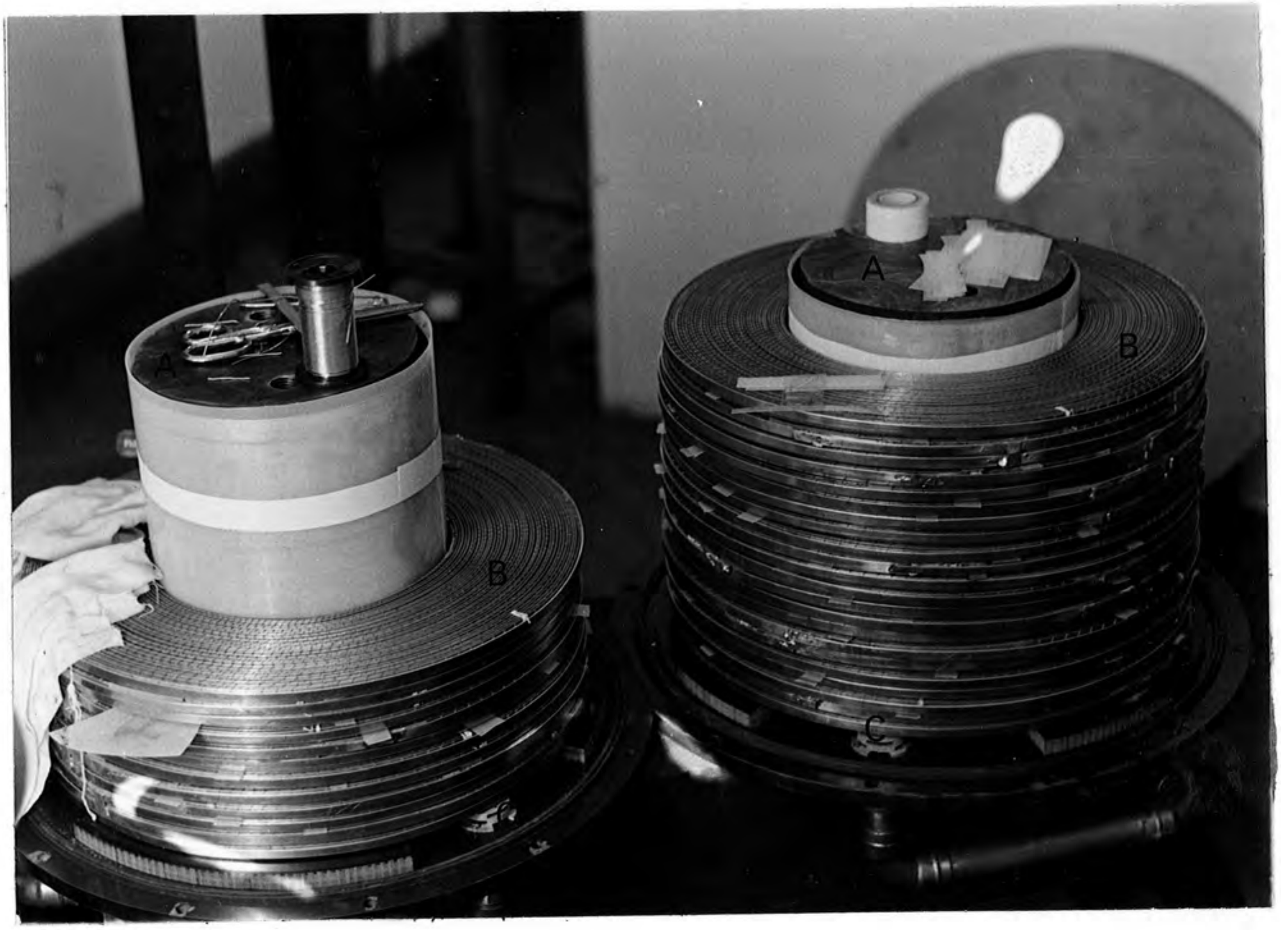

Fig.5.13 Photograph of magnet under construction, showing A, magnet core, B, copper wound solenoids, C, water inlets.

5.7.4 Iron circuit

In the original design, the magnetization data for the iron circuit was taken from Kaye and Laby (1956) for low carbon (0.1%) mild steel.

The actual material available was British Low Carbon Steel Grade A. The magnetization data for this was supplied by British Steel Research Association. It is not too different from that of the Kaye and Laby data and is shown in Figure 5.14.

The iron circuit consists of three pieces cast in shape, shown in Figure 12(b). The surfaces which are machined are also indicated. The casting was done at Jopling's Steel Foundry, Sunderland, and the machining of the pole pieces took place in the Department of Engineering at the University of Warwick. The rest of the machining and construction was carried out in the Physics Department, Durham University.

Each pole piece is secured to the yokes by two bolts which pass through the pieces into the yoke.

5.7.5 Rotation

The iron yoke is mounted on a steel plate which in turn is mounted on a turntable of diameter about 120cms.

Six adjusting screws are fixed to small blocks on the surface of the steel plate, around the outer edge of the base of the yoke. By means of these, the yoke may be centred fairly accurately on the turntable so that the axis of rotation passes through the centre of the pole piece gap.

The turntable was mounted on four wheels which located the turntable onto a track so that translation of the magnet might also be effected.

5.7.6 Water cooling

As the expected power dissipation might be over 5000 watts, water cooling was incorporated into the design of the magnet.

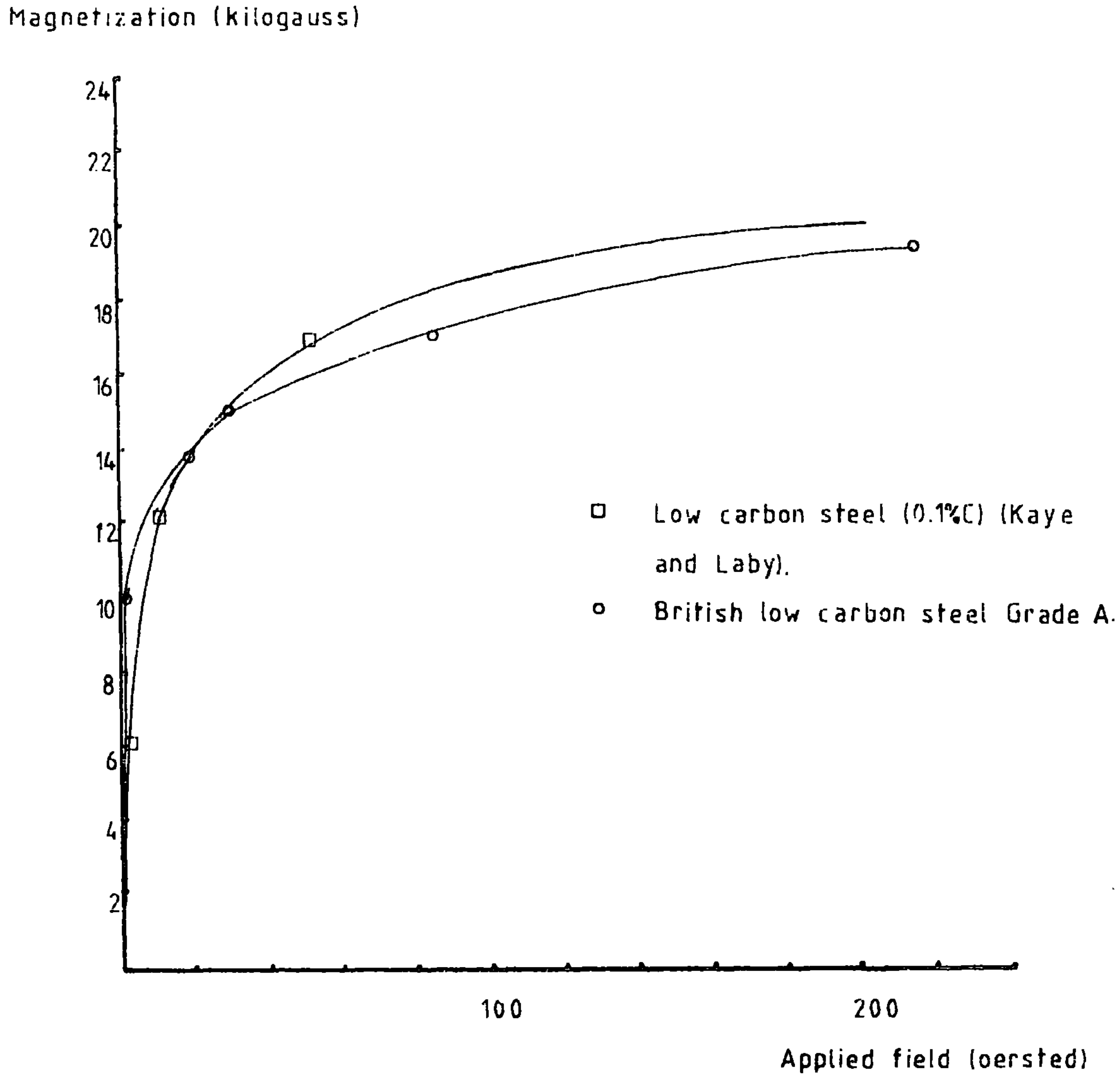

Fig.5.14. Magnetization data of Kaye and Laby (1956) and of the British Steel Research Association.

A closed circuit cooling water system has been used. This consists of the magnet in series with a heat exchanger, water pump and header tank. These were connected by reinforced clear plastic piping of 2.5cms inner diameter.

The heat exchanger was constructed on the basis of experience drawn from the water cooling system of another magnet in the laboratory, for which the heat dissipation was 7000 watts per solenoid. As oil did not prove to be an effective coolant in this system, distilled water was used, the water capacity of the present water circuit being about 50 litres.

5.7.7 Magnet calibration Curve

The magnetic field in the gap has been measured with the use of a Hall probe. The calibration curve is shown in Figure 5.15.

It is seen that the field of 10k Oe has been reached at a lower value of the current than had originally been calculated.

This indicates that the magnetization has increased more than expected with current, and that the stray flux has remained lower than expected. This might be explained by considering that for a certain distance from the gap the surface charge density becomes less the further away from the gap. The part of the pole which is saturated is taken into account for the calculation of the gap field and the rest of the pole where the charge density is lower will contribute only a fraction to the field. However, it is noted that beyond 10000 Oe, the field in the gap increases only very slowly. In this region, the iron must be approaching magnetic saturation and as the field from the solenoid itself cannot contribute to the gap field in this particular magnet construction, the gap field will not exceed a maximum of 0.82 M_{max} which is about 15.5k Oe.

The homogeneity of the field has also been investigated. The field was measured at various parts of the gap volume as indicated in Figure 5.15. A calibration curve is given for each location in the gap.

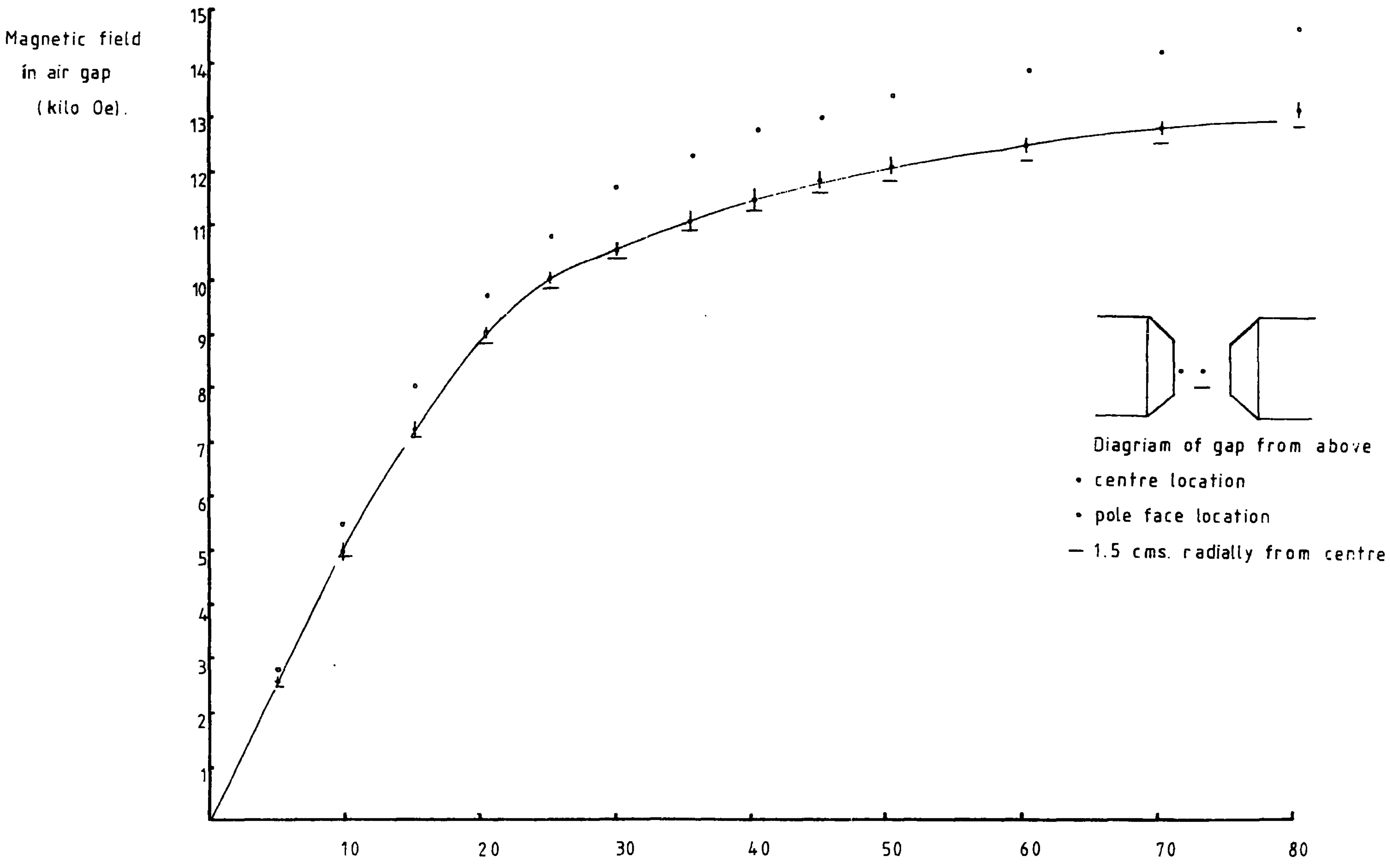

Fig. 5.15 Gap field versus solenoid current for three locations in gap field. For clarity, error bars are shown for just centre location points.

5.8 Suppliers' list

A list of materials' suppliers is given in the second appendix.

Chapter 6

The double crystal diffractometer

6.1 Basic design

The double crystal diffractometer consists of two vertical, parallel axes which are mounted in a single monolithic brass casting. Figure 6.1 gives the important dimensions of the instrument. The novel features of the design are:

1. the mounting positions for the crystal samples are below the main bodywork.
2. the separation of the axes is comparatively large.

In the final experimental arrangement, a magnetic field is applied to the specimen crystal. This field is supplied by the electromagnet described in Chapter 5. It would be difficult to mount this magnet above the diffractometer. Also, the reference crystal needs to be kept free from the path of any part of the magnet, which may be rotated. Thus the two requirements of the design, as mentioned above, are immediately apparent.

6.2 Bodywork

The main brass body of the diffractometer is supported at its four corners on a large steel gantry, which is bolted to the floor. In this arrangement the crystals are located about 85cms above the floor level.

The uppermost surface of the instrument is smoothly machined. Two circular inverted T grooves, one concentric with each axis, have been milled into this surface. These enable additional apparatus, such as detection equipment, to be attached directly to the bodywork.

The diffractometer is kept cool by water which passes through a duct enclosed inside the brass casting. The location of this duct is shown in Figure 6.1.

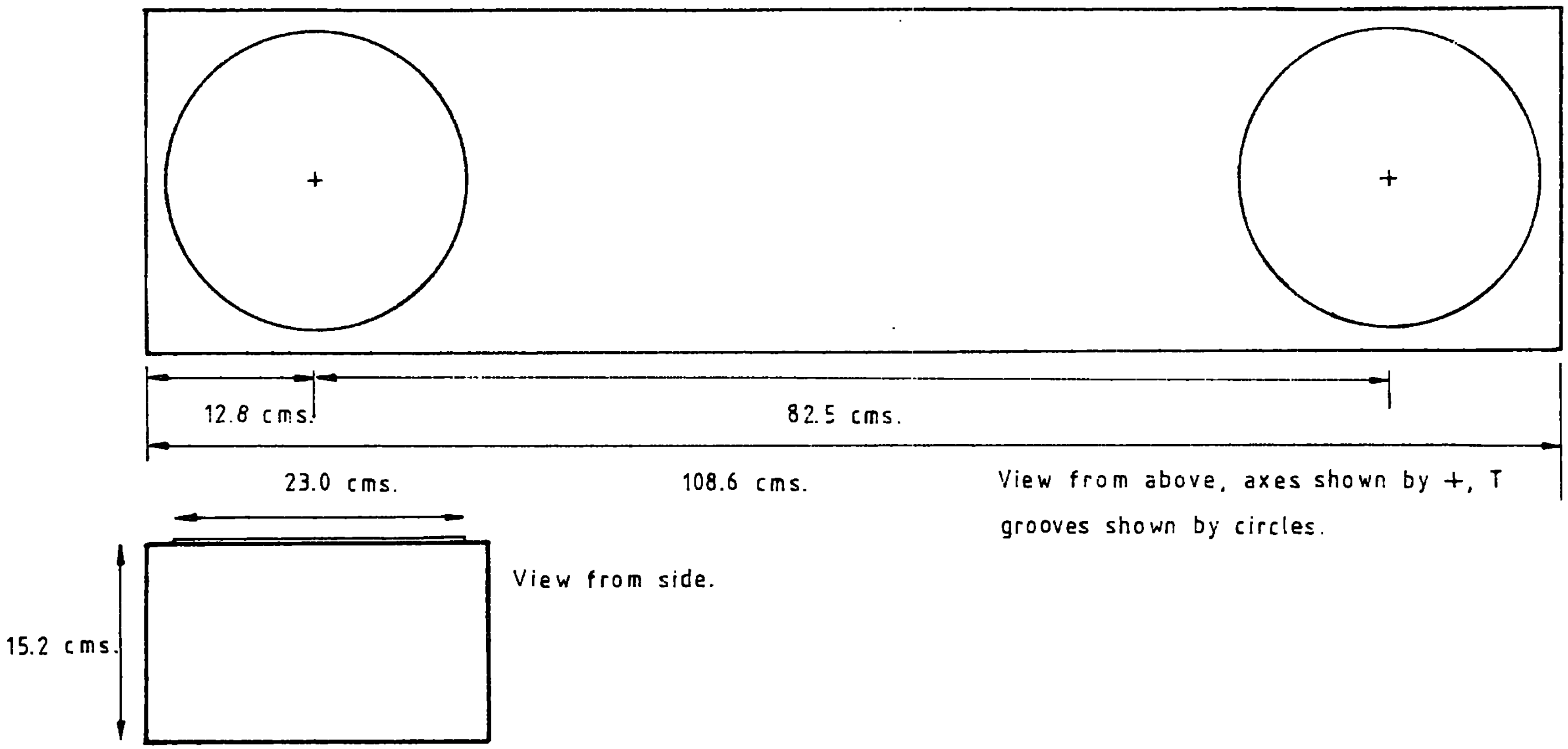

Fig.6.1 Schematic diagram of double crystal diffractometer.

+ Rotation axis
A Armature of fine axis
B Gear box
G Stepper motor
M Micrometer
W Sealed water channel

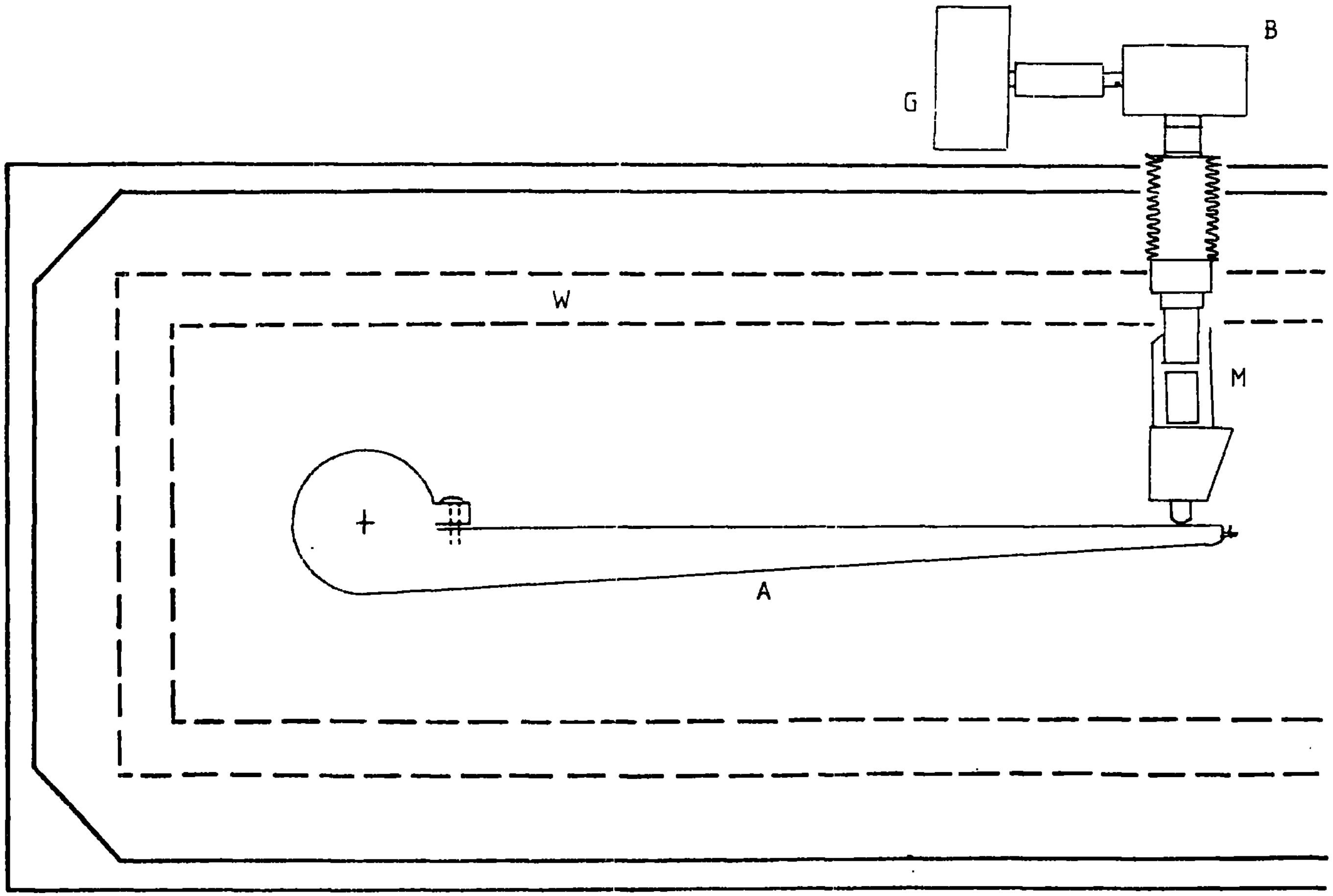

Fig.6.1 View of diffractometer from below. Half section shown.

Each of the two goniometers used with the diffractometer is supported on a vertical axle, the central line of which represents the rotation axis for each crystal. These axles, made from aluminium, are supported in the bodywork by pre-loaded bearings which allow their smooth rotation. The axles may be fixed to the rotation mechanisms by clamping rings.

6.3 Rotation axes, driving mechanisms

Each rotation axis is driven by a stepper motor, which acts via a gearbox, micrometer and armature combination. This arrangement is shown in Figure 6.1.

The reference crystal is normally mounted on the "coarse" axis. The armature to this has a radius shorter than that of the armature to the "fine axis, on which the specimen crystal is mounted. It is useful to know what angular rotation corresponds to one step of the motor for each axis. This information, together with other details of the rotation axes driving mechanisms, is given in Table 6.1.

Table 6.1

Details of rotation axis driving mechanisms

	"coarse" axis	"fine" axis
stepper motor steps per revolution	48	48
gear box ratio	20:1	90:1
armature length (mm)	146	292
angular rotation of axis for one step of motor (secs. arc)	0.932	0.103

For finer adjustment of the coarse axis, a piezo electric control is also attached to the armature.

For manual control of the rotation axes when setting up and prior to clamping, an armature is attached to each axle above the top surface of the diffractometer. Again, the extra sensitivity required for the fine axis is provided by the armature to this being of considerable length (~ 70cms).

The total angular rotation range for the "coarse" axis is approximately 5° and for the "fine" axis is also approximately 5°. When the limits of these ranges are reached by the armatures (attached to the micrometers), microswitches operate to reverse the sense of rotation.

The pulses required to drive the stepper motors are supplied from a pulse generator which operates in forward and reverse at variable speeds. A digital display enables the pulses fed to the motor to be monitored. The pulse generator may also operate between set limits which are shown on further digital displays.

6.4 X ray source

The X ray source is housed in a portable tube shield which in turn is mounted on a freely standing support. This may then be easily moved about the reference crystal. Ideally the tube shield ought to stand on a circular rail concentric with the rotation axis of the reference crystal. This modification is to be made after the work for this thesis is finished.

A considerable intensity of X rays is incident on the reference crystal. Thus the path between the source and the reference, and the reference crystal itself are closely shielded. An X ray collimator system, whose slit width is adjustable, is placed in the path of X rays between the source and the reference crystal.

The X ray tube is powered by a nearby Philips generator, and may operate up to 50kV at 24mA. The tube shield is fitted with an electrically operated shutter.

6.5 Detection apparatus

When the experimental arrangement does not include use of the magnet, a scintillator coupled to a photomultiplier tube may be used to monitor the final rocking curve. When doing this, the detector is mounted on a 'G' shaped support which is attached to the main body of the diffractometer at the circular T slot. The signal from the photomultiplier is fed directly into a ratemeter. The output of the ratemeter is given visually on an analogue scale and audibly through a speaker.

When the magnet is being used, the signal from the photomultiplier is decreased almost to zero owing to deflection of the electrons in the tube by the Lorentz $q \underset{\sim}{v} \times \underset{\sim}{B}$ interaction. In this case a Xe gas proportional detector is employed. The details of this are given in Table 6.2.

Table 6.2

Details of Xe gas filled proportional detector

Body		
	Material	Aluminium
	O.D. (mm)	19.1
	length (mm)	93
Window		
	Entry	Beryllium
	size (mm)	6 x 16
	thickness (mm)	0.02
EHT (volts)		1810
Energy range (keV)		6 - 30
termination		flying leads

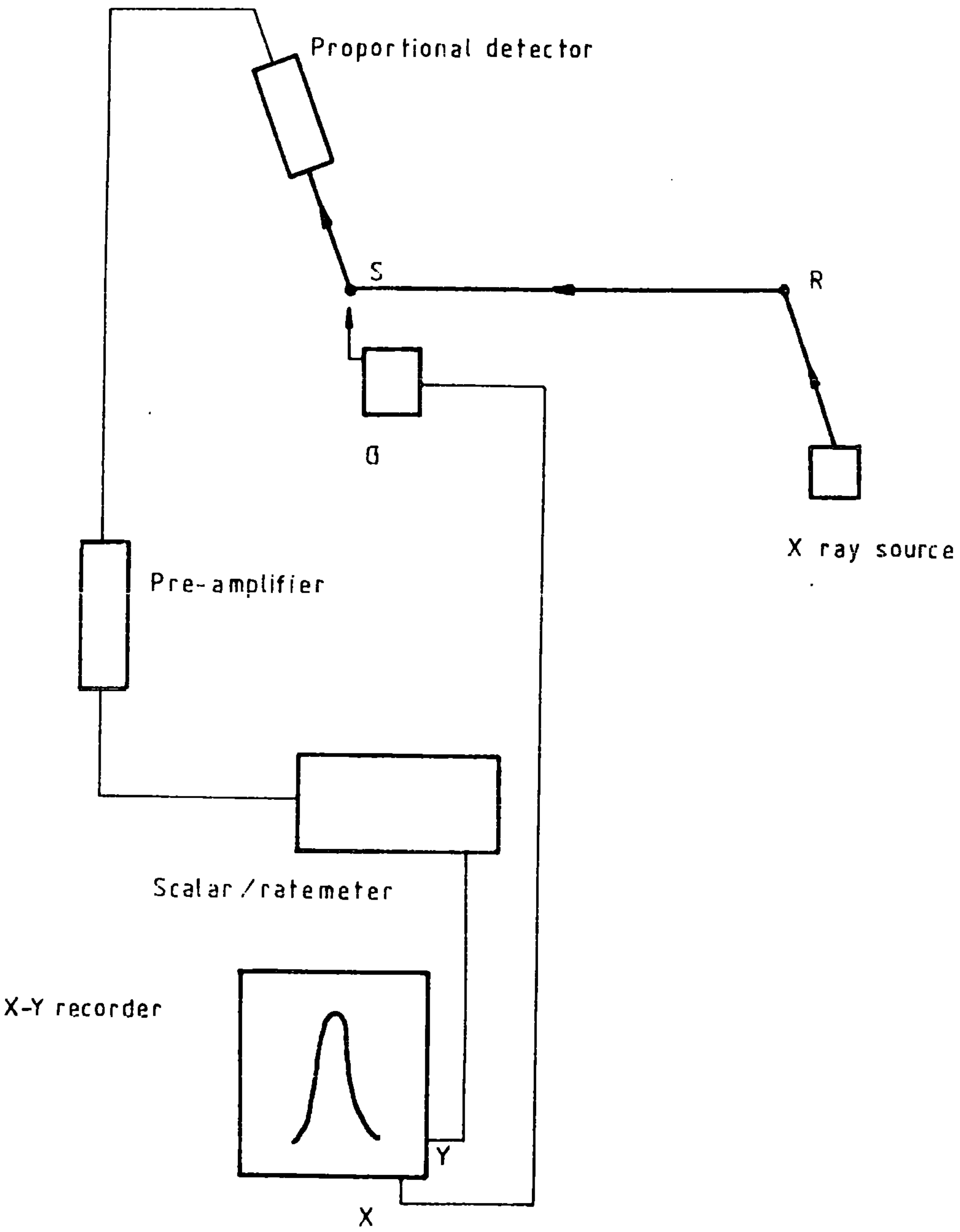

Fig.6.2 Schematic diagram of detection apparatus. R, reference, S, specimen, G, stepper motor drive.

It was noted that the energies of the Kα_1 absorption edges for Cu and Mo are 9keV and 17.5keV respectively, which fall within the range of the detector. The energy range of Ar is 3keV - 12keV. Thus the choice of Xe is obvious if Mo and Cu radiations are to be used.

The proportional detector is mounted in a protective brass/copper casing which is attached to a circular brass rail, concentric with the specimen crystal axis and scaled in degrees.

The signal from this detector is fed, via a pre-amplifier, into another ratemeter. This second ratemeter is an Ecko model, which is able to provide the E.H.T. voltage for the proportional detector. The output of the ratemeter is shown visually on an analogue scale. Also incorporated is a scalar counter/timer system and the rocking curve may be plotted using this.

The rocking curve may be displayed automatically on an X-Y recorder. The ratemeter provides an output which may be fed onto the Y axis. The angular rotation of the crystal through the rocking curve is fed from the shaft of the stepper motor through a cog wheel gear and helipotentiometer system onto the X axis of the recorder. This detection arrangement is shown in Figure 6.2.

The final experimental arrangement is shown in Figure 6.3.

6.6 Double crystal topography

Double crystal topographs may be taken in either the (+-) or the (++) setting with this apparatus. The arrangement in the (+-) setting was that shown earlier in Chapter 4. The detecting plate is simply mounted in a light tight plastic seal, and is supported on a stand near the specimen crystal. The X rays which pass through the plate may be monitored by the photomultiplier during the exposure so that any drift which might occur from the peak diffraction curve may be compensated.

W	Magnet water pump
X	X-ray tube shield
P	Lead shield
D	Diffractometer
S	Stepper motors
M	Magnet
R_1	Photomultiplier tube rate-meter
U	Stepper motor drive unit
R_1	Proportional detector rate meter
Y	X-Y recorder

Fig.6.3 Apparatus in final assembly.

CHAPTER 7

Alignment of the diffractometer

7.1 Various examples of double crystal diffractometer

In Chapter 4 reference was made to several works involving the double crystal diffractometer. The equipment used by Merz (1960) had an axes separation of a little more than 50 cms. The separation of the axes of Hart and Lloyd's (1975) diffractometer was apparently less than this. The relative closeness of the axes suggests that alignment of the diffractometer would be relatively simpler than in the case of well separated axes. This would be especially so in the case of Hart and Lloyd's arrangement, in which the first axis is a commercially available precision single axis goniometer.

In the cases of Okazaki (1973), Sykora (1970) and Bottom (1970) the Bragg angles were high, and geometrical requirements of fitting the apparatus together without blocking the X ray path led to larger separations of the axes. In Okazaki's equipment this was 60 cms, whilst in Sykora's equipment the total path length of the X ray beam was 3 metres. The longer path length suggests a considerably more tedious alignment task. Bottom suggested an initial coarse alignment procedure using a laser beam for crystals with the reflecting planes parallel to the surface. However, this method is, as suggested, only useful for such cases. Often the reflecting planes are not parallel to the surface of the crystal. The obvious example of this is the case of asymmetric reflections. However, even when crystals are used which have been cut so that the surface is parallel to the reflecting planes, there is often a deviation of typically a couple of degrees between the surface and plane. With the diffractometer described in Chapter 6, where the axes are separated by more than 80 cms, use of a laser beam for alignment when such crystals are mounted can lead to the beam diffracted by the first crystal being several centimetres off target by the time it passes the second crystal axis.

Also, it has been mentioned (Chapter 6) that the X ray source shield is free standing and mobile. With the help of suitable angular markings around the reference axis, the tube shield may be roughly aligned by eye.

Okazaki's alignment procedure is quite elaborate, involving rotation of several major parts of the apparatus. When the total experimental arrangement includes other large pieces of apparatus, as is the case of the work of this thesis, it is important to keep the alignment procedure as simple as possible.

7.2 Alignment

The alignment procedure adopted naturally involved two parts, alignment of the reference (first) crystal and further alignment of the specimen (second) crystal.

The circular entrance window of the photomultiplier tube detector was 2 cms in diameter. The larger entrance window, together with the faster response time, made this more suitable than the proportional detector during alignment. If the photomultiplier tube is placed so that its entrance window is at the specimen crystal position, then the setting of the X ray tube source and the first crystal needs to be made fairly critically, and in normal cases this would involve considerable time spent in trial and error.

The photomultiplier tube can however be supported on an optical bench, which is mounted below the diffractometer along the direction of the line joining the two crystal positions. This arrangement is shown in Figure 7.1(a). The photomultiplier tube is placed close to the reference crystal, so that with reasonable setting of this crystal and the X ray tube the entrance window of the detector is likely to be in a position to accept a given diffracted beam. The photomultiplier tube is gradually moved back towards the second crystal position. If, as this happens, the diffracted

(a) Optical bench arrangement.

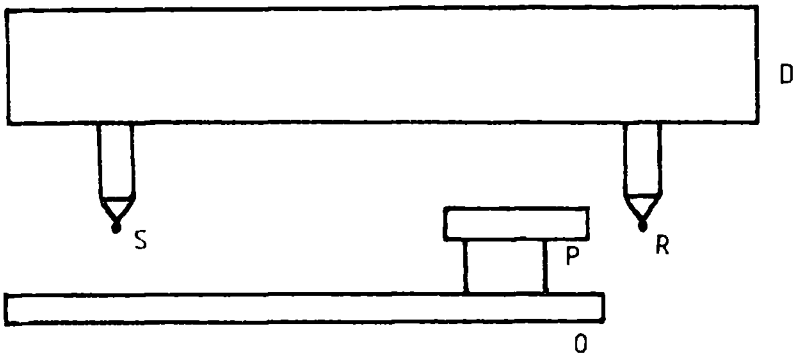

S Specimen, R Reference, P Photomultiplier, O Optical bench, D Diffractometer.
X X-ray source, $S_{1,2}$ Slits.

(b) Horizontal alignment.

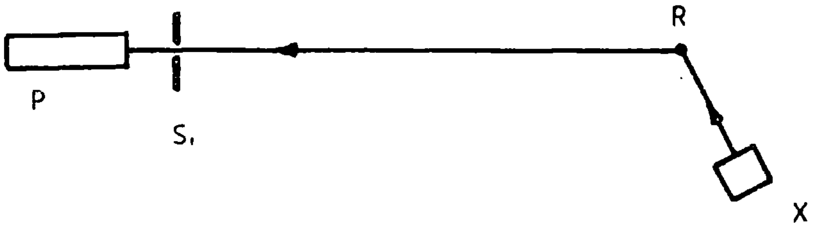

(c) Vertial alignment.

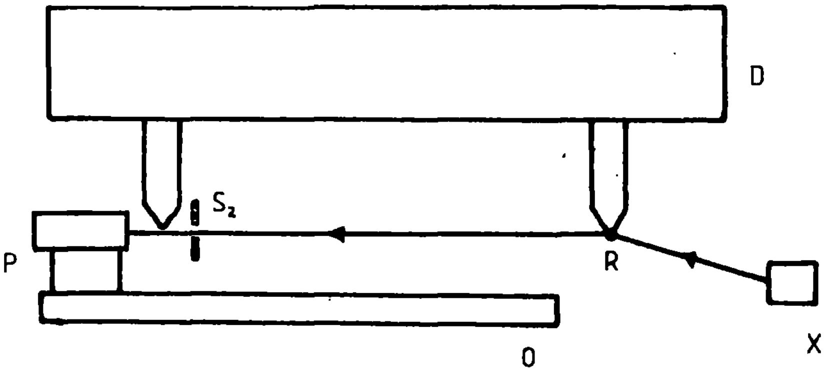

Fig.7.1 Diagram showing features of alignment procedure.

beam can be seen to be deviating from the line joining the two crystal positions, compensatory adjustments may be made to the X ray tube shield position. In order to check that the beam from the first crystal passes exactly through the rotation axis of the second crystal, a lead collimator of a couple of mms gap is placed just before the second crystal position, so that the vertical centre line of the collimator gap lies parallel to the second crystal rotation axis, and passes through the line joining the two crystal positions. This latter line can be checked for being fairly close to horizontal by similar use of the lead collimator. The arrangements are shown in Figure 7.1(b) and (c) respectively.

The second crystal, mounted on its goniometer so that the reflecting planes are parallel to those of the first crystal (this is discussed in more detail later), is put in place on the diffractometer. The photomultiplier tube is mounted on a ' G' shaped support shown in Figure 7.2(a). The entrance window is fairly close to the specimen crystal. However, the lower arm of the support is parallel to the expected direction of the beam diffracted from the second crystal, and the position at which the photomultiplier tube is suspended from this arm may be varied, as indicated in Figure 7.2(a). Thus once the second reflection has been picked up by the photomultiplier, the latter may be moved away from the crystal along the lower arm. When this adjustment is completed, the proportional detector, whose cylindrical axis is vertical, is placed directly in front of the entrance window of the photomultiplier. At this stage, the entrance window is about 12 cms from the second crystal, which is a little more than the minimum clearance required so that the magnet pole pieces may be moved into position without interfering with the aligned diffractometer. The final arrangement is shown in Figure 7.2(b).

The first attempts at actually picking up the second reflection made use of the stepper motor on the specimen crystal axis. The crystal was

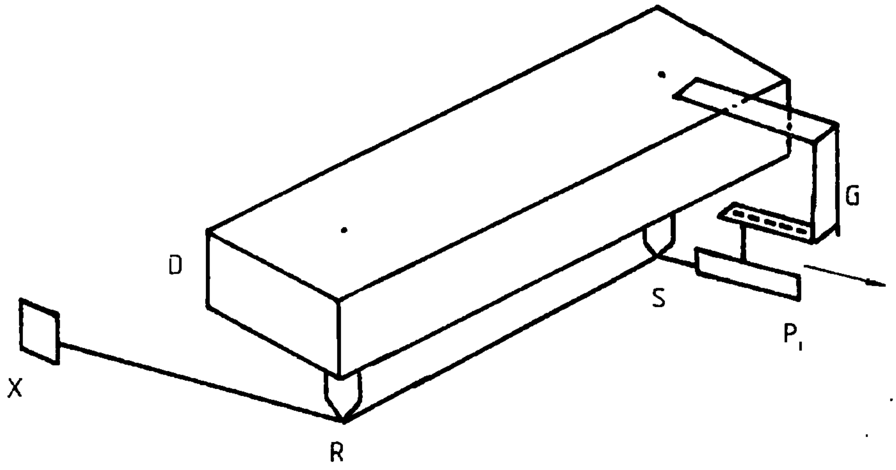

Fig.7. (a) Schematic diagram showing diffractometer with detector support.
X X-ray source, D Diffractometer, R Reference, S Specimen, P_1 Photomultiplier, G Detector support.

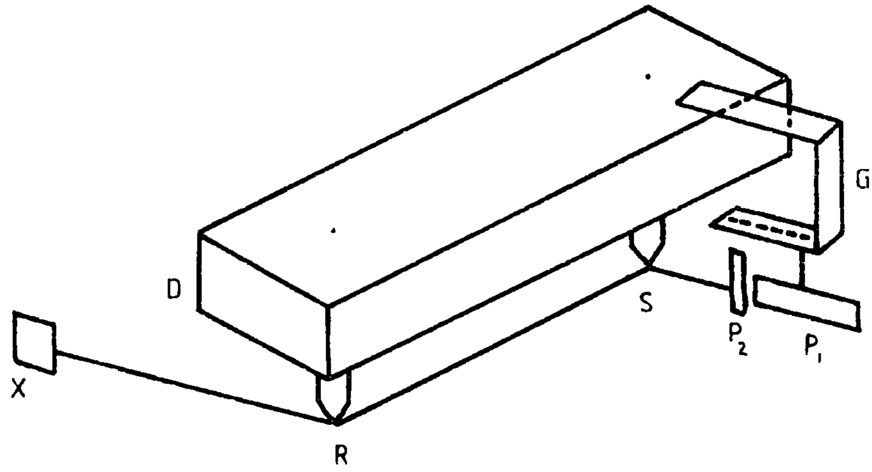

Fig.7.2(b) Final arrangement showing proportional detector, P_2, in position.

put into the approximate reflecting position, and the motor scanned through a maximum angle of about 2 degrees at a time (defined by the maximum possible displacement of the micrometer shaft). This procedure was, however, quite time consuming. It was decided that a long armature (70 cms) be attached to the specimen crystal axis above the upper surface of the diffractometer. It was found that by slow, careful manual adjustment of the angular position of this long armature, with the rate meter time constant and full scale deflection values being at the lowest settings, the reflection from the specimen crystal could be located. In fact this manual procedure proved to be considerably easier than had been originally anticipated.

Finally, slight adjustment normally needs to be made to the goniometer setting of the second crystal in order to bring the reflecting planes of both crystals as close as possible to being parallel, and thus to maximize the peak reflected intensity and to narrow the rocking curve down as much as possible.

3. Effect of absorption of X rays in air

In order to estimate the effects of absorption of X rays by air, some simple calculations were performed for MoKα, and CuKα, wavelengths. The following information regarding the X ray absorption parameters for air was taken from the "Handbook of Chemistry and Physics" (1961). Radiation traversing a layer of substance is reduced in intensity by a constant fraction, μ, per centimetre. After penetrating to a depth x, the radiation has intensity given by

$$I = I_o e^{-\mu x}$$

where I_o is the intensity at the surface. μ/ρ is the mass absorption coefficient, where ρ is the density of the material. At a temperature t and under a pressure of H cms of mercury, the density of air is given by:

$$\rho = \frac{0.001293}{1 + 0.00367t} \; \frac{H}{76}$$, where the units are in grams per

cubic centimetre. At t = 20°C, H = 76 cms of mercury, the density ρ is 0.001205 gms cc^{-1}.

At a wavelength of 0.7Å, the mass absorption coefficient of oxygen is 1.22 and of nitrogen is 0.87. A simple weighting of these was made to produce the mass absorption coefficient for air of 0.94. If the path length between the two crystals is considered, that is about 82 cms, a value of I/I_o of 0.90 is obtained, which corresponds to MoKα radiation. Similarly for radiation of wavelength 1.5Å, a weighted mass absorption coefficient was found to be 8.18, where the individual mass absorption coefficients for nitrogen and oxygen are 7.50 and 11.10 respectively. For the same path length, the value of I/I_o comes out to be 0.45. This corresponds to the case of CuKα radiation. Use of CuKα radiation will be described in more detail in Chapter 8.

It can be seen that for MoKα characteristic radiation, not a lot would be gained in evacuating the X ray path of air. In fact a length of steel tube (80 cms) was placed between the two crystals when the diffractometer was aligned. The ends were sealed off with mylar windows and the tube could be evacuated. The rate meter reading at the rocking curve peak was noted with an air path between the two crystals, and hardly changed at all when the X ray path was evacuated. It is fortunate that there was no need to include the evacuated tube in the experimental arrangement as such an addition would certainly have proved to cause an inconvenience when the magnet was being moved into place.

4. Initial test alignment

The first crystals to be mounted on the diffractometer were samples of device grade silicon. This initial test alignment was useful for two purposes. Firstly it was needed to be seen that the proposed method of alignment would in fact be suitable. Secondly it was necessary to check that the diffractometer, as it had been constructed, would give potentially sufficient sensitivity to make it worthwhile in continuing with the magnetostriction experiment.

The silicon crystal used was of plate-like form. Two samples were taken from the same original specimen, whose surface was approximately parallel to a {111} plane. The orientations of the crystals, each being mounted on separate goniometers, were checked with the help of Laue photography. The interpretations of the Laue photographs were made with a Grenninger chart and a standard (001) stereographic plot according to the description given by Cullity (1956).

It was noted that the (111) plane was not in fact parallel to the surface. The plane and surface were deviated by an angle of two degrees, as measured with the goniometer, and the Grenninger chart. The necessary adjustments were applied to the settings of the goniometers to make the orientations of both crystals identical, as well as could be ascertained with Laue photography. It was seen by eye with the help of a variable angle set square that both crystals were tilted on the goniometer by two degrees.

One of the goniometers was mounted on the reference axis. It was checked by eye that the rotation axis passed through the crystal face, and with the help of a fluorescent X ray beam detector it was seen that the X ray beam was incident at the position where the rotation axis passed through the crystal face. Such checks are somewhat easier when the reflecting plane is exactly parallel to the surface, but some doubt exists in knowing whether the rotation axis is exactly parallel to and passes through the reflecting plane when there is a deviation between the plane and surface.

The alignment of the first crystal proceeded, as has been described, to the point where the second goniometer could be mounted on the second axis. The (444) reflection, with Bragg angle 26.96°, was used. For lattice parameters and X ray wavelengths, the "Handbook of Chemistry and Physics" (1961) was used. Before this was carried out, however, the goniometer on the first axis was removed and replaced by the second goniometer and crystal. With nothing else adjusted at all, it was noted that the diffracted beam from this second crystal also passed through the lead collimator, placed before the "second crystal" position as described previously. As the width of the collimator was about two millimetres, this test implied that the orientations of the two crystals were themselves the same approximately to within an angle given by $\tan^{-1} 0.2/82.5 \simeq 0.15^{\circ}$. This angle compares favourably with the tilt angle of 10′ arc quoted by Bottom (1971) who used a laser beam for the coarse alignment. In the first stage of the alignment, the collimator between the X ray source and first crystal was about 100μm in width and about 0.5 cm in height. With an X ray tube setting of 6mA and 50kV, ample diffracted intensity was available. The second part of the alignment now proceeded as described. The collimator slit width was increased to 1.5mm. The initial rocking curve width obtained was about 24" arc. However, after a slight adjustment of the tilt of the second crystal was made, a rocking curve width of 5" arc was obtained. This is shown in Figure 7.3. The rocking curve is fairly symmetric, and although narrower rocking curve widths have been quoted in the literature, one can see that from an inspection of the slope of the flank, a 15% change in signal, which may easily be detected, implies a value of $\Delta\theta$ of 0.5" arc. This in turn, at a Bragg angle of $\theta_B = 26.96^{\circ}$, implies a relative change in "d" spacing of $\frac{\Delta d}{d} \simeq 5 \times 10^{-6}$. This corresponds to a typical value of magnetostrictive strain.

5. Instrumental errors

The errors associated with X ray diffraction measurements have been discussed by Bond (1960). The discussion was extended by Bottom and Carvalho (1970) to cover the case of the double crystal diffractometer. The errors listed by Bond are given as follows:

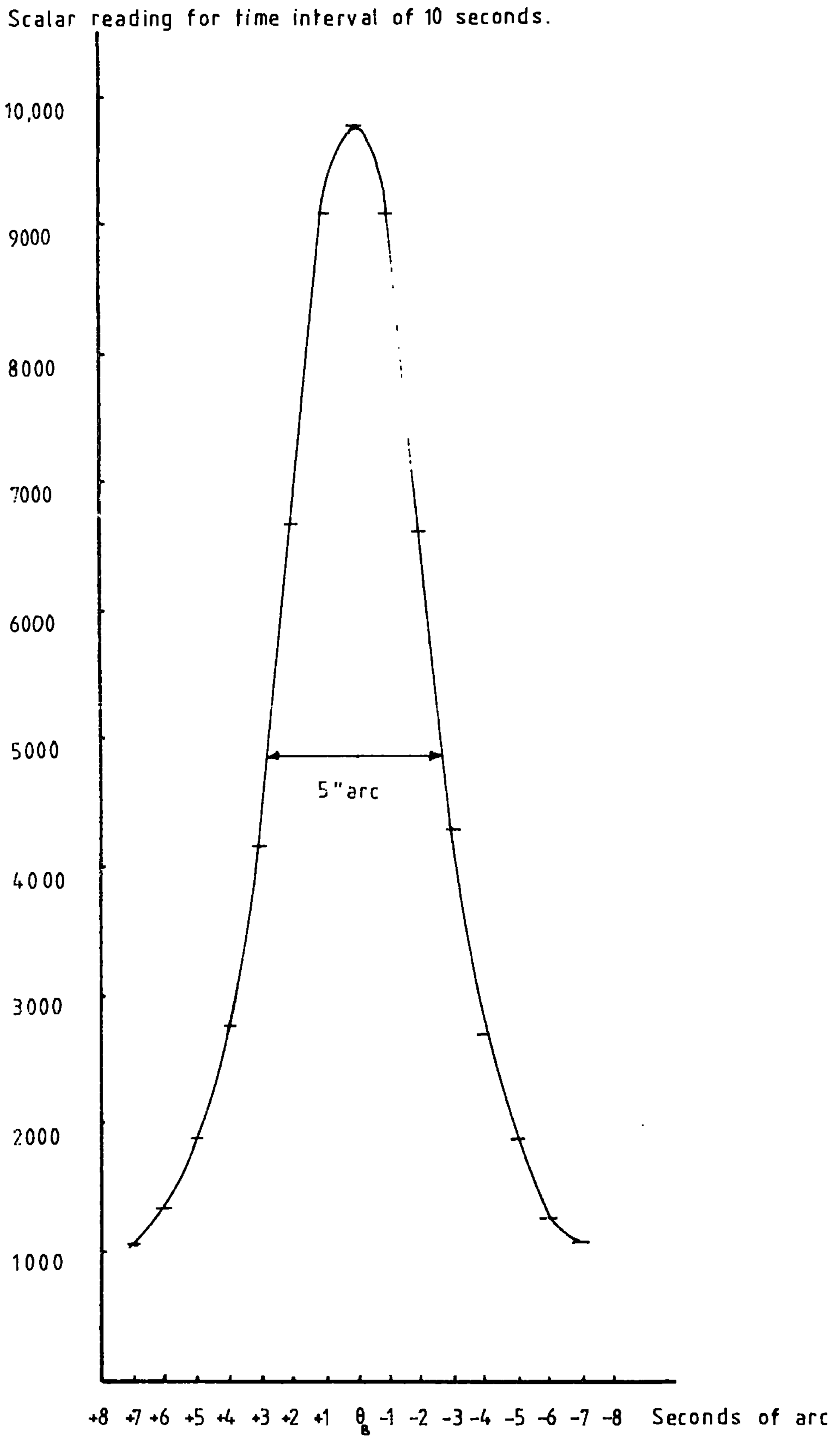

Fig 7.3 Rocking curve of (444) reflection of Si aligned in the (+,−) parallel setting.

(i) Error owing to lack of knowledge of X ray wavelength

(ii) Error associated with the determination of the zero position on the angular scale

(iii) Absorption error owing to different distances traversed in the crystal by X rays of different wavelength

(iv) Error owing to the effect of refraction

(v) Errors owing to polarization factors, which in general are very small except at large values of Θ

(vi) Eccentricity error owing to misalignment of the goniometer rotation axis with the diffraction surface of the crystal

(vii) Axial divergence error which is associated with the finite height of the collimator slit

(viii) Crystal tilt error

(ix) Angle reading error

(x) Dispersion error

Errors (i) and (ix) may here be considered together. From the differentiated forms of Bragg's equation $\frac{\Delta d}{d} = \frac{-\Delta\Theta}{\tan\Theta}$, it can be seen that in order to obtain the fractional change in "d" spacing no knowledge of the wavelength is required. However, knowledge of Θ is required. Θ could be determined with some collimator slits system with an error of typically some minutes of arc. Θ may also be determined from Bragg's equation using accepted wavelengths and lattice parameters given in the literature. An error also is associated with this. In the work of this thesis the latter method was employed. If the geometrical centre of the $K\alpha_1$ reflection (usually) from the first crystal is always used, then whatever error exists with this method, it will always at least be consistent.

The zero error will be non effective in the case of the present instrument.

The effects of absorption, refraction and polarization factors, errors (iii) to (v), are to cause displacements of the peak of the diffraction maximum. In the case of the double crystal diffractometer, it is not the absolute position of the rocking curve maximum that is required but the displacement of the rocking curve. Hence these effects may be neglected.

The eccentricity error (vi), has been discussed in the previous section. It depends essentially upon the care used in the construction of the device.

The effects of using collimator slits in the instrument have been discussed in Chapter 4. It has been seen that the shape of the rocking curve does not depend on the slit widths. If collimator slits systems are used for angle determinations then there are axial tilt errors associated with the length of the slits.

An error can occur in the determination of $\Delta d/d$ if the crystals have tilts (error (vii)). If the normal to a set of diffracting planes makes angle Δ with the plane of the incident and diffracted rays, then the wavelength diffracted is given by $n\lambda = 2d \sin\Theta_1 \cos\Delta$, where Θ_1 is the apparent Bragg angle. If Δ_1 is the angle of tilt of the first crystal and Δ_2 the angle of tilt of the second crystal, then: $n\lambda = 2d \sin\Theta_1 \cos\Delta_1$ and: $n\lambda = 2d \sin\Theta_2 \cos\Delta_2$.

When the lattice spacing of the specimen crystal has changed, then the second of the above two equations may be written:

$$n\lambda = 2(d + \Delta d) \sin (\Theta_2 - \Delta\Theta) \cos \Delta_2.$$

Δ_1, Δ_2 and Θ_1 are eliminated from these equations to give:

$$\frac{\Delta d}{d} = (1 - \cos \Delta\Theta + \cot \Theta_2 \sin \Delta\Theta)/(\cos \Delta\Theta - \cot \Theta_2 \sin \Delta\Theta)$$

which may be rewritten with approximation as:

$$\frac{\Delta d}{d} = \Delta\Theta \cot \Theta_2 + \frac{\Delta\Theta^2}{2} .$$

If $\Delta_1 = \Delta_2$, then $\Theta_1 = \Theta_2$, and no error is introduced in the measurement of the change in lattice spacing. If $\Delta_1 \neq \Delta_2$, then $\sin \Theta_2 = (\cos \Delta_1/\cos \Delta_2) \sin \Theta_1$, and $\Theta_2 \neq \Theta_1$. The efforts made to minimize the effects of tilt in the present case have been described in the previous section. At best, it may be said that the angles associated with tilt could be kept to about 10′ of arc with some certainty. However, after slight adjustment of the second crystal to reduce the rocking curve width, it is hoped that Δ_1 becomes sufficiently close to Δ_2, so that any tilt error may be small.

The expression for dispersion has been given in Chapter 4. In the particular measurements to be described in Chapter 8 the reference crystal lattice spacing differs from the specimen crystal lattice spacing such that $\frac{\Delta a}{a} = 1.5 \times 10^{-3}$. The value of $\frac{\Delta\lambda}{\lambda}$ (where λ is the wavelength of MoKα_1 radiation) is then equal to 1.2×10^{-4}, and the value of $[\tan \theta\ (\lambda_o, n_A) - \tan \theta\ (\lambda_o, n_B)]$ has magnitude 4.2×10^{-4}. Thus the additional reflection width $\delta\beta$ owing to dispersion is approximately 5×10^{-7} radians, or 10^{-1} seconds of arc. Thus it can be seen that reliable measurements of small lattice strain may still be made.

Chapter 8

Magnetostriction Measurements

8.1 Introduction

A study has been made of the magnetostriction in the material $Tb_2LuFe_5O_{12}$. The method used was that outlined at the start of Chapter 4. In this method, the rocking curve was obtained from rotation of the specimen crystal, which here was the second crystal. The latter was set on the flank of the curve. When the magnetization was changed from one direction in the crystal to a direction perpendicular to the first, the movement of the recorded X ray intensity along the flank of the curve was noted, and from this, a value of one of the magnetostriction constants was obtained.

A study of the mixed rare earth garnet mentioned above was useful for several reasons. As will be pointed out later, there are 180° domains only in the sample. It has been pointed out in Chapters 3 and 4 that X ray techniques, which have been used to study magnetostriction without the help of an applied magnetic field, yield the spontaneous magnetostriction constants only of the materials which have magnetic domain walls other than of the 180° type.

The expected values of the magnetostriction constants of the material are fairly low ($<10^{-5}$). Thus a measurement of one of them using the double crystal diffractometer took advantage of the high resolving power of the instrument. Also, it will be seen that the magnetic field required to rotate the magnetization through 90° from the axis of easy magnetization was fairly high, and the measurements which have been made have required that the magnet described in Chapter 5 be used to almost its full capacity.

8.2 Samples

The rare earth iron garnet (R.I.G.) samples used in the experiments were kindly supplied by Dr W.T. Stacy of Philips Research Laboratories. The garnet $Tb_2LuFe_5O_{12}$ was deposited in the form of a thin film on a substrate of non magnetic gadolinium gallium garnet (GGG) by liquid phase epitaxy. The substrate has been Czochralski grown, and was in the form of a circular thin platelet. There was a deposit of film on either side of the platelets. The G.G.G. substrate of a further garnet $Eu_{2.7}Lu_{0.3}Fe_{4.3}A\ell_{0.7}O_{12}$, which was similarly grown, was also employed in the experiment. A description of both these garnets is given in Table 8.1.

Table 8.1

Description of garnet films

Composition	$Eu_{2.7}Lu_{0.3}Fe_{4.3}A\ell_{0.7}O_{12}$	$Tb_2LuFe_5O_{12}$
Thickness (μm)	4μm	3.8μm
Platelet diameter (cms)	2.7	2.0
Expected value of λ_{111}	$+ 1.5 \times 10^{-6}$	$+ 7.2 \times 10^{-6}$

In the above table, an expected value of the magnetostriction constants, λ_{111}, has also been given. As Bobeck et. al. (1970) have pointed out, such expected values may be determined by linear weightings of the respective magnetostriction constants of the pure rare earth iron garnets. The experimental room temperature valuesof the R.I.G. series have been determined by Iida (1967), as was pointed out in Chapter 1. The values are shown in Table 8.2, and these values have been used in the linear weightings.

Table 8.2

Room Temperature Rare Earth Garnet Data

	λ_{111} (x 10^{-6})	Lattice constant (Å)
Sm	-8.5	12.53
Eu	+1.8	12.52
Gd	-3.1	12.47
Tb	+12.0	12.43
Dy	-5.9	12.39
Ho	-4.0	12.37
Y	-2.4	12.36
Er	-4.9	12.35
Tm	-5.2	12.33
Yb	-4.5	12.30
Lu	-2.4	12.27

Bobeck et. al. (1970)

8.3 Observations of domains by the Faraday method

The garnet platelets are coloured and transparent. The 180° domains in the thin films may be rendered visible by the Faraday method, described by Craik (1975). A beam of polarized light passing through a magnetic material undergoes a rotation of its plane of polarization owing to the component of the specimen magnetization lying along the direction of propagation. The angle of rotation depends on the magnitude of the sample magnetization and the distance the light travels through the sample. The sense of the rotation is determined by the magnetization direction. In the arrangement used here, shown in Figure 8.1(a), white light is passed through a piece of polaroid, then through the sample, further through a second polaroid, and finally into an optical microscope. At the crossed position of the polaroids, the contrast for each domain is the same. If the polaroids are offset from the crossed position by a small angle β, then the intensity of light entering the optical microscope, which is focused on the garnet film, is proportional to $\sin^2(\beta\pm\alpha)$, where α is the angle of Faraday rotation. It can thus be seen that the contrast of the domains is a maximum when $\alpha = \beta$. The domains observed were of the usual vermicular nature characteristic of such magnetic uniaxial films. As a garnet film was deposited on both sides of the substrate platelet, two sets of domains were able to be brought into focus.

The uniaxial anisotropy field has been determined by the technique described by Kurtzig and Hagedorn (1971). A magnetic field was applied parallel to the plane of the sample platelet. This caused rotation of the magnetization within each domain towards the direction of the applied field. As the latter was increased, the Faraday contrast between adjacent domains decreased, and the separation between adjacent domain walls also decreased. The minimum field required to rotate the magnetization into the plane of the sample was assumed to be the uniaxial anisotropy field, which then could be

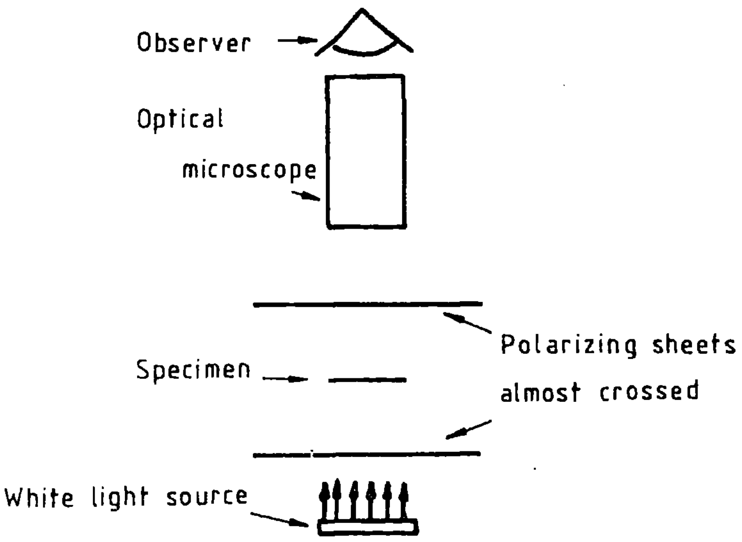

Fig.8.1(a) Arrangement for observation of domains in garnet thin films by the Faraday magnetooptical method.

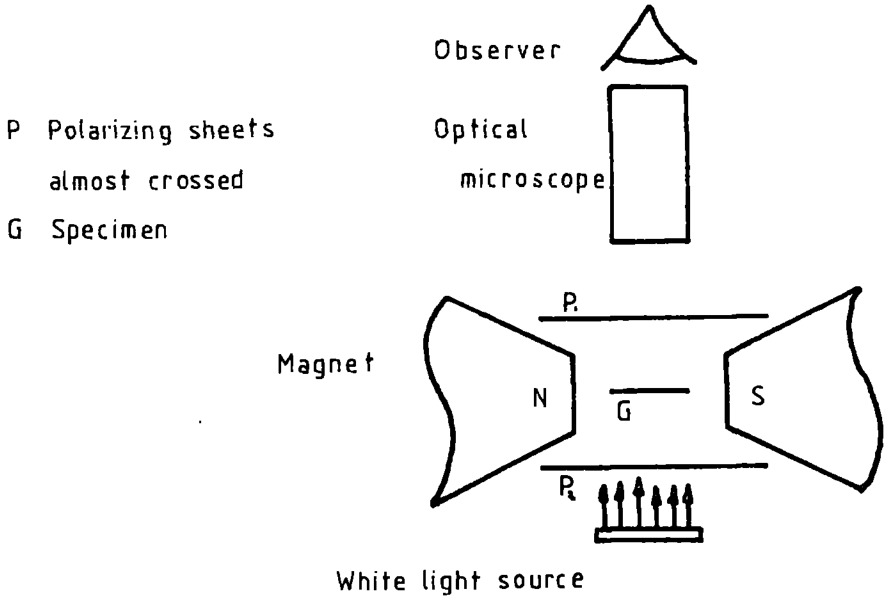

Fig. 8.1(b) Arrangement for determination of uniaxial anisotropy field by the magnetooptical method.

determined within about 15%. The magnetization was known to have rotated into the plane of the sample when all the domain contrast was eliminated.

The experimental arrangement is shown in Figure 8.1(b). The magnetic field indicated in the diagram was supplied by the magnet described in Chapter 5. The considerable free volume around the conical pole pieces made the positioning of the microscope quite an easy operation. The microscope itself had no ferromagnetic parts, and so did not move when the field was switched up.

Various parts of the sample were investigated. Each was mounted on a glass plate and fixed in position by a very small amount of araldite. It was noted that for the parts of the $Tb_2LuFe_5O_{12}$ sample investigated, the magnetic domains disappeared when the applied field reached 6.5 to 7.5k Oe. It was thus concluded that the uniaxial anisotropy field lay in this region also. However, as will be pointed out later, the anisotropy may be greater than this in some other parts of the film specimen. Kurtzig and Hagedorn (1971) investigated the anisotropy of a thin film of $Er_2Eu_1Fe_{4.3}Ga_{0.7}O_{12}$ deposited by liquid phase epitaxy on the (111) surface of a $Gd_3Ga_5O_{12}$ substrate. This was seen to have a uniaxial anisotropy field of 6.5k Oe. A similar, but more elaborate technique of anisotropy field investigation has been described by Krumme et.al. (1972). However, the method of Kurtzig and Hagedorn (1971) had the advantage of simplicity. It would have been more difficult to fit the apparatus described by Krumme between the pole pieces of the magnet, even though a considerable spare volume was available.

8.4 Alignment

The alignment of the diffractometer with the garnet materials essentially followed the procedure outlined in Chapter 7. Laue photographs were taken of both samples, and these indicated that the (111) plane was parallel to the sample surface in each case. The correct positioning of the samples relative to the diffractometer axes then, with the help of a variable angle set square, was comparatively straightforward.

A summary of the Bragg angles which could be used for the garnet $Tb_2Lu_1Fe_5O_{12}$ is given in Table 8.3.

Table 8.3

Bragg angles used with $Tb_2Lu_1Fe_5O_{12}$

Reflecting planes	Bragg angle
(12,12,12)	36.6°
(14,14,14)	44.0°
(16,16,16)	52.5°
Radiation	$MoK\alpha_1$
Wavelength	0.709Å
Lattice constant	12.38Å

The value of the lattice constant used was obtained from a linear weighting of the relevant values shown in the second part of Table 8.2, which gives the lattice constants of the pure R.I.G's. Initially, experiments were carried out with a standard laboratory electromagnet which had conical pole pieces. This was before construction of the large electromagnet was complete. A Bragg angle greater than 30° had to be used, since only then would no part of the magnet be positioned in the X ray beam path. It can be seen then from Table 8.3 that (12,12,12) was a suitable reflection for use here. In later experimental work, when the magnet described in Chapter 5 was employed, the minimum Bragg angle which could be used was 42°. The (16,16,16) reflection therefore was the most suitable reflection here. It was observed that the intensity of the (14,14,14) reflection was considerably less than that of the (16,16,16) reflection.

Hart and Lloyd (1974) have pointed out that their second crystal was used as the reference crystal. In the present experimental arrangement, it would have proved quite difficult to shield the first crystal adequately with lead if the magnet had been located at the same position. Therefore, in all the experimental runs, the magnetic field was applied to the second crystal, and the first crystal was the reference crystal.

When the large electromagnet was in position, stray magnetic field measurements were made with a Hall probe. It was noted that the maximum observable stray field at the first crystal position was 50 Oe. The substrate/ $Eu_{2.7}Lu_{0.3}Fe_{4.3}A\ell_{0.7}O_{12}$ was used as the reference crystal, and it was thought that such a small field would not have caused the crystal to move at all. It was actually observed that when this crystal was freely mounted on a glass plate, it showed no visible signs of movement till magnetic fields of several k Oe had been reached. The reference crystal, therefore, was mounted against a circular brass ring, and held in position by a very small amount of araldite, as indicated in Figure 8.2.

When the reflection from the second crystal (referred to as the second reflection) was being located, it was observed that the reflection from the substrate was more intense than the reflection from the film by a factor of 3 to 4. The second reflection from the substrate was initially found to be typically 12 seconds of arc wide at the peak half maximum, while the second reflection from the film was found to be typically 20 seconds of arc wide. These widths agree quite well with those quoted by Hart and Lloyd (1974) and Stacy et.al. (1974a). The two reflections were separated by several hundred seconds of arc, in agreement with similar observations of Hart and Lloyd (1974) and Estop et.al. (1976). The increased width of the film second reflection, as pointed out by Hart and Lloyd (1974), was due to the small film thickness. Also some dispersion was introduced when the film reflection was used. This has been treated in Chapter 7. As time proceeded, the widths of the rocking

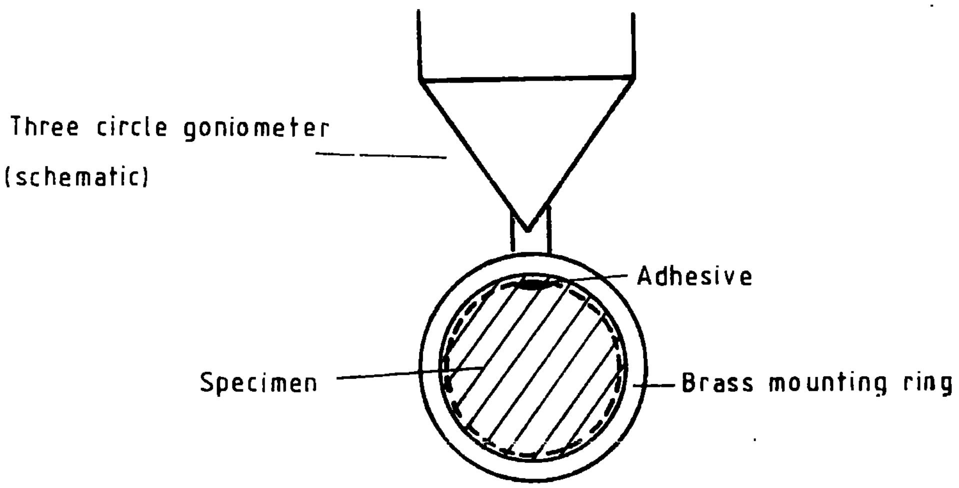

Fig.8.2 Schematic diagram of reference crystal mounting arrangement.

Fig. 8.3 (a) Film reflection rocking curve used to obtain the result of figure 8.9(e).

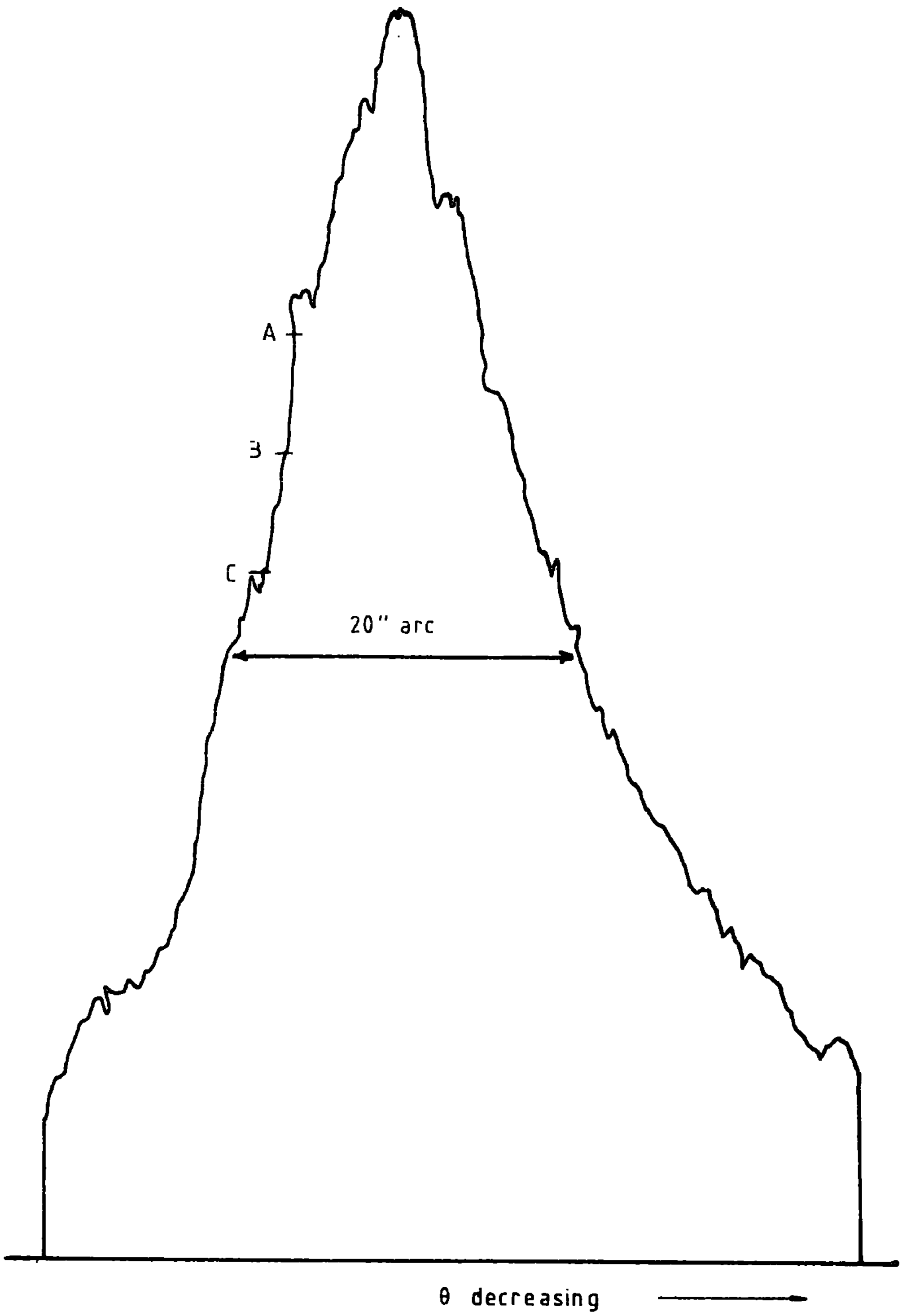

Fig.8.3(b) Film reflection rocking curve used to obtain the result of figure 8.9(f).

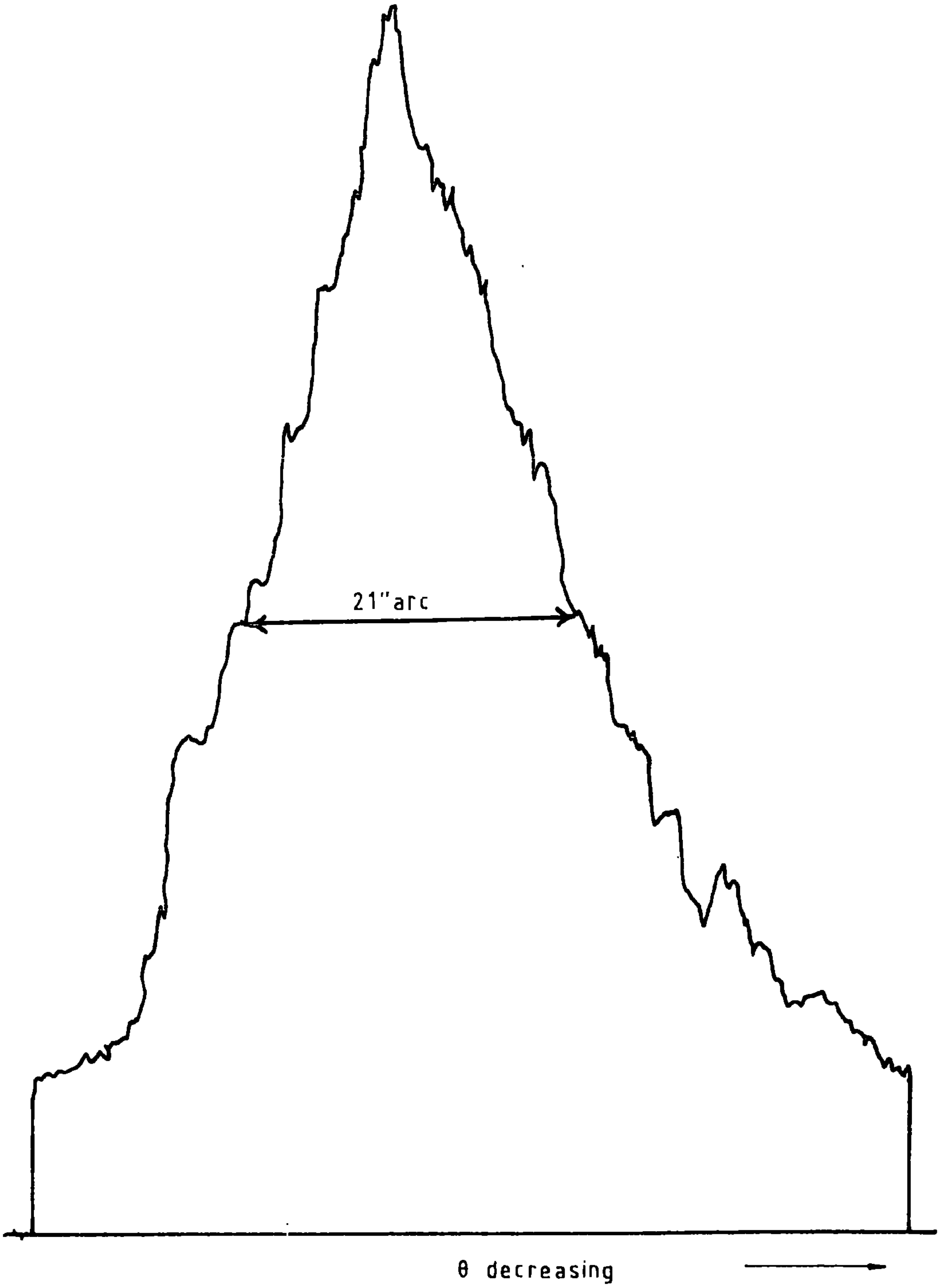

Fig.8.3(c) Film reflection rocking curve used to obtain the result of figure 8.9(i)&(l). Measurement scale different from (a) and (b).

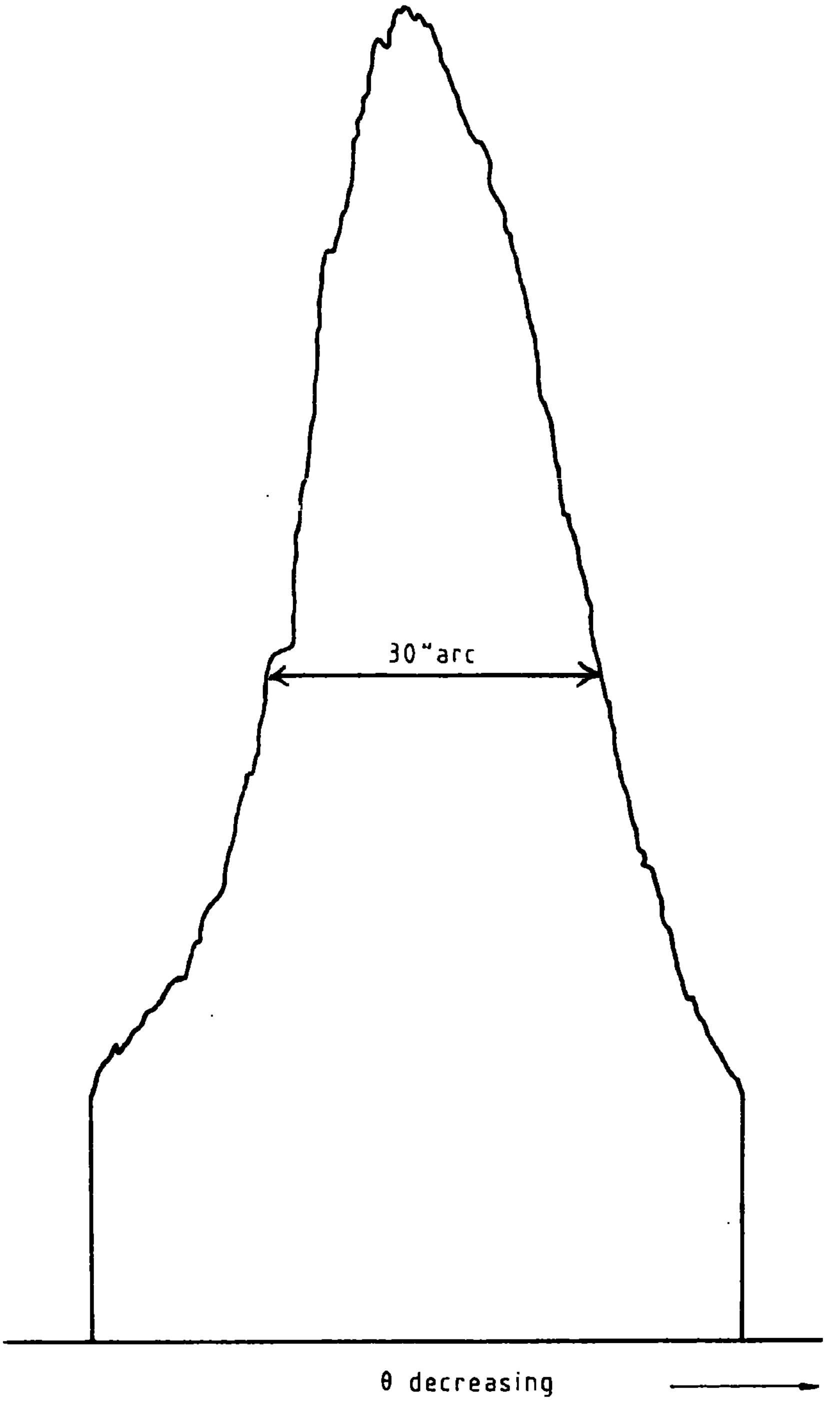

Fig.8.3(d) Film reflection rocking curve used to obtain the result of figure 8.9 (m)&(n).

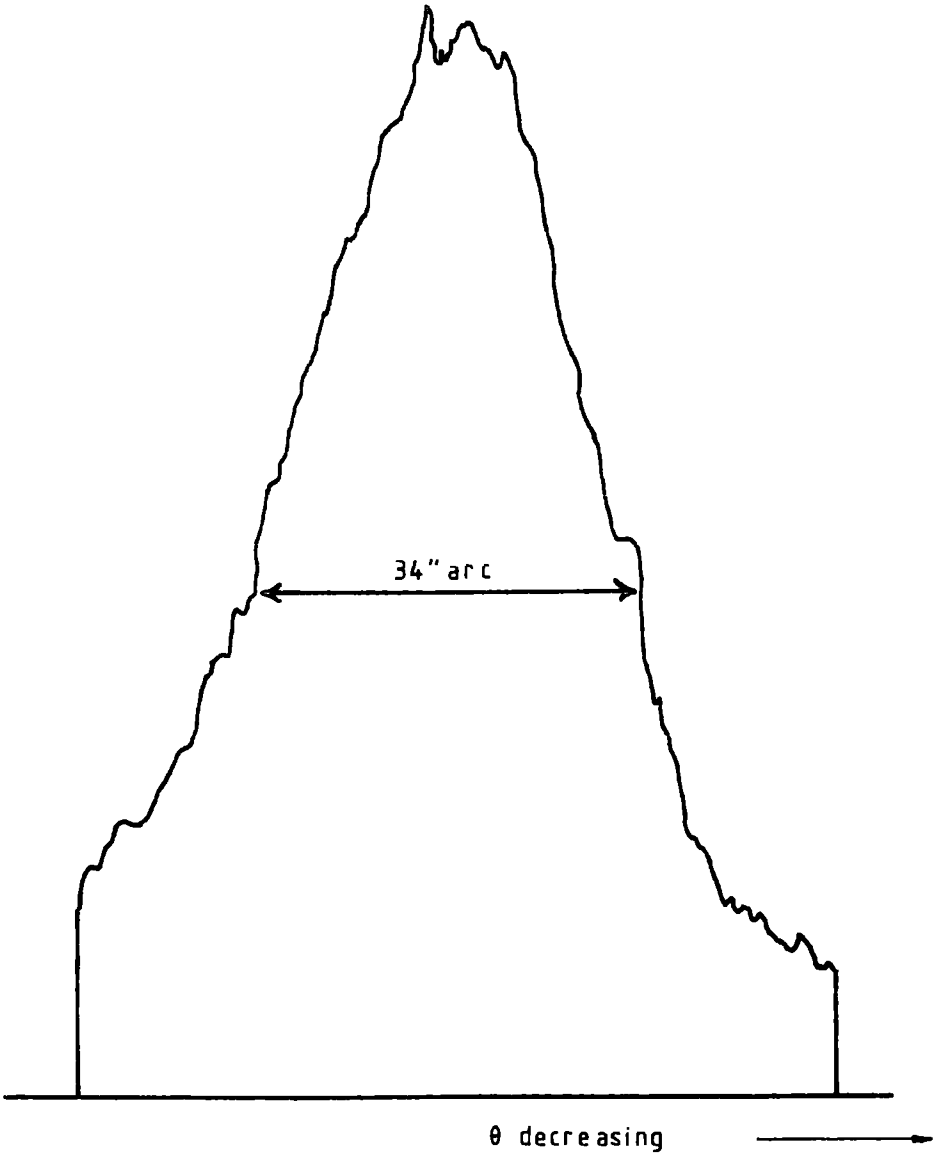

curves, especially of the film reflections, became progressively larger. This was thought to be due to handling of the crystals, and to the effects of the glue used. Final film second reflection widths were typically 30 seconds of arc. Some of the rocking curves observed are shown in Figure 8.3.

8.5 Goniometer arrangement

A considerable time was spent in trial and error before a suitable goniometer arrangement was devised for the specimen crystal. A review of the various arrangements which were tried will be given here. They are shown diagramatically in Figure 8.4.

It has been pointed out in section 8.2 that the samples were circular platelets. It is obvious that the sample could not be mounted on the goniometer with wax, as it would then have moved when magnetic fields of several thousand oesteds were applied. Initially, one side of the platelet was attached to a three circle goniometer by some araldite glue, which was allowed to set in its own time. The arrangement is shown in Figure 8.4(a). The diffractometer was aligned, and the rocking curve from the substrate reflection was observed. It was noted that the rocking curve was about 30 seconds of arc, and could not be decreased when the tilt was altered. Since the beam was incident at position A in the diagram (8.4(a)), it was concluded that the glue was causing the crystal to strain. The diffractometer was re-aligned so that the beam diffracted from the first crystal was incident at position B on the second crystal. A narrower rocking curve of width 15 seconds of arc was obtained. However, when a magnetic field of 2k Oe was applied to the specimen, it was noted that the rocking curve shifted quite considerably. The substrate rocking curve was not expected to shift at all when the magnetic field was applied. It was concluded that as the crystal was fairly large, and was only anchored at one point, some twisting of the sample was taking place as the magnetic field was applied.

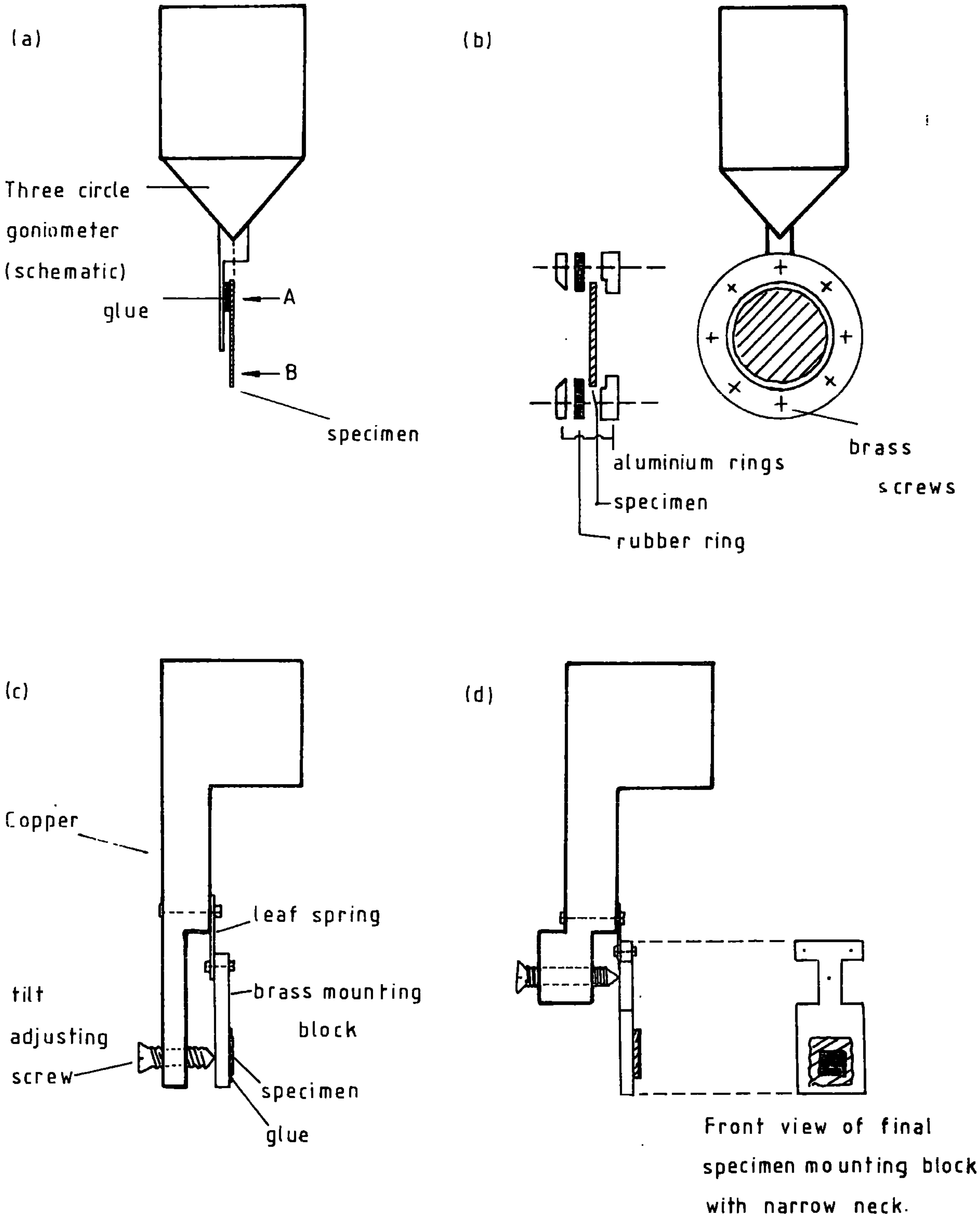

Fig. 8.4 Various goniometer arrangements tried for mounting specimen crystal.

In order to try and solve the dilemma of preventing the crystal from moving in the field whilst not introducing any extra strain in the crystal, the holder shown in Figure 8.4(b) was constructed. The crystal was positioned at the inner rim of an aluminium ring (A), and clasped around its perimeter by the rubber ring (B). A third ring (C) of aluminium held B against A with the help of some small brass screws. The result obtained was encouraging. The film reflection rocking curve was observed to shift in the expected direction when the magnetic field was applied. The maximum field obtainable with the laboratory electromagnet however was only 2.5k Oe, and magneto-optical measurements described in section 8.3 showed that this field was not of sufficient magnitude to cause the magnetization in the film to rotate from the uniaxial easy directions into the film plane.

At this stage, use was made of the specially constructed electromagnet described in Chapter 5. The fields taken from this went initially up to 9k Oe. It was immediately observed that the rocking curve of the substrate reflection shifted a good deal more than was expected when a magnetic field of about 9k Oe was applied. The angular position of the magnet was varied over a range of three degrees, and it was observed that the shift changed from positive at one end of the range to negative at the other. The maximum rocking curve shift recorded over this range of magnet positions was 10 seconds of arc. The shifts observed are shown in Figure 8.5. It is to be noted that the stray field of the magnet covers a considerably larger volume at a greater field strength than the stray field of the original standard laboratory electromagnet. Although the three circle goniometer chosen was of aluminium construction, it was subsequently discovered that the small locking screws were of steel, and these screws were responsible for the large shift observed.

As none of the commercial goniometers available was completely non-magnetic, it was decided that a special goniometer be built. The one shown

Fig.8.5 "Movement" from 0 position on rocking curve as a function of applied field for small variations in angular position about a "zero" setting. The movement is clearly due to some twisting effect.

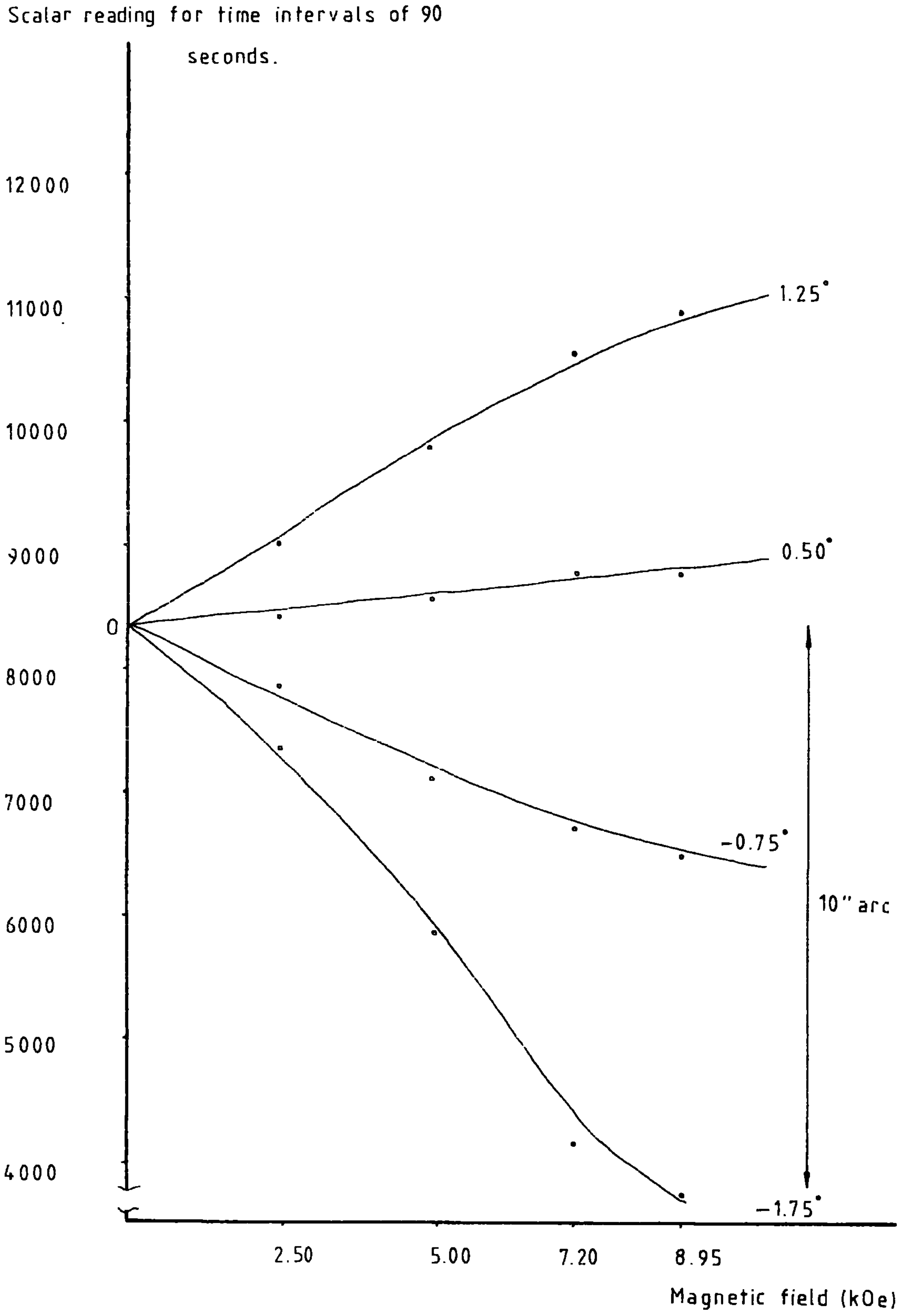

in Figure 8.4(c) was constructed from brass and copper. It consisted essentially of a small brass block against which the sample was mounted, and whose tilt could be adjusted. The tilt adjustment was provided by the leaf spring and screw mechanism shown in the diagram. The non-magnetic base, needed to attach the goniometer to the rotation axis of the diffractometer, was taken from a standard goniometer.

As the crystal was so large, it was never certain that any twisting effects in the magnetic field were being completely eliminated. It was decided then that a small segment of the sample be used. Some araldite glue was evenly smeared very lightly over an area of the brass mounting block (A) of the goniometer, the sample segment was gently laid flat on the layer of araldite, and the glue was allowed to dry slowly in its own time. Again the substrate reflection rocking curve was very wide. It was thought, however, that the effect of adjusting the tilt of the crystal was to induce some strain in the crystal directly behind the crystal, since the tilt adjusting screw was located against the brass mounting block. A similar goniometer shown in Figure 8.4(d) was constructed. However, in this arrangement the tilt adjusting screw was located near the top of the brass crystal-mounting-block. The latter also was modified in the latest construction so that it had a narrow neck in which a small hole was drilled. The point of the tilt adjusting screw located in this. The neck served to prevent as much as possible any strain that might have been induced by the leaf spring and adjusting screw from being transferred into the rest of the brass mounting block and the crystal.

When the crystal which had been mounted on the goniometer shown in Figure 8.4(c) was remounted on the latest goniometer, the rocking curve of the substrate second reflection was found to be 17 seconds of arc in width. With the previous goniometer on which the crystal had strained, widths of between 40 and 50 seconds of arc had been obtained.

The magnet was positioned so that the magnetic field was aligned parallel to the plane of the sample. Therefore when the field was increased, the magnetization in the film would be rotated from the uniaxial easy directions into the plane of the film. The crystal was adjusted so that it was positioned on the flank of the substrate reflection rocking curve. The beam diffracted from the second crystal was detected by the gas proportional tube and the pulses from this were counted by the scalar. The magnet's angular position was altered over a range of five settings, each pair separated by one degree. At each setting the scalar was set to count for two minutes, once with zero applied field and once with an applied field of 8.95k Oe. The scalar readings for each of the two minute intervals are shown in Table 8.4. It can be seen from the number of counts for each interval has a counting error, taken as the square root of the number, of slightly more than 1%.

Table 8.4

Effect of magnetic field on substrate second reflection

Relative angular setting of magnet *	Magnetic field (k Oe)	Counting time (seconds)	Counts
0	0	120	7581
	8.95	120	7834
↷ 1	0	120	7987
	8.95	120	7699
↷ 2	0	120	7606
	8.95	120	7909
↶ 1	0	120	7320
	8.95	120	7506
↶ 2	0	120	7787
	8.95	120	7737

* The relative angular setting is shown in degrees. 0 is taken to mean that the field is parallel to the sample. Then 1 and 2 are the number of degrees the magnet is moved from the 0 setting, clockwise and anticlockwise as indicated.

The actual position of the crystal was changed along the rocking curve by approximately three seconds of arc, and the number of counts then observed for a two minute interval changed by about 40%. From these observations, it was therefore concluded that the crystal itself was not changing its position in the applied field. Similar observations were made at four subsequent stages, on various pieces of the sample, throughout the period that the experimental work was carried out. The apparatus was then ready for magnetostriction measurements to be carried out on the film. These measurements are described in section 8.8. However, in the following two sections, the effects of temperature and measurements with Copper $K\alpha_1$ radiation will be described first of all.

8.6 Effect of temperature change on the rocking curve position

The measurements made on the samples were carried out at room temperature. An investigation was carried out in order to determine the effects of any net temperature changes which might occur during the course of the experiments. The "warm" junction of a thermocouple thermometer was attached to the goniometer close to where the crystal was mounted, so that the temperature recorded by the thermometer was very nearly equal to the temperature of the crystal. A film reflection rocking curve was plotted out on the X. Y recorder at a crystal temperature of, for example, 16^{o}C. Warm air was then passed around the goniometer, and a steady temperature of, for example, 28^{o}C was reached. A further rocking curve was recorded at this elevated temperature. The observed shift of the rocking curve was determined by the difference in the position of the centroids of the two rocking curves recorded. A typical result is shown in Figure 8.6. It can be seen that the difference in centroid positions is approximately 17.5 seconds of arc. If it is assumed that the temperature change is linear over the range being considered, it can be seen that there is a shift in the rocking curve of close to 1.5

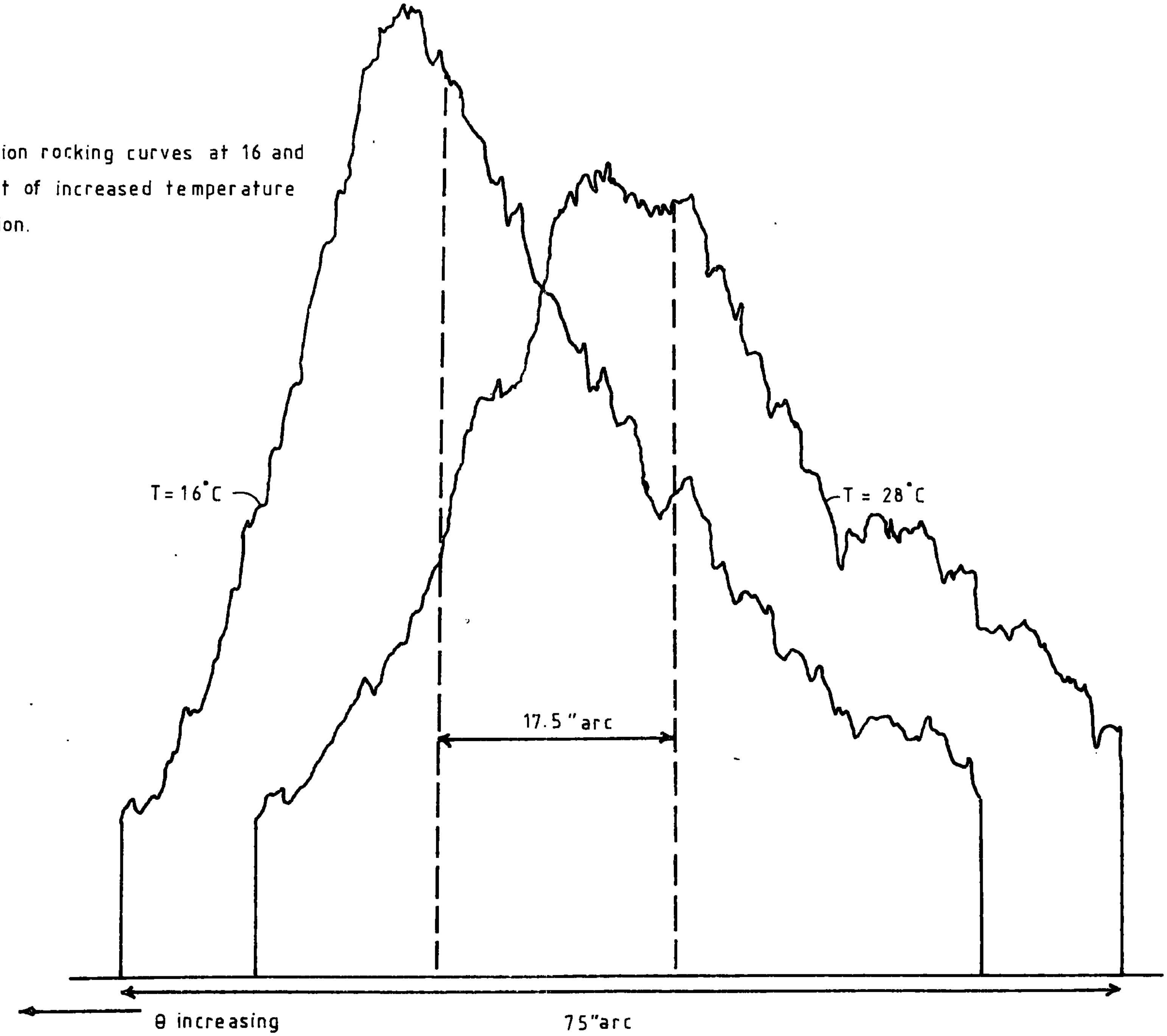

Fig. 8.6 Film reflection rocking curves at 16 and 28°C, showing effect of increased temperature on the curve position.

seconds of arc per degree centigrade net change in temperature. It will be seen that the change in rocking curve position magnetostrictive strain is about twice this, and therefore temperature effects may be a serious source of error. The temperature changes were reduced by adequate ventilation of the laboratory so that heat from electrical apparatus did not build up. The diffractometer was water cooled, and this also helped to stabilize the temperature of the specimen. A check of the temperature with the thermometer throughout an experimental run showed that it did not vary by more than $\pm {}^1/4^\circ$. Another method of checking that the temperature remained constant was to monitor the reflected intensity for a given interval of time without the applied field before and after monitoring the reflected intensity with the applied field, and to note that both recorded intensities were the same. This particular method was more often adopted, and will be described further in section 8.8.

8.7 Measurements with Copper Kα_1 radiation

A comparison of Bragg angles and orders of reflection for CuKα_1 and MoKα_1 characteristic radiation is given in Table 8.5. The values are given for the lattice planes of the garnet $Tb_2LuFe_5O_{12}$. It can be seen that for comparable Bragg angles, the order of reflection of CuKα_1 radiation

Table 8.5

Comparison of Bragg angles and orders of reflection for CuKα_1 and MoKα_1 radiation

	CuKα_1	MoKα_1
Wavelength	1.540Å	0.709Å
Reflecting planes	(8,8,8)	(16,16,16)
Bragg angles	59.5°	52.5°

is considerably lower than of MoKα_1 radiation. It has been pointed out in Chapter 7 that the absorption of MoKα_1 radiation over the X ray beam path length is considerably less than of CuKα_1 radiation. This fact is more than balanced by the lower order of reflection of CuKα_1 radiation for similar Bragg angles, and it has been observed that for similar operating conditions of the diffractometer and X ray generator, the recorded reflected X ray intensity of CuKα_1 wavelength was considerably greater than that of MoKα_1 wavelength. Further it has been noted that the peak intensity of the reflection from the film $Tb_2LuFe_5O_{12}$ was greater than that of the reflection from the substrate, in agreement with similar observations of Hart and Lloyd (1974). In the present case, it was noted that the intensity ratio was approximately 2:1. These facts certainly would have made the use of CuKα_1 radiation more attractive.

The energy of a photon of CuKα_1 radiation is lower than that of a photon of MoKα_1 radiation. Thus the threshold level setting of the proportional detector counting system needed to be set fairly low in this case so that a reasonable counting rate could be obtained. An unfortunate subsequent observation was that the magnetic field from the electromagnet had a detrimental effect on the ratemeter reading. The latter decreased almost to zero when the magnetic field was increased to about 10k Oe. No such effect was observed when MoKα_1 radiation was employed, and a much higher threshold level could be used.

Some attempts were made to shield the detection apparatus from the magnetic field; these involved enveloping the various parts of the equipment with some high permeability iron metal foil. However, the ratemeter reading still decreased by just as much when the magnetic field was switched on. No magnetostriction measurements therefore were made when CuKα_1 characteristic radiation was being employed.

8.8 Magnetostriction measurements

8.8.1 Measurement from rocking curve flank

It can be seen in Figure 8.3 that the flanks of the rocking curves are linear over a considerable part. Use of this fact was made in order that the magnetostriction measurements could be made. The flank of a given rocking curve was plotted in the following way. The crystal was set to reflect, for example, at the point "A" on the rocking curve of Figure 8.3(a), and the reflected intensity was monitored by the detector/scalar for a set time. The crystal was rotated by 30 steps of the stepper motor to position "B", the reflected intensity similarly monitored, and then again at position "C". The interval separating each pair of points A,B and B,C can be seen to be equal to 3.09 seconds of arc from a consideration of the calibration of the diffractometer rotation axes, given in Chapter 6. The crystal was set at a position on the straight line flank passing through the points A,B,C. For given values of the applied magnetic field, from zero upwards, the Bragg reflected intensity from the specimen crystal was monitored. In this way the "movement" along the flank was measured for each value of applied field was measured, and from this, the value of the magnetostrictive strain was deduced from the differential form of Bragg's equation.

8.8.2 Value of magnetostrictive strain

From Table 8.1 it can be seen that the expected sign of λ_{111} for the sample is positive. This means that in its normal uniaxial state, the film is strained by the effect of magnetostriction and the strain is such that there is an expansion along the [111] direction. From equation 1.10, it can be seen that when the magnetization is in the [111] direction, along with the measuring direction, the value of the magnetostrictive strain, relative to the demagnetized state, is equal to λ_{111}. If then the magnetization is rotated to a direction perpendicular to [111], for example [1$\bar{1}$0] or [$\bar{2}$11], the magnetostrictive deformation relative to the demagnetized state then becomes $-\frac{1}{2}\lambda_{111}$. Thus the change in magnetorestrictive deformation as the magnetization is rotated from the [111] direction into the plane of the sample is such as to give a compression along [111], and the magnitude is

$$\Delta\ \frac{d\ell}{\ell} = \frac{3}{2}\ \lambda_{111} \qquad (8.1)$$

This can also be seen from equation 1.11 for a uniaxial crystal. The value of ψ is put equal to 90° and λ here is then λ_{111}.

8.8.3 Samples and operating conditions

Five pieces of the original circular platelet were studied, and the magnetostriction measurements were taken from four of these. The sizes and shapes are shown in Figure 8.7. Four of the pieces were from the outer regions of the platelet, and one, the largest, was taken from the middle.

The size of the X ray collimator slit, shown in Figure 7.1(b), was 5mm in height by 1.5mm in width. It was found that if these dimensions were decreased by very much, then the reflected intensity (from the second crystal) became impractically low. With the smaller samples, the peak intensity of the rocking curve was typically 30 counts per second. With the largest sample, the peak counting rate was typically 90 counts per second. This indicates that there was some vertical divergence of the beam incident on the second crystal, that is, the beam height was greater than the height of the smaller crystal segments.

When the measurements were being made, the X ray generator was operating at a maximum of 50kV and 24mA. MoKα_1 radiation was used. The reflecting planes were (16,16,16).

Fig.8.7 Sizes and shapes of samples of $Tb_2Lu_1Fe_5O_{12}$ film on G.G.G. substrate.

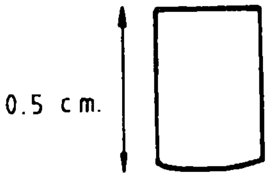

Sample 1

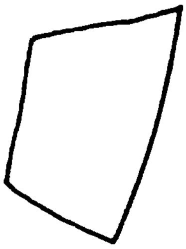

Sample 2

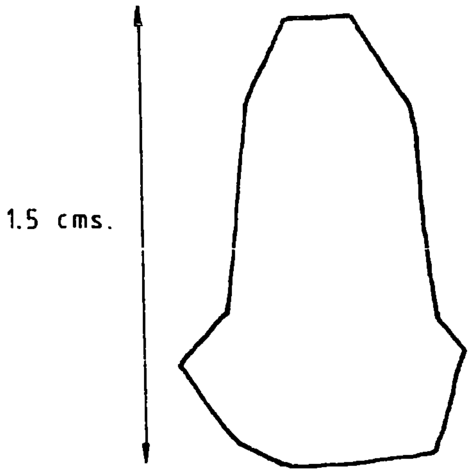

Sample 3

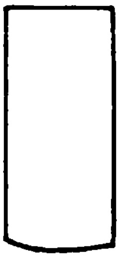

Sample 4

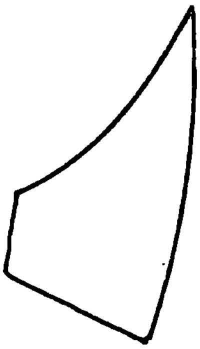

Sample 5

8.8.4 Measurements

The measurements were made as described in section 8.8.1. If, for example, the crystal was positioned on the high angle side of the rocking curve, it can be seen that the reflected intensity was expected to increase when the magnetic field was applied. In such a case then, the measurements in the applied field were made at position B in Figure 8.3 before the reflected intensity was monitored at C. In this way, no reversal of the stepper motor drive system had to occur, and therefore no backlash effect was introduced during the measurement. A schematic representation of a typical set of results, shown as a "movement" along the flank of the rocking curve for given values of applied field, is given in Figure 8.8.

In all, fifteen sets of measurements were made from the four pieces of sample. The displacements along the flank of the rocking curve were converted to the corresponding values of ΔΘ. Figure 8.9 shows plots of ΔΘ versus applied magnetic field made for each experimental run. With each plot, the following information is given: rocking curve width, rocking curve peak intensity, average "square root" error on the scalar readings, counting time and sample number (as given in Figure 8.7).

It has been seen in section 8.6 that a check needed to be kept on the effect of temperature on the position of the rocking curve. In some of the measurements, the crystal was positioned, for example, at the point B on the rocking curve as mentioned above. This peak has been called the "zero field" or "base" point. It was monitored for the given interval before and after all the measurements with the applied field had been made. Any difference then in the "base" point was considered to be due to the effects of a net temperature change during the course of the experimental run. An even closer check was to monitor the "base" point before and after each individual application of the magnetic field. This was done for the remainder of the measurements not checked by the first method. These methods are called

Fig.8.8 Movement along flank of rocking curve owing to magnetostriction, as measured for result 8.9(d).

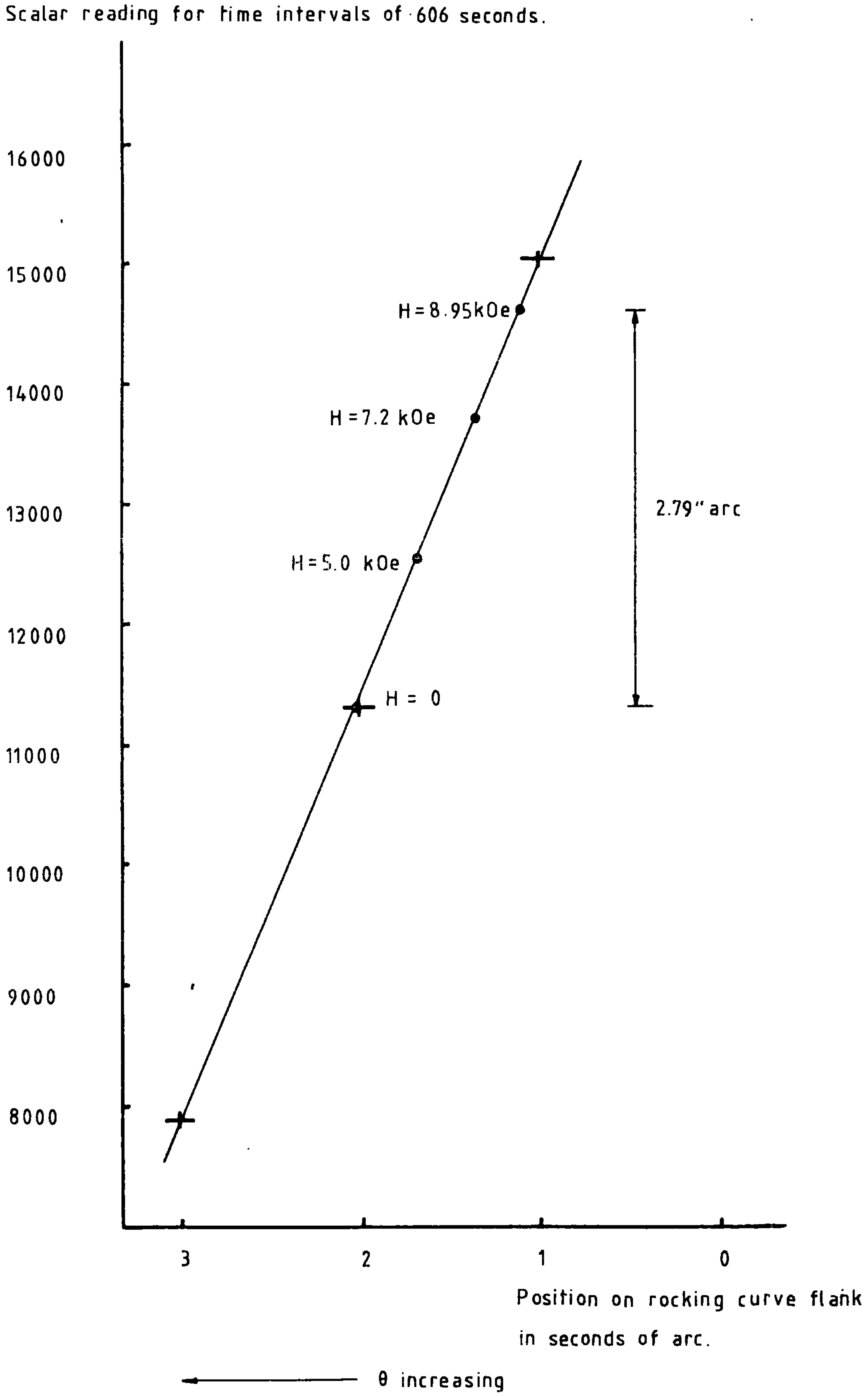

Fig. 8.9 Plots of measured values of movement, $\Delta\theta$, along rocking curve flank versus magnetic field strength, and one upon field strength.

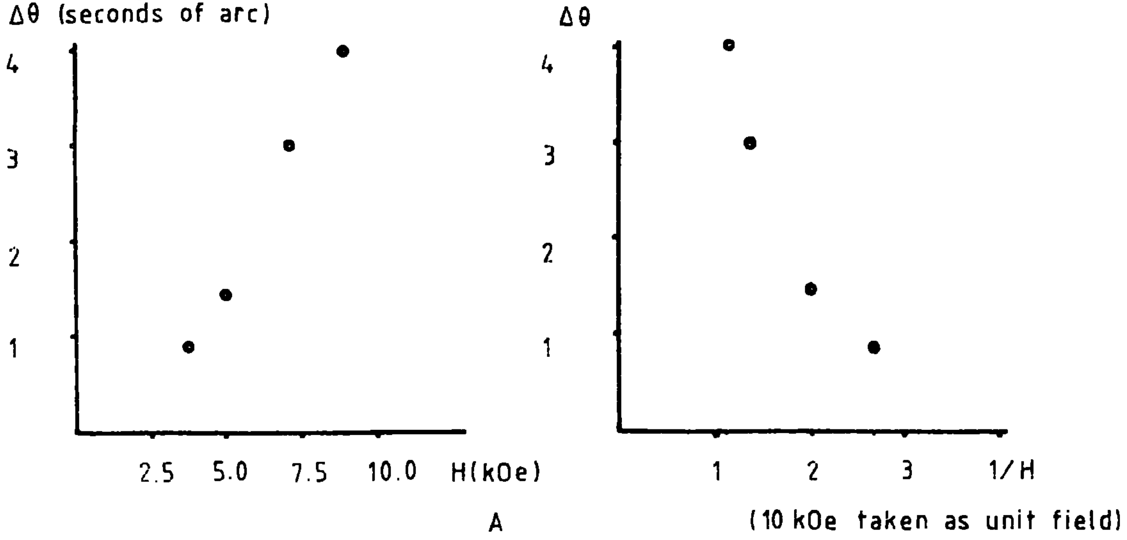

Fig. 8.9(a)

1	30" arc
2	27 c.p.s.
3	1.5 %
4	300 seconds
5	1

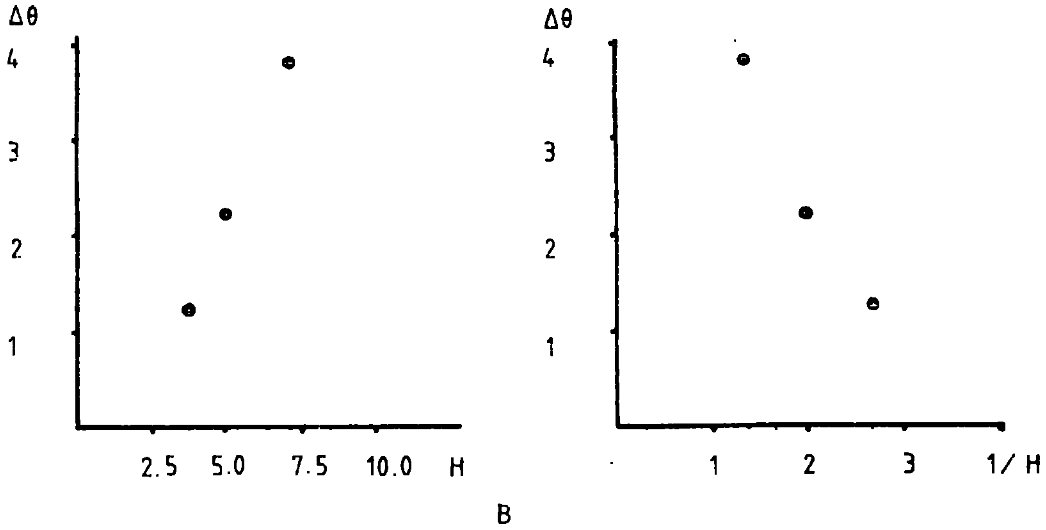

Fig. 8.9 (b)

1	30" arc
2	27 c.p.s.
3	1.5 %
4	300 seconds
5	1

Key to graph captions.

1 Rocking curve width at half height.
2 Peak count rate for rocking curve.
3 Percentage square root counting error.
4 Monitoring time.
5 Sample number.

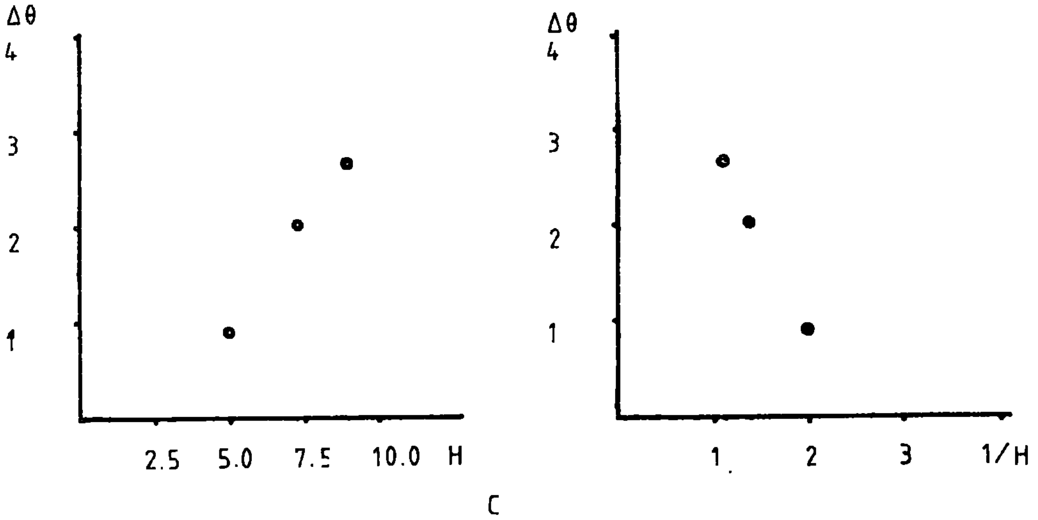

Fig.8·9(c)

1	28"arc
2	28 c.p.s.
3	0.5%
4	1060 seconds
5	1

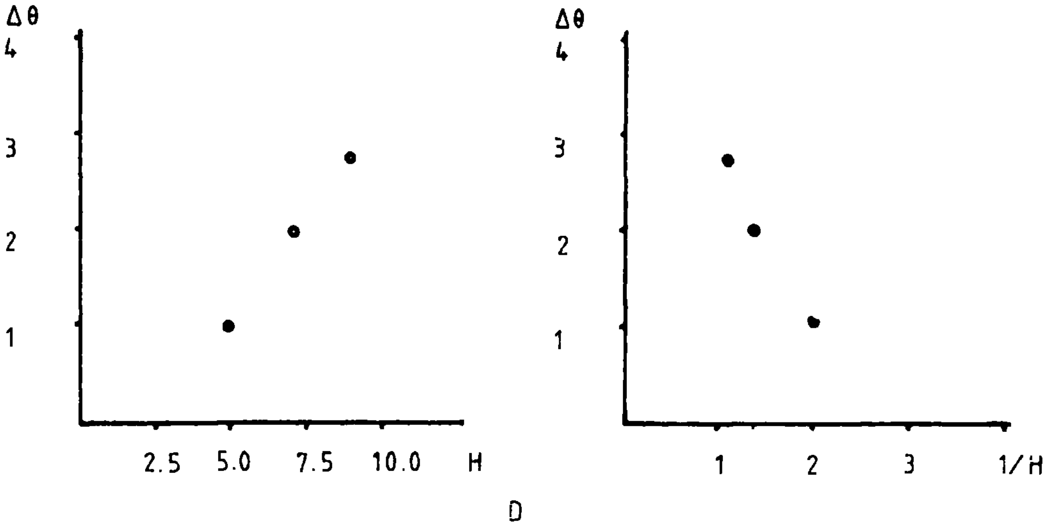

Fig.8·9(d)

1	21"arc
2	29 c.p.s.
3	0.9%
4	606 seconds
5	2

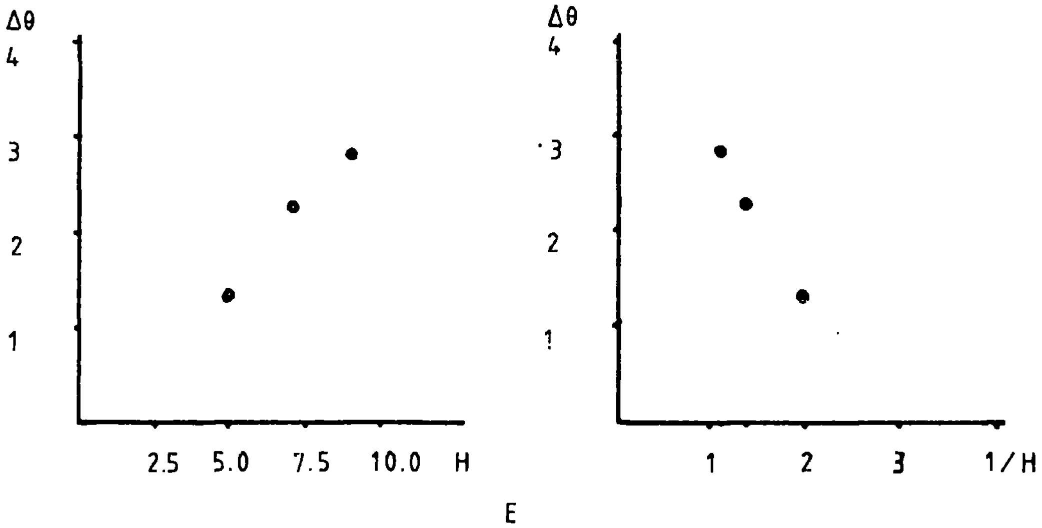

Fig.8·9(e)

1	21"arc
2	29 c.p.s.
3	0.9%
4	587 seconds
5	2

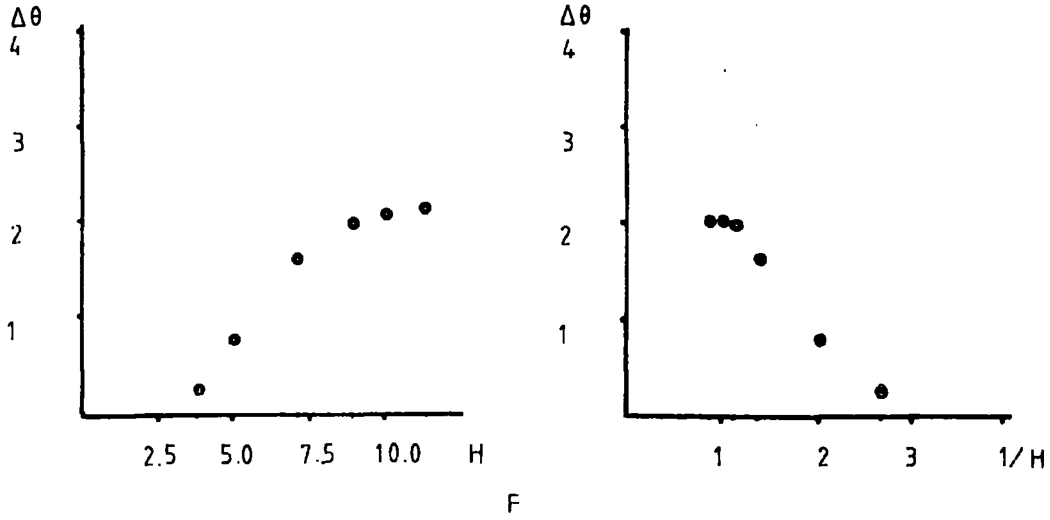

Fig.8·9(f)
1 24"arc
2 26 c.p.s.
3 1.4%
4 300 seconds
5 2

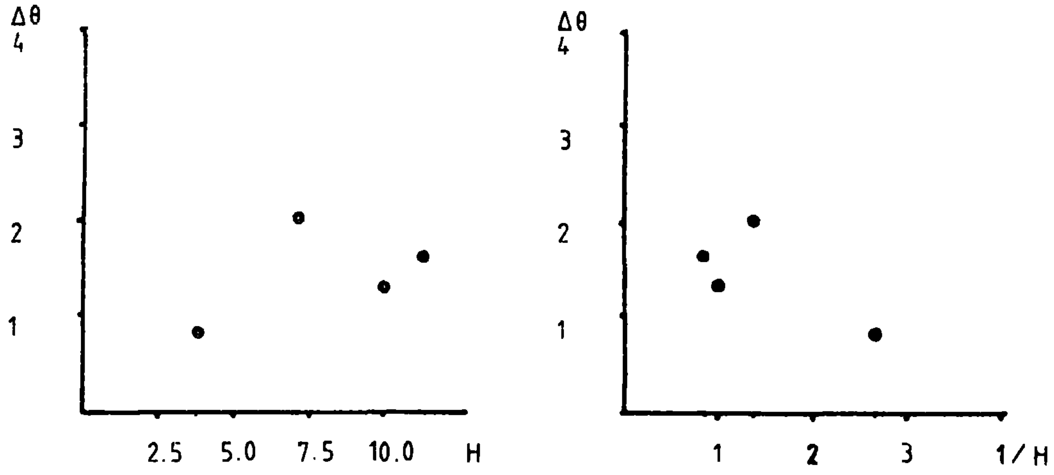

Fig.8·9(g)
1 31"arc
2 90 c.p.s.
3 0.9%
4 180 seconds
5 3

G

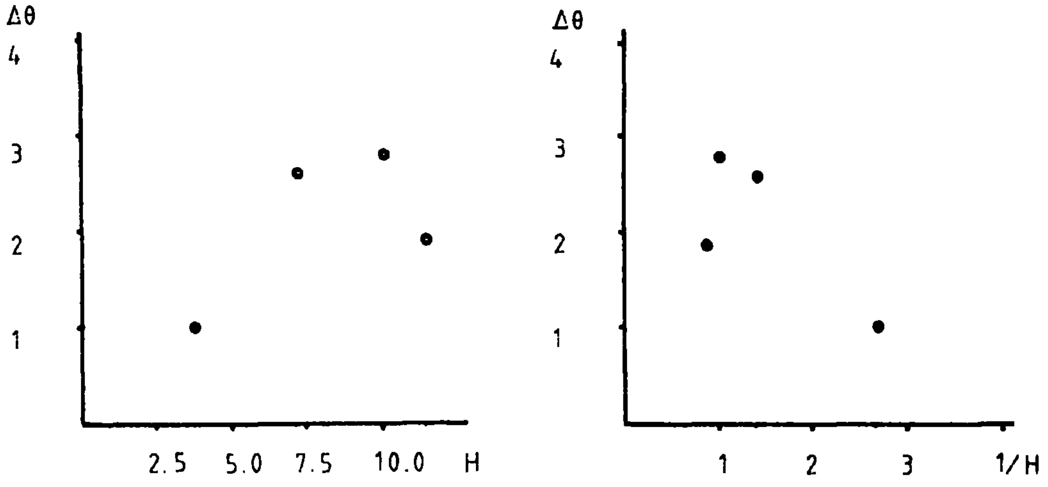

H

Fig.8·9(h)
1 31"arc
2 90 c.p.s.
3 0.9 %
4 180 seconds
5 3

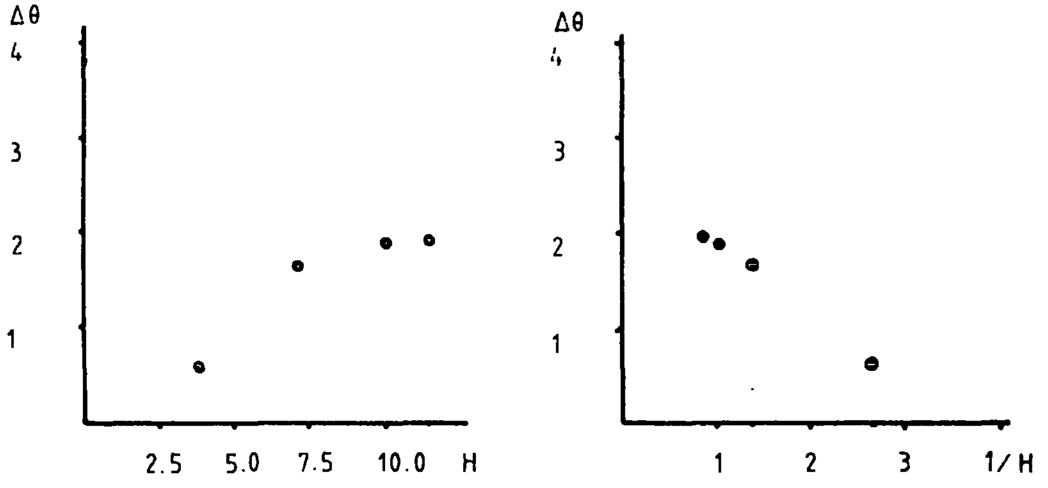

I

Fig.8·9(i)
1 30"arc
2 90 c.p.s.
3 1.0%
4 180 seconds
5 3

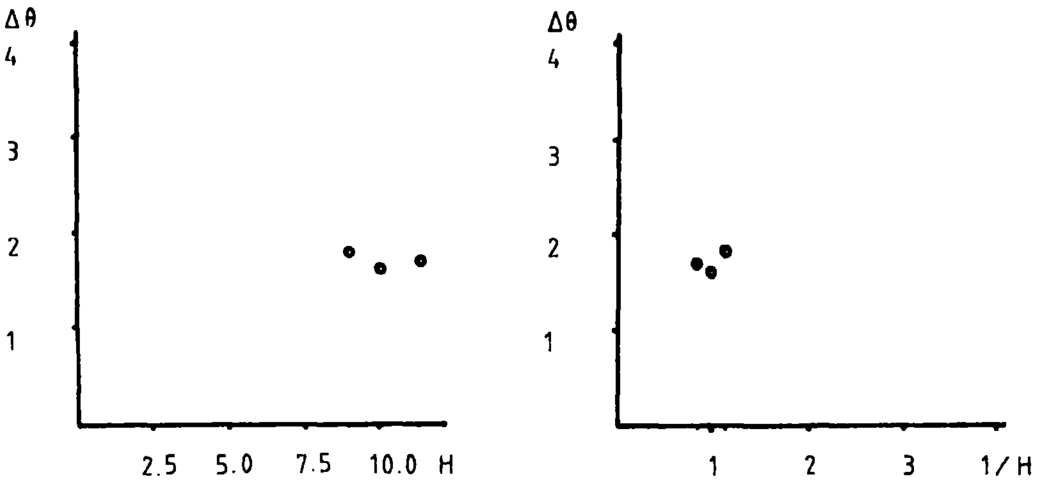

J

Fig.8.9(j)

1	22"arc
2	29 c.p.s.
3	1.5%
4	320 seconds
5	2

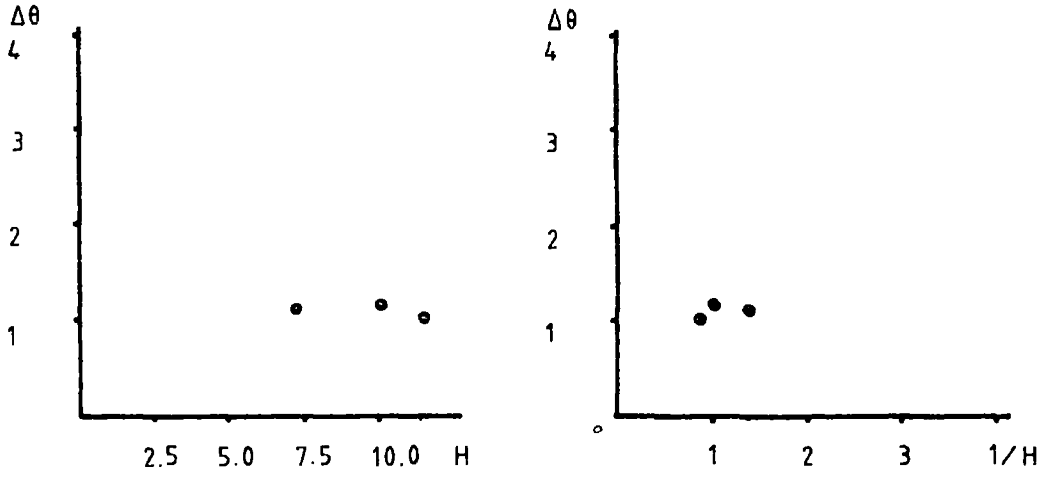

K

Fig.8.9(k)

1	36"arc
2	22 c.p.s.
3	1.4%
4	568 seconds
5	4

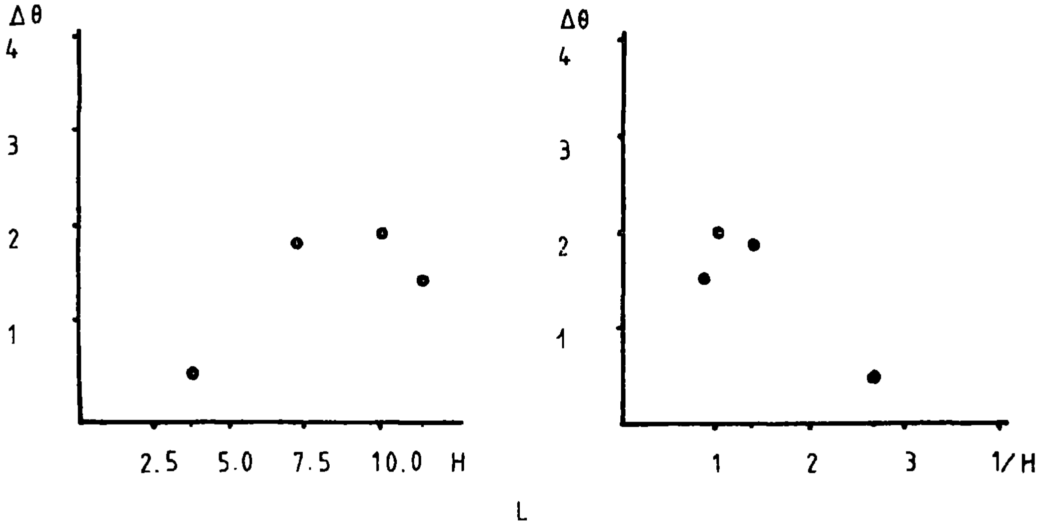

Fig.8.9(l)

1 30"arc
2 90 c.p.s.
3 1.0%
4 180 seconds
5 3

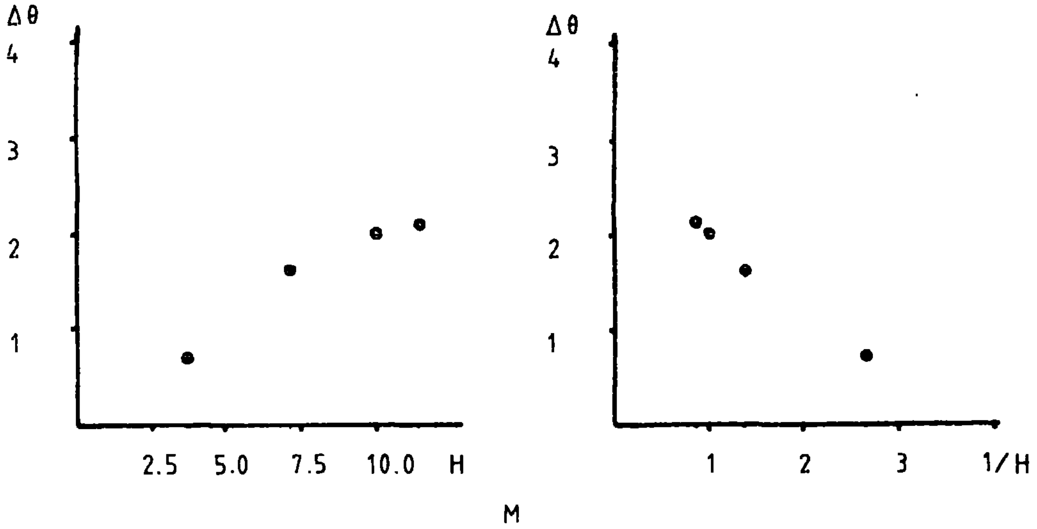

Fig.8.9(m)

1 35"arc
2 70 c.p.s.
3 0.9%
4 300 seconds
5 3

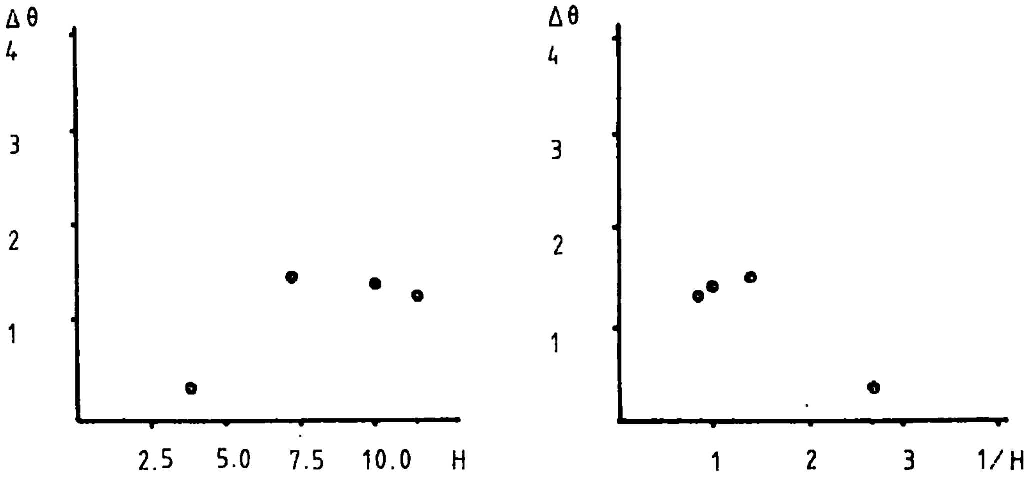

N

Fig.8·9(n)

1	35"arc
2	70 c.p.s.
3	0.9%
4	300 seconds
5	3

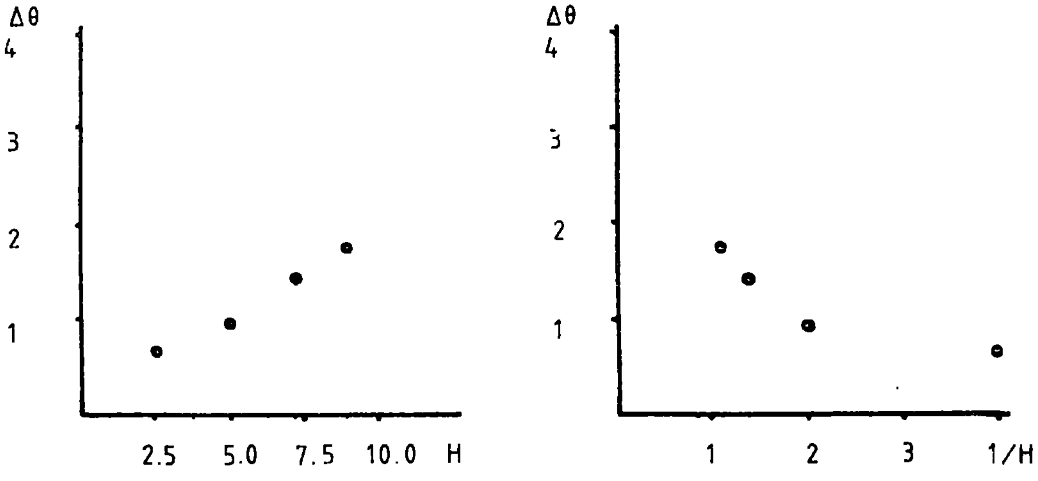

O

Fig.8·9(o)

1	28"arc
2	28 c.p.s.
3	0.5%
4	1060 seconds
5	1

"method 1" and "method 2" respectively. The maximum movement of the "base" point during the course of each run is shown in Table 8.6; this is given as the percentage change in the scalar reading for a given interval of time, and thus represents the maximum error in the magnetostrictive strain measurements, which is due to the effects of temperature instability.

Table 8.6

Percentage error in strain measurement owing to movement in "base" point

Experimental run	Method of "base" point checking	Maximum change in measured intensity at "base"
A	method 1	0.7%
B	method 1	0.7%
C	--	-
D	method 1	0.2%
E	method 1	2.0%
F	method 1	10.9%
G	method 2	7.0%
H	method 2	2.3%
I	method 2	1.0%
J	method 1	1.7%
K	method 2	2.0%
L	method 2	4.5%
M	method 2	1.6%
N	method 2	1.6%
O	method 1	2.0%

Often in the experimental runs which were checked by method 2, the percentage changes of base point were considerably less than the maximum values shown in Table 8.6. Comparison of the percentage changes in "base" point with the square root counting errors given in Figure 8.9 shows that most of the former "temperature" errors are quite small.

A puzzling observation was the decreasing change in reflected intensity at high field values, especially in the results, G, I, and L. It was thought that perhaps some slight movement of the crystal was occurring at these high values of the field, although with the goniometer arrangement, and crystal mounting technique being used, this was unexpected. However, the sample used in these particular measurements is the largest of the four.

8.8.5 Treatment of measurements

It can be seen that a considerable number of the magnetostrictive strains measured show no tendency to saturate. This observation was made when the first sets of measurements were being carried out. Here, only field values of up to 8.95k Oe were used, since the magnet cooling circuit was not complete. When the cooling system was ready, just high field measurements were made under the assumption that these would correlate with the previous lower field measurements. This explains the absence of low field measurements in some experimental runs and of high field points in others. Since most of the results showed no tendency to saturate, it was difficult to extrapolate the results to infinite field and thus to obtain a value of the λ_{111} magnetostriction constant, as indicated schematically in Figure 8.10.

In order to obtain a value of λ_{111}, the results are extrapolated to infinite magnetic field. The usual procedure adopted in magnetostriction measurements is to plot $\Delta\ell/\ell$ versus ΔH. Here $\Delta\Theta$ is plotted against $^1/H$. The unit value of magnetic field was taken as 10k Oe. The plots are shown for each experimental run in Figure 8.9 alongside the corresponding plots of $\Delta\Theta$ versus H. A straight line was fitted to each plot by the method of least squares. The value of the intercept of the straight line on the ordinate obtained for each was taken to be the value of $\Delta\Theta$ at infinite magnetic field. The series of values of $\Delta\Theta$ intercepts obtained is shown in Table 8.7.

Table 8.7

Value of ordinate intercept in least squares fit of $\Delta\Theta$ versus $^1/H$

Experimental run	Intercept ($\Delta\Theta$, seconds of arc)
A	5.99
B	6.53
C	4.98
D	4.86
E	4.63
F	3.26
G	2.10
H	3.22
I	2.67
J	1.17
K	0.98
L	2.53
M	2.78
N	2.04
O	1.82

An average of these was found. With a value of Θ_B equal to 52.5°, the relation

$$\frac{d\ell}{\ell} = -\frac{\Delta\Theta}{\tan\Theta_B} \qquad (8.2)$$

together with relation (8.1) is used to obtain an average value of λ_{111}

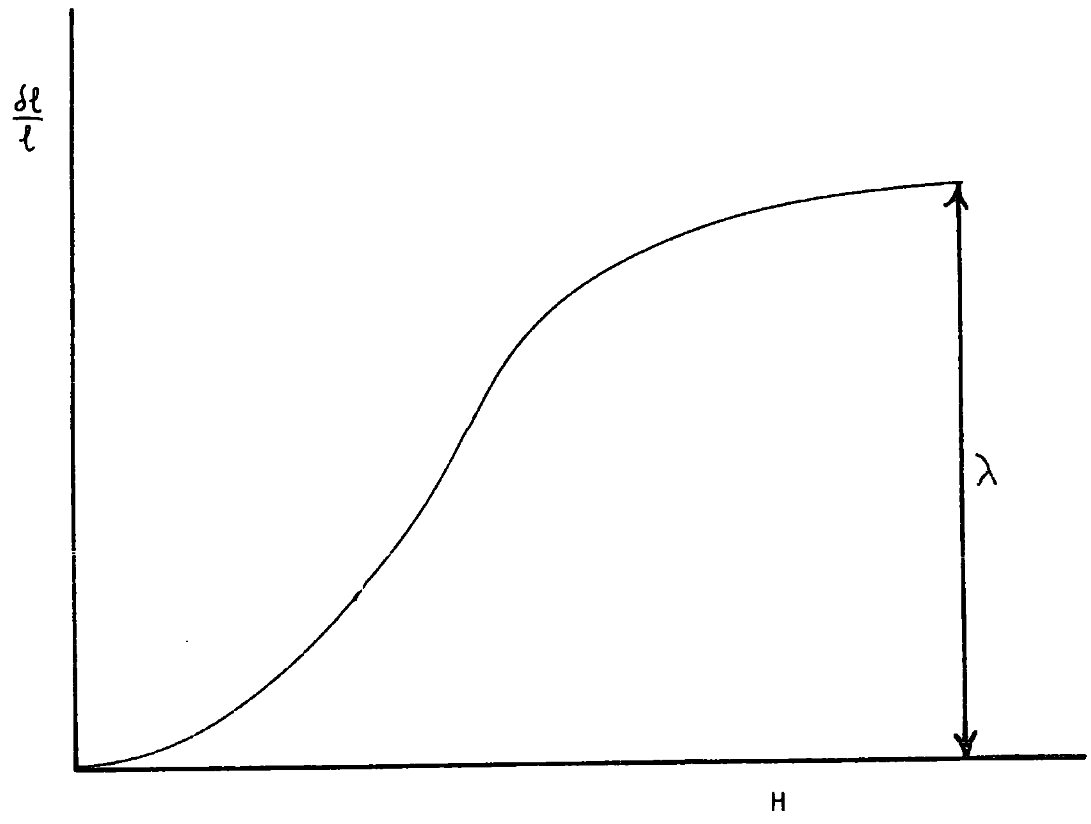

Fig.8.10 Magnetostriction as a function of the field intensity. Chikazumi (1964).

$$\lambda_{111} = (8.12 \pm 1.00) \times 10^{-6}$$

where the standard error has been quoted. This method of obtaining the value of λ_{111} oversimplifies the behaviour of $\Delta\Theta$ with $1/H$. From a consideration of Figure 8.10 it would be expected that the value of $\Delta\Theta$ would level off at low values of $1/H$ and thus the value of λ_{111} obtained from the least squares fit is an overestimate of the actual value by about 10%.

8.9 Double crystal topographs

Double crystal topographs were taken of the substrate sample 2 and of the substrate of a fifth piece of the original platelet, which was of similar dimensions to those of sample 2. The experimental arrangement for taking double crystal topographs has been described in Chapter 4. The detection plate was placed as close to the specimen as possible. For the topographs described here, symmetric reflections in the (+,−) parallel positions were used. The procedure used for processing the nuclear emulsion plates is essentially that described by Tanner (1976). All the details of the two topographs are given in Table 8.8. The reference crystal was the same as that used in the magnetostriction measurements. Topographs 1 and 2 are shown in Figures 8.11 and 8.12 respectively.

The featuresof the topographs include bright and dark curved bands, which are growth striations. Such features in G.G.G. grown by the Czochralski technique have also been revealed by Stacy (1974b) who also used the method of double crystal topography. From the black and white contrast of the bands, an estimate may be made of the variation in lattice parameter in the substrate owing to the compositional variation arising during the growth process. From the rocking curve width used in topograph 1, a value of $\Delta\Theta$ may be taken to be 9 seconds of arc. Similarly from the rocking curve width used in topograph 2, $\Delta\Theta$ may be taken to be 13.5 seconds of arc. From the relation $\frac{\Delta \ell}{\ell} = \frac{-\Delta\Theta}{\tan\Theta}$, which omits the lattice rotation term of equation 4.25, values

Table 8.8

Details of topographs 1& 2

	Topograph 1	T	Topograph 2
Reflection	(16,16,16)		(8,8,8)
Radiation	Mo K_{α_1}		Cu K_{α_1}
Exposure	36 hrs.		20 hrs.
X-ray generator setting	50 kV. 24 mA.		50 kV. 24 mA.
Plate type	Ilford L4, 50μ		Ilford L4, 50μ
Rocking curve width.	18" arc.		27" arc.

Fig.8·11 Double crystal topograph of substrate of sample 2 using Mo K_{α_1} radiation. The presence of growth striations is clear from the black and white contrast bands. The presence of a facet region may be inferred from the region A.

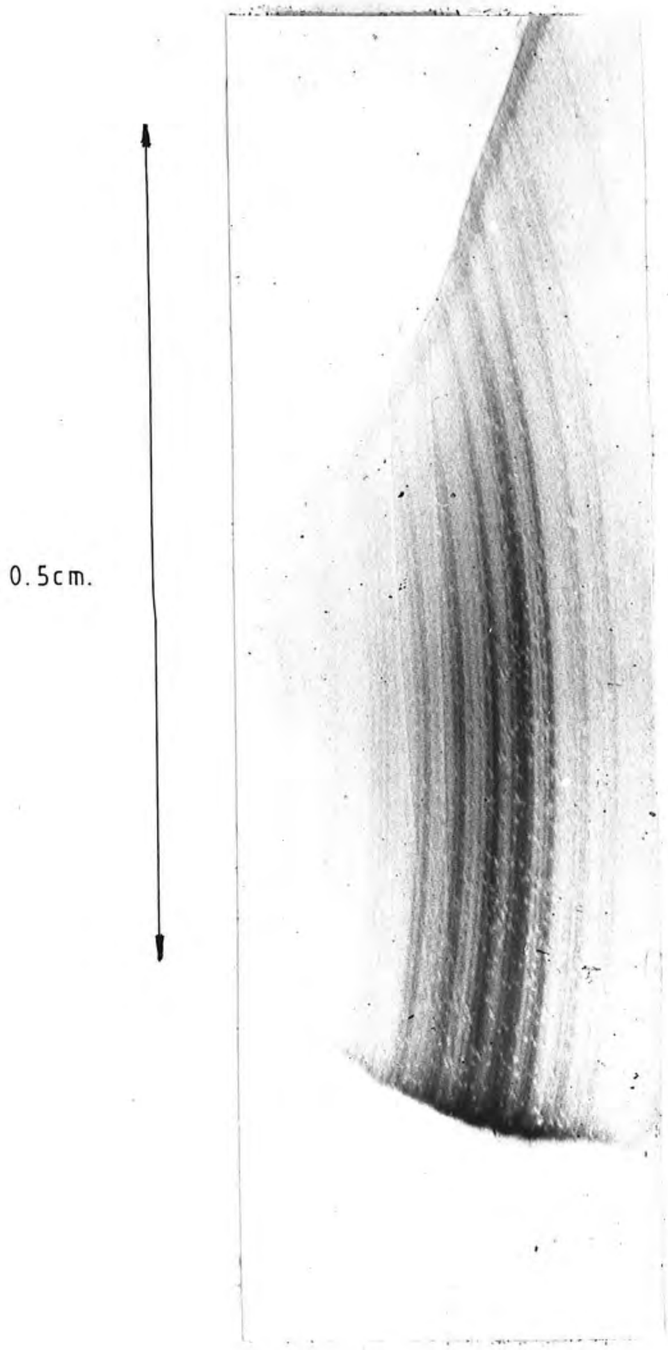

Fig.8·12 Double crystal topograph of substrate of sample 5 using Cu K_{α_1} radiation. Again growth striations are evident.

of the strain $\frac{\Delta\ell}{\ell}$ are found to be 3.3 x 10^{-5} and 3.8 x 10^{-5}, that is, the strain owing to growth striations may have an average value of 3.5 x 10^{-5}. Components of this strain may be transferred into the magnetic film, as has been pointed out in Chapter 1.

A further feature present in topograph 1 is a bright oval region, labelled A. This has the appearance of a facet region, the strain of which is transferred into the film. It has been seen that the anisotropy of the crystal may vary when such strains are present in the film. The facet observed is very similar in appearance to those made visible by Stacy (1974b). The crystal used for topograph 1 was one of those used for the magnetostriction measurements. It was taken from the outer region of the crystal platelet, as were sample 1 and sample 4. It has been concluded that these features of the crystals have been a contributory factor to the variation of the results obtained. Each experimental run of the pairs of results (G,H), (L,I) and (M,N) was made on the opposite side of the respective rocking curve to the other run. It can be seen that there is considerable difference in measurements made even on different parts of the same rocking curve.

8.10 Conclusions

Several conclusions have been drawn from the measurements which have been carried out in the work of this thesis. They may be summarised as follows.

1. The double crystal diffractometer which has been built has a sensitivity such that strains of the order of 10^{-5} - 10^{-6} may be measured. Such measurements of course require crystals of good lattice perfection.
2. Provided that the position of the samples may be kept sufficiently stable in the applied magnetic field, "small" values ($\lambda < 10^{-5}$) of magnetostriction may be measured.

3. The magnetostriction measurements are not reproducible for different parts of the sample, or even for different parts of the rocking curve. The measurements depend on the state of local strain, and an "overall" or "average" value is taken from the series of measurements obtained.
4. The value of λ_{111} which has been obtained agrees, within the experimental error, to the expected value obtained by linear weightings. The method of measurement analysis is, however, expected to lead to an over-estimate of the actual value.

8.11 Suggestions for further work

Now that the double crystal diffractometer and magnet are in full operation, magnetostriction measurements may be extended to a whole series of materials. The requirements of these materials are that they be of good lattice perfection and that their magnetization may be saturated by the magnetic field available.

Work on magnetostriction measurements by the strain gauge technique is currently in progress in the Durham group also. An interesting investigation would be to compare magnetostriction measurements made with the double crystal diffractometer and then with strain gauges.

Magnetic domains have been observed in Ni by Chikaura and Nagakaura (1975) with X ray topography, and more recently by Kuriyama et.al. (1976), who used transmission topography on Czochralski grown single crystals. An interesting extension of Bradler and Polcarova's (1972) work on Fe:Si could perhaps cover the case of Ni, in which domain walls are of the 71° and 109° type. The spontaneous magnetostriction constant determined in this case would be λ_{111}, since the easy directions are <111>.

Bibliography

(1842) Joule J.P., Sturgeon's Annals of Electricity 8 219

(1893) Lochner S.J., Phil. Mag. 36 498

(1913) de Broglie M., Le Radium 10 186

(1915) Compton A.H., Trousdale E.A. Phys. Rev. 5 315

(1917) Compton A.H., Phys. Rev. 10 95

(1920) Compton A.H., Rognley O., Phys. Rev. 16 464

(1921) Bragg L., et. al., Phil. Mag. 41 309

(1921) Davis B., Stempel W.M., Phys. Rev. 17 608-623

(1922) Becker J.A., Phys. Rev. 20 134

(1925) Webster W.L., Proc. Roy. Soc. 107 496

(1928) Yensen T.D., Phys. Rev. 31 714

(1929) Lloyd H., J. Sci. Instr. 6 81

(1930) Stearns J.C., Phys. Rev. 35 1

(1931) Akulov N.S., Z. Phys. 69 78

(1932) Allison S.K., Phys. Rev. 41 1

(1932) Parratt L. G., Phys. Rev. 41 561

(1933) Richtmyer F.K. et. al., Phys. Rev. 44 311

(1935) Compton A.H., Allison S.K., X Rays in Theory and Experiment" 709-730

(1936) Kaya S., Takaki H., Anniversary volume (Sendai) 314

(1939) Bitter F. Rev. Sci. Instr. 10 373-381

(1945) Wooster N., Wooster W.A., Nature 155 786

(1947) Goldman J.E., Phys. Rev. 72 529

(1948) Street R., Proc. Phys. Soc. (London) 60 236

(1949) Kittel C., Rev. Mod. Phys. 21 541

(1949) Williams H.J., Shockley W., Bozorth R.M., Phys. Rev. 75 155

(1951) Carr W.J., Smoluchowski R. Phys. Rev. 83 1236

(1951) Yoder H., Keith M.L., American Mineralogist 36 519-533

(1952) Bond W.L., Andrus J., American Mineralogist 37 622-632

(1953) Bozorth R.M., Hamming R.W. Phys. Rev. 89 865-869

(1955) Corner W.D., Hunt G.H. Proc. Phys. Soc. 68A 133

(1955) Lee E.W. Rep't Prog. Phys. 18 184-229

(1956) Akulov N.S. Sov. Phys. Doklady 1 1-4

(1956) Cullity B.D. "Element of X ray Diffraction" (AdisonlWesley)

(1956) Kaye G.W.C., Laby T.H. "Table of Physical and Chemical Constants" (Longman, Green and Co.)

(1958) Bonse U., Kappler E., Z. Naturforschung 13a 348-349

(1958) Dash W.C., J. App. Phys. 29 736-737

(1958) Tsuya N., J. App. Phys. 29 449

(1958) Tweet A.G. J. App. Phys. 29 1520-21

(1959) Lang A.R. Acta Cryst. 12 249

(1960) Birss R.R., Lee E.W.

(1960) Bond W.L. Acta Cryst. 13 814-818

(1960) Merz K. J. App. Phys. 31 147-154

(1960) Roth W.L. J. App. Phys. 31 2000

(1960) Slack G.A. J. App. Phys. 31 1571

(1961) Bitter F., Rev. Sci. Instr. 33 342-349

(1961) Gersdorf R. Thesis Univ. Amsterdam

(1961) "Handbook of Chemistry and Physics" (Chem. Rubber Pub. Co.)

(1961) Montgomery B., National Magnet Laboratory M.I.T.)

(1961) Slonczewski J.C. J. App. Phys. 32 2535

(1962) Bonse U. "Direct Observations of Imperfections in Crystals" (Wiley, N.Y.) 431

(1962) Lang A.R., Polcarova M. App. Phys. Letts. 1 13-15

(1963) Alberto L., Alberto A.L. Phil. Mag. 8 2101

(1963) Callen E.R., Callen H.B. Phys. Rev. 129 578-593

(1963) Callen E.R. et. al. Phys. Rev. 130 1735-40

(1963) Darnell F.J. Phys. Rev. 132 128-133

(1963) Iida S. Phys. Letts. 6 165-167

(1963) Legvold S. et. al. Phys. Rev. Letts 10 509

(1964) Birss R.R. "Symmetry and Magnetism" (North Holland) P. 182 et. seq.

(1964) Chikazumi S. "Physics and Magnetism" (John Wiley and Sons)

(1964) Clark A.E. et. al. J. App. Phys. 35 1028-29

(1964) John K., Iida S. J. Phys. Soc. Jap. 19 344-350

(1964) Radeloff C. Z. Angew Phys. 17 247

(1965) Callen E.R., Callen H.B. Phys. Rev. 139 A455-471

(1965) Rhyne J.J., Legvold S. Phys. Rev. 140 A2143

(1965) Tatsumoto E., Okamoto T. J. Phys. Soc. Jap. 20 1534

(1966) Belov K.P. et. al. J.E.T.P. Letts. 4 127

(1966) Clark A.E. et. al. J. App. Phys. 37 1324-26

(1966) Lourens J.F., Viljoen P.E. Physica 32 1177

(1966) Yamada T. et. al. J. Phys. Soc. Jap. 21 664-671

(1966) Yamada T. et. al. J. Phys. Soc. Jap. 21 672-680

(1967) Benninger G.N., Pavlovic A.S. J. App. Phys. 38 1325-26

(1967) Comstock R.L., Raymond J.J. J. App. Phys. 3737-39

(1967) Iida S. J. Phys. Soc. Jap. 22 1201-09

(1967) Polcarova M., Kaczer J. Phys. Stat. Sol. 21 635-642

(1967) Smith A.B., Jones R.V. J. App. Phys. 38 2700-01

(1967) Zijlstra H. "Experimental Methods in Magnetism" (North Holland)

(1968) Basterfield J. et. al. J. Mat. Sci. 3 33-40

(1968) Callen E.R. J. App. Phys. 39 519-527

(1968) Clark A.E. et. al. J. App. Phys. 39 573-575

(1968a) Hart M. Proc. Phys. Soc. A309 281-296

(1968b) Hart M. Sci. Prog. Oxf. 56 429-447

(1968) Kohra K., Takano Y. Jap. J. App. Phys. 7 982-988

(1968) Kroon D. "Laboratory Magnets" (Philips Technical Library)

(1968) Williams G.M., Pavlovic A.S. J. App. Phys. 39 571

(1969) Polcarova M., Gemperlova J. Phys. Stat. Sol. 32 769-778

(1970) Bobeck A.H. et. al. App. Phys. Letts. 17 131

(1970) Bottom V.E., Carvalho R.A. Rev. Sci. Instr. 42 196

(1970) Sykora B., Peisl H. Z. Angew. Physik. 30 320

(1971) Bower D.I. Proc. Roy. Soc. (London) A326 87-96

(1971) Callen H.H. App. Phys. Letts. 18 311-313

(1971) Heinz D.M. et. al. J. App. Phys. 42 1243

(1971) Ishikawa Y., Syono Y. J. Phys. Soc. Jap. 31 461

(1971) Kurtzig A.J., Hagedorn F.B. I.E.E.E. (Mag.) 7 473-476

(1971) Lee E.W., Asgar M.A. Proc. Roy. Soc. (London) A326 73-85

(1971) Polcarova M., Lang A.R. Phys. Stat. Sol. 4 491-499

(1971) Robinson M. et. al. I.E.E.E. (Mag.) 7 464-466

(1971) Rosenwaig A., Tabor W.J. J. App. Phys. 42 1643-44

(1971) Schick L.K. J. App. Phys. 42 1554

(1971) Schick L.K. et. al. App. Phys. Letts. 18 89-91

(1972) Bradler J., Polcarova M. Phys. Stat. Sol. (a) 9 179-186

(1972) Glass H.L. Mat. Res. Bull. 7 1087-92

(1972) Krumme J.P. et. al. Phys. Stat. Sol. (a) 12 483-490

(1972) Matthews J.W. et. al. Mat. Res. Bull. 7 213-222

(1973) Cockayne B. et. al. J. Mat. Sci. 8 382-384

(1973) Cockayne B., Roslington J.M. J. Mat. Sci. 8 601-605

(1973) Hansen P., Krumme J.P. J. App. Phys. 44 2847-52

(1973) Mathiot A. et. al. Phys. Stat. Sol. (a) 20 K1-K4

(1973) Miller D.C. J. Electrochem. Soc. 120 678-685

(1973) O'Kane D.F. J. Electrochem. Soc. 120 1272

(1973) Okazaki A., Kawaminami M. Jap. J. App. Phys. 12 783-789

(1973) Patel J., Mathiot A. J. App. Phys. 44 3763

(1974) Hart M., Lloyd K.H. J. App. Cryst. 8 42-44

(1974) Isherwood B.J., Wallace C.A. Physics in Technology 5 244-258

(1974) Petroff J.F., Mathiot A. Mat. Res. Bull. (U.S.A.) 9 319

(1974a) Stacy W. et. al. J. Cryst. Growth 22 37-43

(1974b) Stacy W. J. Cryst. Growth 24/25 137-143

(1975) Birss R.R., Isaac E.D. "Magnetic Oxides" Part 1 298-348 (Ed. Craik)

(1975) Chikaura Y., Nagakura S. Acta Cryst. 31A S149

(1975) Craik D.J. "Magnetic Oxides" Ch. 9. (Wiley and Sons)

(1975) Makram H., Vichr M. "Magnetic Oxides" 97-140

(1975) Nakahigashi K. et. al. J. Phys. Soc. Jap. 38 1634

(1975) Petroff J.F., Mathiot A. Acta Cryst. 31A S3 149

(1975) Petroff J.F., Mathiot A. A.I.P. Conf. Proc. (U.S.A.) 28 757-758

(1976) Clark A.E. et. al. A.I.P. Conf. Proc. (U.S.A.) 29 192-195

(1976) Estop E. et. al. Acta Cryst. A32 627-630

(1976) Greenough R.D., Underhill C. Physica 81B 24-34

(1976) Hart M., Baker J.F.C. et. al. Sol. State Electronics 19 331-334

(1976) Kuriyama M. et. al. J. App. Phys. 47 5064

(1976) Tanner B.K. "X Ray Diffraction Topography" (Pergamon)

(1977) Sery R.S. et. al. To be submitted to Conference on Magnetism and Magnetic Materials, Minneapolis, November.

Appendix 1

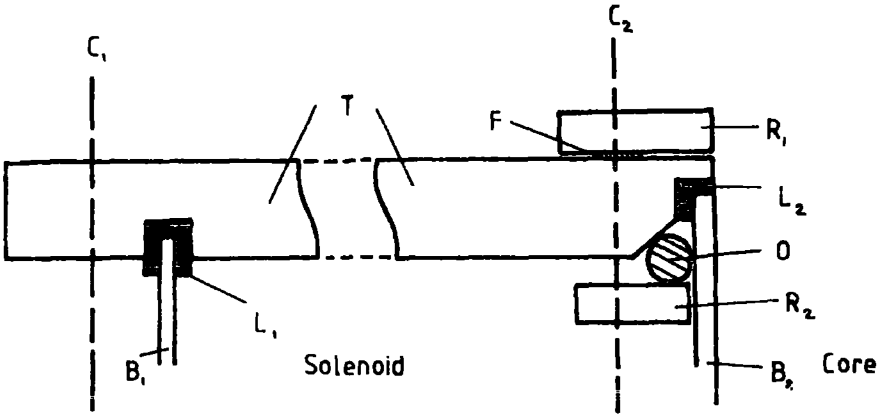

Schematic diagram showing tufnol end plate arrangement, in cross section. Water sealing is provided by rubber rings L_1, L_2, O and fibre washer F, and is effected by the tightening of screws passing along C_2 through brass ring R_1, tufnol end plate T and brass ring R_2, and by means of threaded rods which pass along C_1 and which connect top and bottom end plates. B_1, B_2, outer and inner brass cylinders between which is solenoid.

Appendix 2

List of Suppliers for magnet parts:

Iron: Joplings Steel Foundry, Pallion, Sunderland

Extruded rubber channel: North East Rubber Company, North Shields

O rings (8¼ins diameter): James Walker, 20 Broad Chare, Newcastle

Tufnol sheet: Tuckers Ltd (Teesside), Murdock Road, Middlesbrough

Pole piece bolts: H Osborn Ltd. Tel. Newcastle 20311

Plastic tubing: Peter Plastics, Chain Bridge Road, Blaydon

Brass sheet: Righton National Metal Services, Newcastle

Copper: J Smith & Sons Ltd., 52 Third Avenue, Brierley Hill, Staffs.

Appendix 3

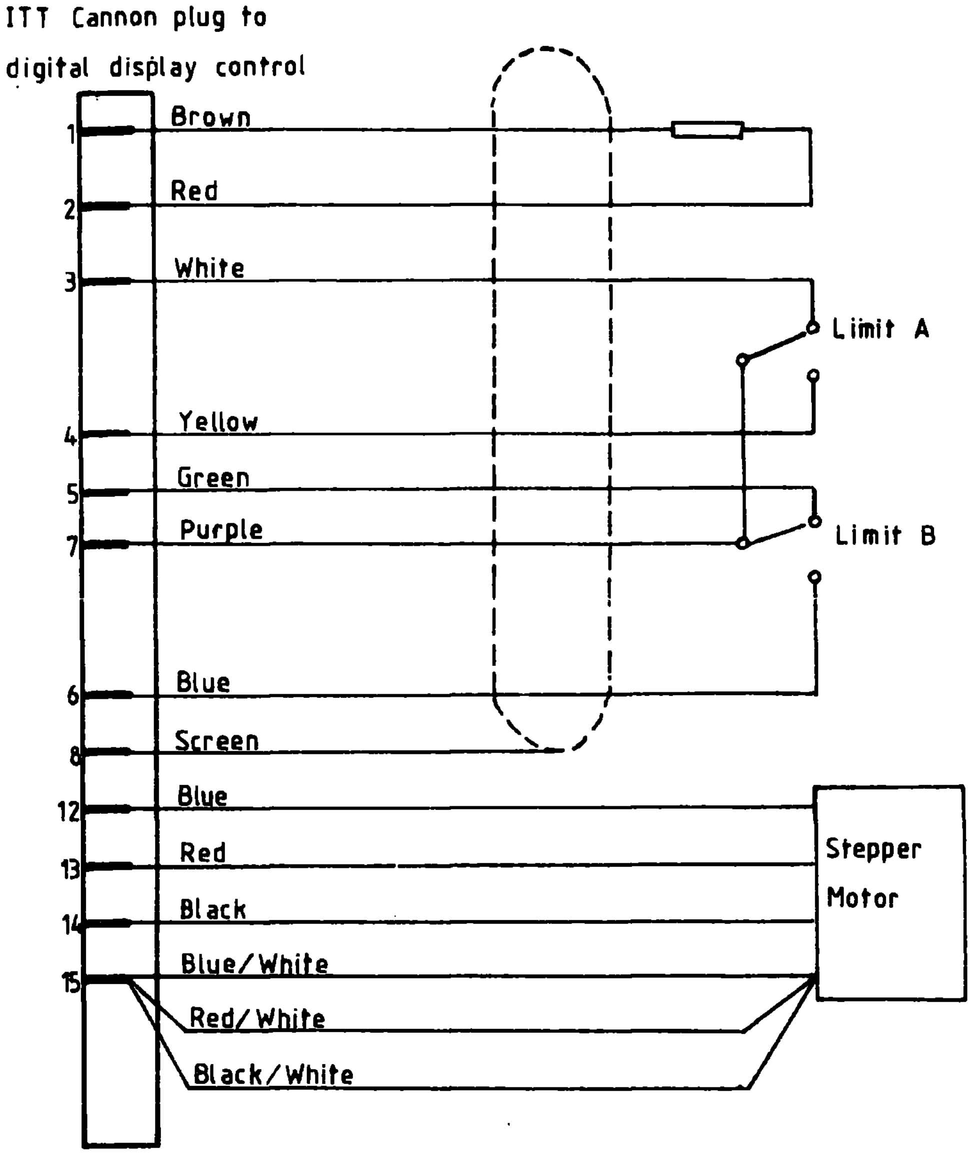

Colour code for stepper motor wiring connections.